W4 Revisited: A chimney candidate in the Milky Way Galaxy explored using radio continuum and polarization observations.

by

Jennifer Lorraine West

A Thesis
Submitted to the Faculty of Graduate Studies
In Partial Fulfillment of the Requirements for the Degree of

MASTER OF SCIENCE

Department of Physics and Astronomy
University of Manitoba
Winnipeg, Manitoba

© Jennifer Lorraine West, August 2003

THE UNIVERSITY OF MANITOBA

FACULTY OF GRADUATE STUDIES

*****

COPYRIGHT PERMISSION PAGE

W4 Revisited: A chimney candidate in the Milky Way Galaxy explored using radio continuum and polarization observations.

BY

Jennifer Lorraine West

A Thesis/Practicum submitted to the Faculty of Graduate Studies of The University of Manitoba in partial fulfillment of the requirements of the degree of

MASTER OF SCIENCE

Jennifer Lorraine West © 2003

Permission has been granted to the Library of The University of Manitoba to lend or sell copies of this thesis/practicum, to the National Library of Canada to microfilm this thesis and to lend or sell copies of the film, and to University Microfilm Inc. to publish an abstract of this thesis/practicum.

This reproduction or copy of this thesis has been made available by authority of the copyright owner solely for the purpose of private study and research, and may only be reproduced and copied as permitted by copyright laws or with express written authorization from the copyright owner.

Abstract

Compelling evidence for the existence of a fragmented superbubble above W4 that may be in the process of evolving into a chimney has been found. High latitude extension fields above the W3/W4/W5 star forming region have been processed at both 1420 and 408 MHz (21 and 74 cm) Stokes I total power as well as Stokes Q and U polarization. These observations reveal an egg-shaped structure with morphological correlations between our data and the Hα data of Dennison, Topasna & Simonetti (1997, ApJ 474 L31) as well as evidence of breaks in the continuous structure. Assuming an estimated distance of 2.3 kpc, the egg structure measures ~165 pc wide and extends ~240 pc above the mid-plane of the Galaxy. In addition the polarized intensity images show depolarization extending from W4 up the walls of the superbubble providing strong evidence that the observed continuum and Hα emissions are at the same distance as the W4 region.

A temperature spectral index map indicates that there are no high energy losses in the region via synchrotron emission. This implies that energetic cosmic rays retain sufficient energy to escape into the Galactic halo. In addition the rotation measure in the region has been calculated allowing an estimate of the line of sight magnetic field ($B_{//}$) in the region to be determined. We find $B_{//} = 9 \pm 8$ μG assuming a wall thickness of 20 pc or $B_{//} = 13 \pm 11$ μG assuming a wall thickness of 10 pc and directed *towards* the observer.

In addition, some interesting features appearing in the polarization and 408 MHz datasets are examined. These features are not likely related to the W4 superbubble.

Acknowledgements

I would like to take this opportunity to thank the many people who have been helpful to me over the last couple years. Some have contributed with knowledge, others with friendship and many (well, most) have provided both.

Both for me and for my supervisor, Jayanne English, the experience was a new one; Jayanne being new at the role of advisor and me being new at the role of graduate student. Together we figured out the deadlines and the requirements and in the end, the result is some interesting science.

Without the support (and the data!) of Magdalen Normandeau, this thesis would not have been possible. Thanks also to Jo-Anne Brown who provided me with some of the polarization data and algorithm to process it! Additionally, I would like to thank Gilles Joncas for observing an Hα field at my request.

I am very grateful for the opportunity I had to spend two great months in Penticton, B.C. at the Dominion Radio Astrophysical Observatory. In my time there, I was able to immerse myself in the radio astronomy world and as such I was able to absorb much from the many knowledgeable and friendly people around me. I am especially thankful to Tom Landecker who made me feel very welcome and for leading me through the difficult task of understanding radio polarization; and to Roland Kothes who patiently helped me to process and mosaic the data used in this thesis and who was always willing to answer my many questions be it by email or in person. I would also like to thank others at DRAO

for helpful and illuminating conversations, notably Andrew Gray and Chris Brunt. In addition, there are many from the International Galactic Plane Survey consortium who gave me encouraging words and helpful suggestions including Marijke Haverkorn, Tyler Foster, and Dave Routledge.

Closer to home, I would like to thank my advisory committee Richard Bochonko, Samar Safi-Harb, and Kumar Sharma for advice and suggestions along the way. Ian Cameron, who had the (mis-?)fortune of being my office neighbour was always willing to talk and provide some encouragement whenever I was confused, frustrated, or just exhausted. Thanks also to Ashish Askegar, Kumar and Ian for reading through my thesis in short order and providing many helpful comments. Thank you to Shelly Page and Norm Davison for helpful discussion.

Family and friends have been invaluable for keeping me sane over the past couple years. Many thanks to my mom, sisters, brother-in-law, nieces and nephew for love and much needed diversions from the university life. Thanks to my good friends and fellow graduate students Marjorie Gonzalez and Jenny Chuang... you went through it with me. And finally thanks to my many friends in the RASC who helped me keep connected to the "real" sky.

Table of Contents

List of Figures

List of Tables

1: Goals and Motivation

In section 1.1 the structure of the Milky Way Galaxy and its halo are described. The W4 chimney is introduced and the possible role it may play in creating some of our Galaxy's structure is explored. Section 1.2 describes the previous research on W4 and in section 1.3 outstanding questions surrounding the W4 chimney candidate are presented and our methods of investigating these questions are summarized.

1.1 Introduction to disk-halo interaction

Acquiring a detailed understanding of Galactic structure and kinematic behaviour is one of the important endeavours in astronomy today since it leads to an understanding of the evolution of galaxies in general. Our own Milky Way Galaxy provides a unique opportunity to study the structure in much more detail than is offered by other galaxies due to their great distances from us. The current picture of our Galaxy consists of a thin disk and central bulge containing luminous stars and a thicker disk containing a more diffuse distribution of stars. Accompanying the stars in the disk are dust, hot ionized gas, and cooler, neutral atomic and molecular gases that emit at radio wavelengths. The disk is embedded in a spherical distribution of stars, globular clusters, cosmic rays and diffuse, hot gas with highly ionized particles (CIV, SiIV, NV) (Normandeau & Basu 1999) as

well as X-ray emission. When away from the plane of the disk, this distribution is referred to as the *halo*.

The Sun is located at a Galactocentric radius of about 8.5 kpc (Binney & Merrifield 1998). The visible disk extends 4 to 6 kpc beyond our Sun (see Figure 2-10 for a plan view schematic diagram of part of our Galaxy) while the HI disk has a Galactocentric radius of ~21 kpc (Binney & Merrifield 1998). Most neutral hydrogen gas is near the Galactic plane. Lockman, Hobbs, & Shull (1986) estimate that the HI nearest the mid-plane has a vertical Gaussian distribution with σ_z = 135 pc. There is a tail to this distribution that can be characterised by an exponential density drop off with a *scale height*[1] of ~500 pc (Lockman et al. 1986). Dickey & Lockman (1990) characterise the HI as a combination of two Gaussians and an exponential. The total distribution has a FWHM of 230 pc. The consensus is that the *halo* begins to dominate above 500 pc and is characterized by a scale height of ~3 kpc (Normandeau & Basu 1999, and references therein) with the bulk of the diffuse ionized gas being contained within the "Reynolds Layer" which extends up to about 1 kpc above the mid-plane (Reynolds 1991).

In order to produce ionized particles, the gas in the halo must have a temperature of at least tens of thousands of Kelvin or in the case of the X-ray emission, millions of degrees. Since the typical cooling time for this hot gas is of the order 10^6 or 10^7 years (Norman & Ikeuchi 1989), there must be some energy input to the halo to explain why the hot gas has not cooled in the Galaxy's 13 billion year history.

---

[1] Scale height in general is used to mean the height at which the density drops by a factor of 1/e.

Theorists suggest that supernovae and/or winds from massive stars existing in clusters confined to the disk produce bubbles in the interstellar medium which expand and burst out of the Galactic disk producing collimated outflows of UV photons and cosmic rays to the Galactic halo (Norman & Ikeuchi 1989). A singular massive star may produce a bubble while a group of massive O and B type stars may produce a *superbubble*. A single star bubble would have scales on the order of tens of parsecs (Chu, Gruendl & Guerrero 2003) whereas superbubbles have typical scales of 100-1000 pc and typical energies of 10^{54} ergs (Norman & Ikeuchi 1989). As a superbubble expands, it will eventually reach a point where it fragments and bursts resulting in a *chimney* (de Avillez & Berry 2001 and references therein, eg. Tomisaka & Ikeuchi 1986) (Figure 1-1). Burst bubble walls or cavities in atomic hydrogen that act as conduits for these outflows. In addition, it is predicted that these conduits should have twisted, toroidal magnetic field lines running roughly parallel to the Galactic plane (Norman & Ikeuchi 1989).

Theoretical predictions estimate that there should be many more disk-halo conduits than have so far been identified. Estimates of the number of conduits range from 1000 (Norman & Ikeuchi 1989) to between 50 and 100 (Heiles et al. 1996). Although only four or five chimney candidates have been identified observationally (Normandeau & Basu 1999; McClure-Griffiths et al. 2000), this particular energy transport mechanism is the most widely accepted. One such candidate is an unusual, cone shaped void observed in neutral hydrogen (Normandeau 1996) above the star cluster OCl 352 and the discrete

radio source, W4[2]. In Normandeau's (1996) data this void did not appear to be closed at the top and so was nicknamed the "W4 Chimney".

In theory, chimneys require the existence of an energy source at the base to create the initial bubble and to power the outflow. The only known phenomena that would produce sufficient energy are supernovae or the combined winds of several supermassive O or B-type stars and the chimney formation theories suggest all such regions should be blowing chimneys. In the case of the chimney candidate, W4, it is proposed that the region has been evacuated of HI by the winds of 9 O-type stars (Normandeau, Taylor and Dewdney 1996, hereafter NTD96) that are part of the open cluster OCl 352. In this case the stellar wind scenario is favoured since the cluster seems too young to have had any supernovae occur and that the energy output of the winds appears to be sufficient to account for the void. Estimates of the age of OCl 352 range from 1.3-2.5 Myr (Dennison, Topasna and Simonetti 1997, hereafter DTS97 and references therein) to 3.7-4.3 Myr (NTD96).

Using Hα observations, Dennison et al. (DTS97) suggest that the region above W4 is not a chimney, but rather a superbubble. The picture of a superbubble is that of a low density cavity which is ionized on the inside due to ionizing radiation from the stellar winds of O-type stars and which is bounded by a thin HI shell (Tenorio-Tagle & Bodenheimer 1988, de Avillez & Berry 2001). OCl 352 is positioned at the base of the superbubble observed by DTS97 and referred by them as "SC" (see Figure 4-2). However the DTS97

---

[2] W4 was first identified by Westerhout (1958) in his "Survey of the Continuous Radiation from the Galactic System at a Frequency of 1390 Mc/s", hence the "W" designation.

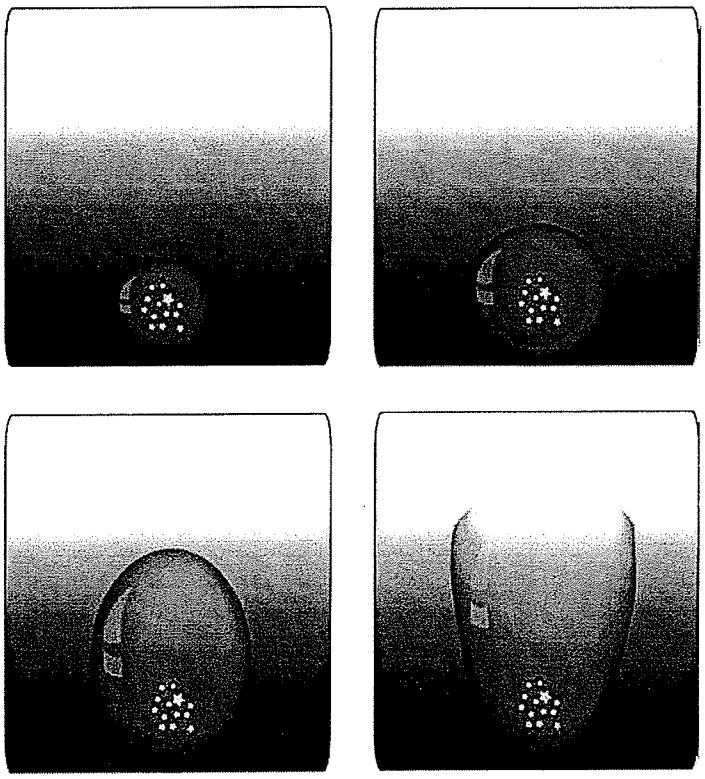

Figure 1-1: Cartoon drawing showing the evolution of a superbubble into a chimney. A spherical bubble begins to be blown around an OB association (top left) due to their combined winds or supernova events. The bubble continues to expand spherically (top right) until it grows to where its radius is of the order of the Galactic scale height (Tenorio-Tagle & Bodenheimer 1988) at which point the expansion in the vertical direction begins to accelerate (bottom left). As it expands further, the density of the ISM becomes so tenuous and the expansion accelerates to the point where the top of the bubble becomes unstable and fragments, resulting in a chimney (bottom right).

data suffers from substantial vignetting at the field edges that could possibly lead the eye to seeing a bubble shape where none exists (see Figure 3-12). This makes corroboration from other datasets desirable.

Additional high latitude observations were obtained at the Dominion Radio Astrophysical Observatory (DRAO) by M. Normandeau (private communication) extending to b = 9°, or about 360 pc at an assumed distance of 2.3 kpc which extends above σ = 135 pc of the Gaussian HI distribution and extends well into the exponential component (see earlier this section). These observations include atomic hydrogen spectral line data as well as radio continuum and radio polarization data. Some analysis has been done on the spectral line data by M. Normandeau (private communication), but her continuum and polarization data had yet to be fully analysed for evidence supporting or refuting the theory that this structure is a chimney. Such supporting evidence in the continuum and polarization datasets would include morphological features suggestive of collimated gas outflow, features in polarization suggestive of magnetic field lines parallel to the Galactic plane, or a spectral index suggestive of convective cosmic ray transport. In this thesis the radio continuum and polarization datasets are explored.

1.2 Previous research on W4

The W3/W4/W5 region, a star forming complex in Cassiopeia at a distance of ~2.3 kpc (Normandeau 2000), was chosen as the pilot project for the Canadian Galactic Plane Survey (CGPS) (Normandeau 1996). This survey used the Synthesis Telescope at the

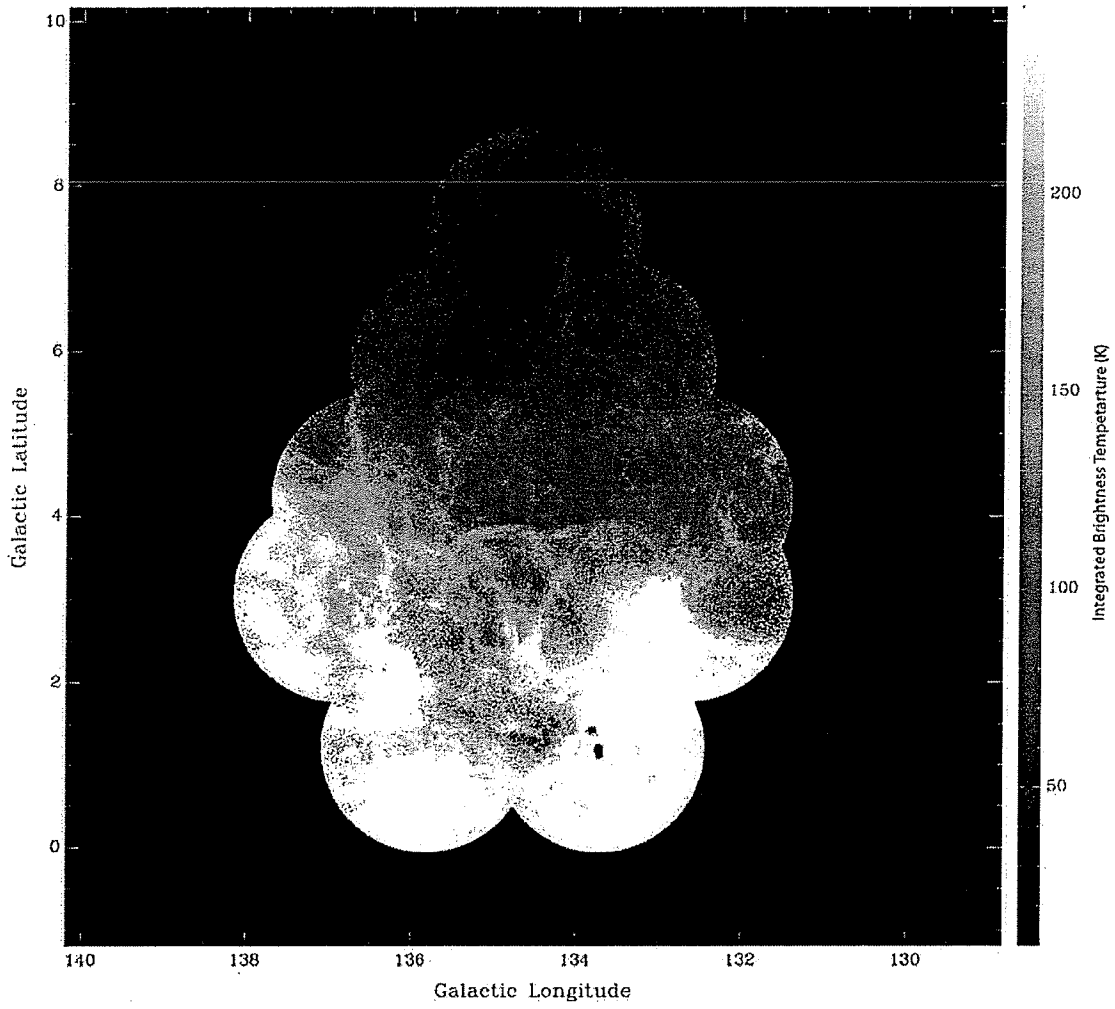

Figure 1-2: HI spectral line image (Normandeau, 2000). Intensity has been integrated over four velocity channels from $v = -40.11$ km/s to $v = -45.05$ km/s. Grey scale shown is in Kelvin (see right). Latitude and longitude scales are in degrees.

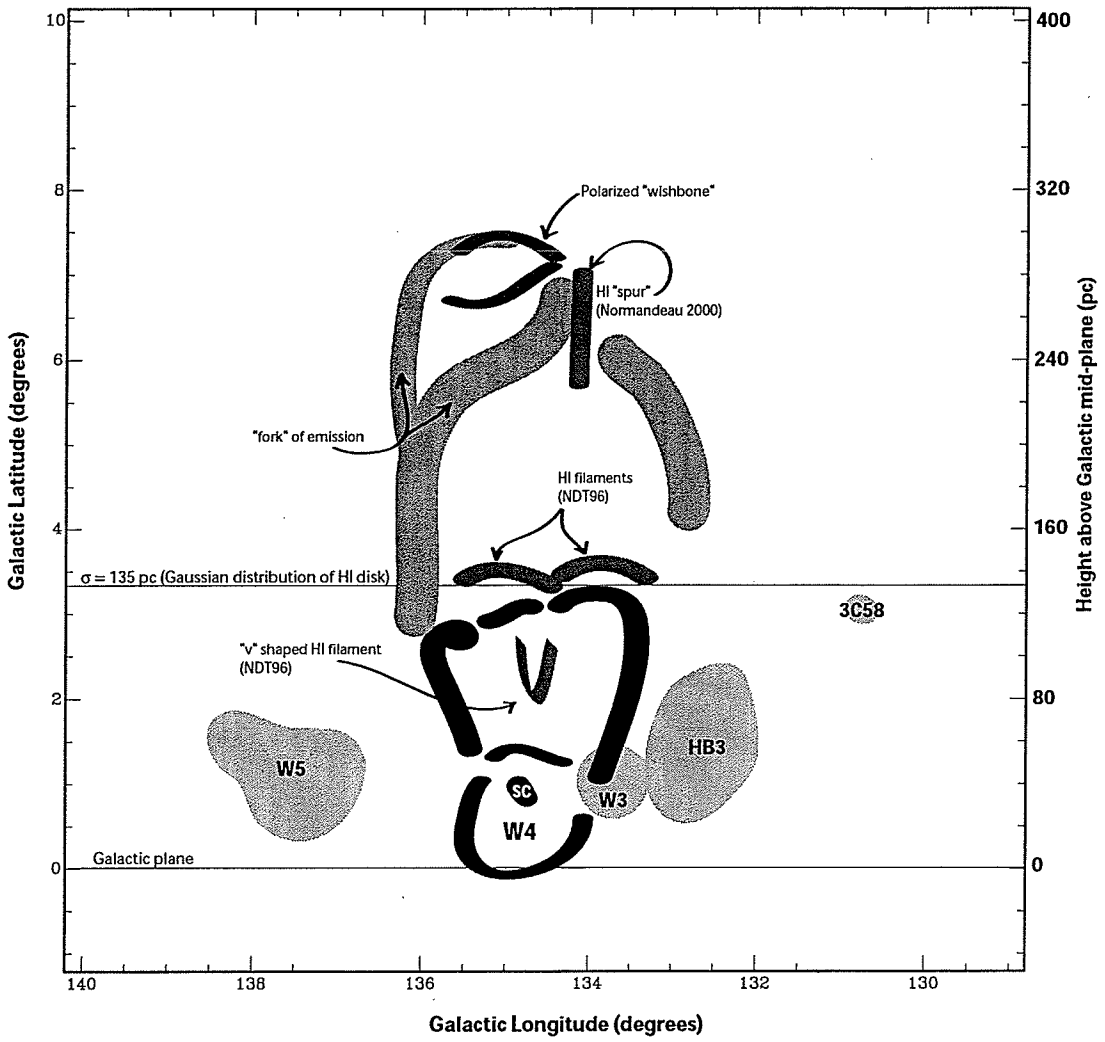

Figure 1-3: Schematic diagram of the W3/W4/W5 region, including the supernova remnants HB3 and 3C58. The region marked "SC" identifies the location of OCl 352. The HI features ("spur", filaments, and "v" shaped "rabbits ears") are visible in Figure 1-2. Other features such as the polarized "wishbone" and "fork" of emission are visible in the other datasets which are introduced in Chapter 3 (see Figure 3-21 for labels on an image that combines the other datasets using colour).

Dominion Radio Astrophysical Observatory (DRAO) (Landecker et al. 2000). The CGPS data includes neutral hydrogen spectral line observations at 1420 MHz as well as radio continuum observations at 1420 MHz and 408 MHz (see Chapter 3 for details). Normandeau et al. (NTD96) describe the unusual void apparent in the neutral hydrogen data above (i.e. towards the North Galactic Pole) W4 that has become known as the W4 Chimney. However, the CGPS data has an extent of 5° latitude, or ~200 pc at our adopted distance of 2.3 kpc, above the plane of the Galaxy which is not sufficient to define a boundary for the region above W4. The void is visible in Figure 1-2 which includes recently acquired data extending up to a latitude of ~8°. Figure 1-3 is a schematic diagram of the region that labels many of the features visible in the HI data (Figure 1-2) in addition to features visible in the other datasets and which will be discussed later in this thesis.

As one can see in Figure 1-3, the region is complex and contains much more than just W4. However the other objects in the region show little evidence of contributing to the observed HI void. The very young, compact HII region, W3, shows no indication that it has an expanding HI shell or that it is disturbing its surroundings (Normandeau 1996). Its stars are still embedded in the surrounding molecular cloud and there is little evidence of associated HI except as a strong absorption feature. The W5 region is excited the cluster OCl 364 and although it is likely at a similar distance from the sun as W3 and W4, there does not appear to be any evidence that there is significant interaction between the regions (Normandeau 1996). The supernova remnant, HB3, is thought to be located at a

distance just slightly further than W3 (Normandeau 1996). Thus it is thought that W3, W5, and HB3 do not contribute to the observed HI deficiency above W4.

A gas outflow may be suggested in the morphology of the region. The low latitude data shows a "v" shaped filament in neutral hydrogen (see Figure 1-2 and Figure 1-3) with a counterpart in molecular CO. The material has a velocity gradient suggesting it is moving up and towards the observer and may be indicative of outflow (NTD96). There is also a "spur" of neutral hydrogen visible in the high latitude neutral hydrogen data that extends from ~(134.15°, 6.083°) to ~(134.175, 7.25) (Normandeau 2000) and that may suggest an outflow.

Reynolds, Sterling and Haffner (2001) have observed a very large loop in Hα data from the Wisconsin Hα Mapper (WHAM) extending to ~30°, or 1200 pc at our adopted distance of 2.3 kpc, above the Galactic plane (Figure 1-4) which is well into the halo. The base of this loop is roughly coincident with the W4 region (see Figure 1-4), the velocities are consistent with the velocities of the HI void and the OB cluster at the base of the void is a possible energy source for blowing out the loop. These observations lead the authors to suggest that this large loop is actually a blowout from the W4 region. The DRAO continuum data for latitudes >4° has been analysed in this thesis in order to confirm this relationship or to provide other suggestive morphological features.

Evidence presented by DTS97 contends that the region above W4 is not a chimney, but rather a superbubble. They claim the region appears to be a closed superbubble observed

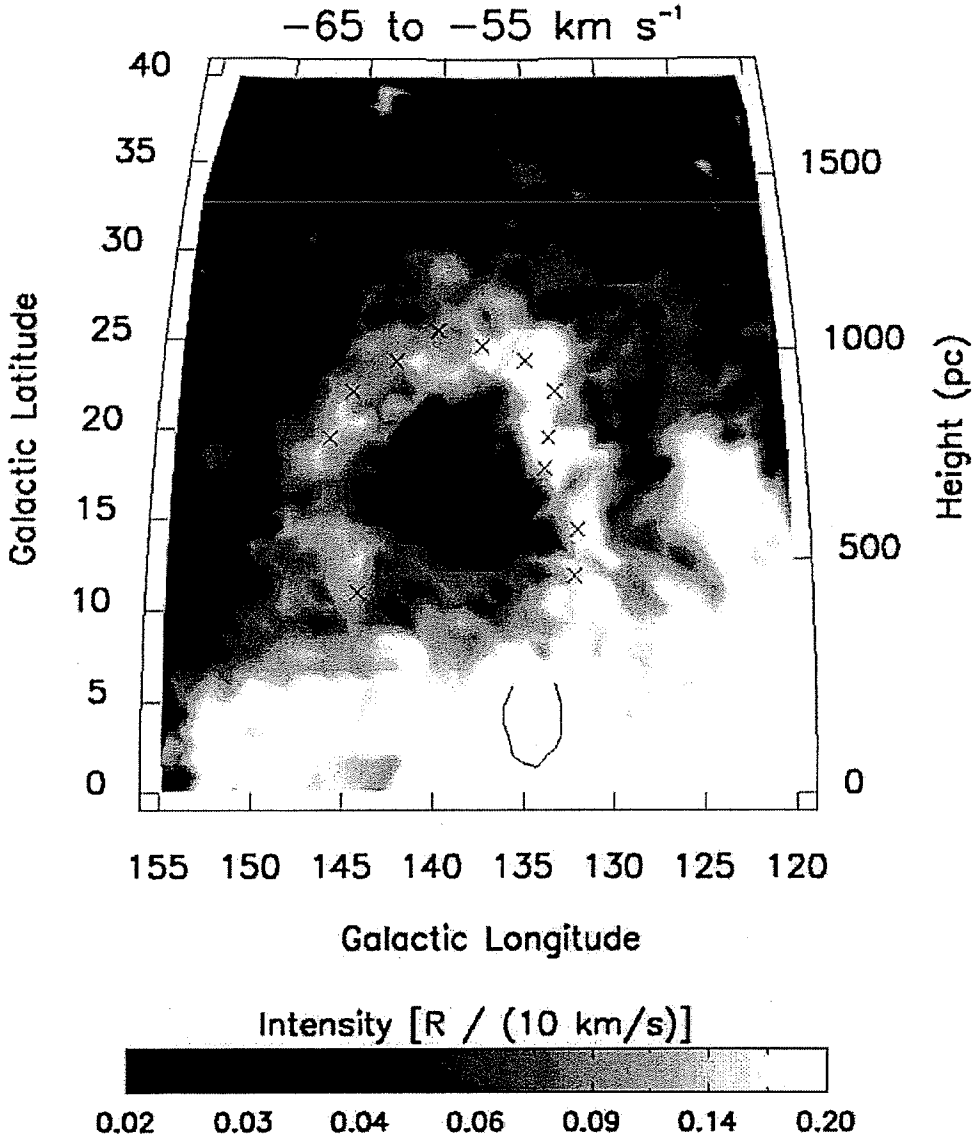

Figure 1-4: WHAM Northern Sky Survey image of the loop of ionized hydrogen extending to $b \sim 30°$ above the position of the W4 Chimney (reproduced with permission from Reynolds et al. 2001) in the velocity interval –65 km/s to –55 km/s. The horseshoe figure indicates the position of the Chimney and the crosses indicate positions of velocity plots presented by Reynolds et al. (2001). Grey scale in Rayleighs [R] (see definition in section 4.2.1) and shown at bottom. Latitude and longitude scales are in degrees.

in ionized hydrogen emission. They also suggest that the ionizing radiation from the cluster is mostly contained within a region that is relatively close to the cluster. They calculate the expected intensity in the upper limb of the superbubble to be ~5 times greater than the measured value. To explain this deficiency they claim that two small molecular CO clouds, near the cluster, immediately above a small loop of ionized gas surrounding the cluster, trap the gas and allow only a small amount to escape. The upper filament of the loop is labeled as point "O" in Figure 4-2.

According to DTS97, the radiation that does escape ionizes the observed superbubble and thus does not escape from the region and does not contribute to the diffuse ionized Reynolds layer. However, the Hα data used to reach these conclusions suffers from artefacts and will therefore be reanalysed in the context of newly available data at other wavelengths in an effort to determine if a superbubble does exist. Also, if a superbubble exists that is not completely impermeable, we expect to find evidence for both outflow and some containment.

Terebey et al. (2003) suggest that the extinction correction applied to the DTS97 data may be too large and that fewer photons are trapped than Dennison et al. suggest. After examining the DRAO 1420 MHz and IRAS 60 and 100 μm datasets for the region immediately surrounding OCl 352, they find 40% ± 16% of the ionizing photons are allowed to escape to >60 pc above the cluster. Their conclusion is that these photons contribute to the ionization of the diffuse ionized gas and the upper Galactic halo.

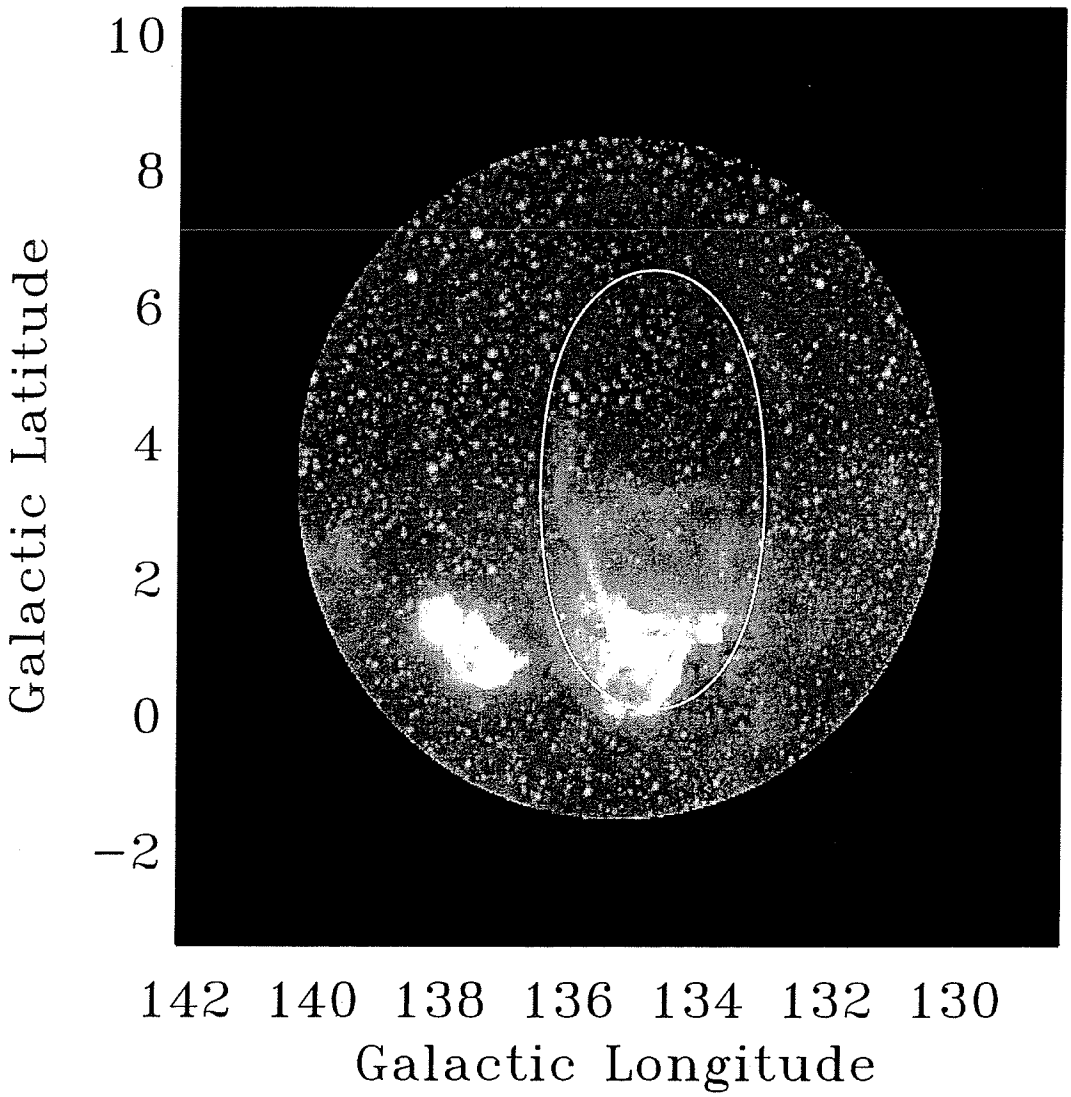

Figure 1-5: Best-fit Kompaneets model (white oval) to the DTS97 Hα data (BJM99). Grey scale shown has white as the most intense emission and black as the least intense. Latitude and longitude scales are in degrees. Figure is reproduced with permission from BJM99.

The Hα superbubble observed by DTS97 was modeled by Basu, Johnstone and Martin (1999, hereafter BJM99) using a simple 2D model of a shock wave propagating in an atmosphere which has an exponential drop-off in the vertical direction. This model is known as the Kompaneets approximation. Basu et al. (BJM99) assume that the expansion takes place through a continuous energy input via the stellar winds. The ISM is assumed in this model to be a uniform medium that decreases in density out of the plane of the Galaxy and that is characterized by an exponential scale height.

The model superbubble profile seems to fit the data (see Figure 1-5), however it forces a scale height of $H \sim 25$ pc which contradicts the mean scale height of the Galaxy, H>~100pc (Normandeau & Basu 1999). Basu et al. (BJM99) suggest the vertical compression is likely to have occurred in the presence of the W3/W4/W5 star forming complex decreasing the expected scale height. However, the scale height of the region has been measured to be $H \sim 140$ pc using the HI spectral line data (Normandeau 2000) which does agree with the mean Galactic value and therefore suggests that the model is either too simple or inappropriate. In an effort to determine whether the superbubble scenario is appropriate, regardless of whether or not the Kompaneets model is appropriate, part of our analysis focuses on searching our data for coincidences with Dennison et al.'s (DTS97) Hα data by comparing morphological features.

The chimney model of Norman & Ikeuchi (1989) and the bubble model of Basu et al. (BJM99) predict that the magnetic field of W4 should be tangential to its shell. Such a field within the shell is produced as the Galactic magnetic field, that is thought to be

oriented parallel to the disk of the Galaxy, is "frozen" into the plasma and is thus "pulled" upwards with the shell material as the bubble expands. It is proposed that magnetic field in such an orientation may act to stabilize the structure (BJM99).

The polarization data from the pilot survey data was presented by Gray et al. (1999). They found Faraday rotation effects in the background Galactic synchrotron emission in the direction towards W3/W4/W5. These effects are observationally recognized by depolarized regions that follow the contours of the HII regions. If in the present polarization data, we observe the depolarization continuing to follow the contours of Dennison et al.'s (DTS97) superbubble, it would support the theory that the observed Hα emission is occurring at the same distance as W3/W4/W5. Figure 1-6 illustrates the effects of Faraday rotation on emission passing through the superbubble and what we expect to observe if such a process is occurring. A description of polarization and Faraday rotation is presented in section 2.2.

It would be useful to examine Hα Fabry-Perot data to determine if superbubble features apparent in the DTS97 data have corresponding features that reside at the same velocities as W4's HI structure. If they do, it would provide further motivation for more realistic 3D modeling of the region. Such data has been collected in this region by G. Joncas in the fall of 2002 at Mont Megantic but has not been processed as of yet and thus was unavailable for analysis at the time of this writing.

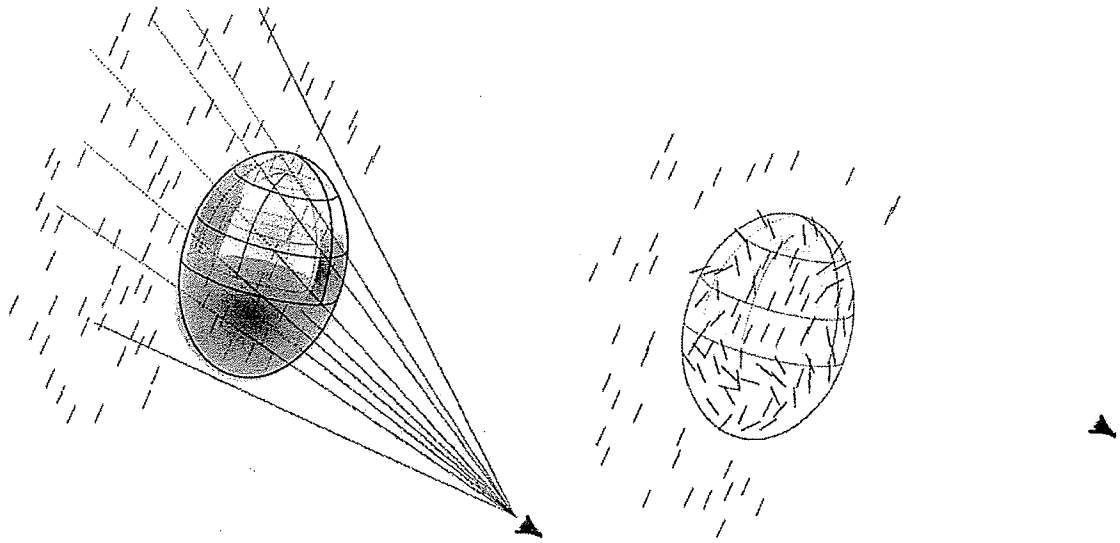

Figure 1-6: A uniform polarized background observed through an ionized region (shown at left) will be scrambled due to Faraday rotation (shown at right). The polarized emission for lines of sight not passing through the ionized region will be unaffected. The polarization vectors with lines of sight passing through the projected center of the egg-shaped region are affected, but not as dramatically as those with lines of sight passing through the walls. Note that small lines represent the polarization vectors which initially have a uniform but arbitrary position angle (left).

1.3 Outstanding questions

This thesis will extend the research on the chimney candidate, W4 (Normandeau 2000) in an attempt to answer some of the outstanding and inter-related questions:

1. Is the object a chimney or a superbubble?
2. Is it open or closed?
3. If it is a superbubble, is it broken? Permeable?
4. Is anything escaping such as hot ionized gas or cosmic rays?

5. Is any gas contained within the bubble-like region or has it been evacuated?

In Chapter 2 we begin by presenting the background material required to understand the analysis and the discussion. A description of radio emission in the Galaxy is included. How the spectral index may be derived from the detected emission and the relevance of the spectral index is also explained. A description of radio polarization is presented with emphasis on Faraday rotation and the measurement of that quantity. The technique of radio interferometry is then briefly described.

In Chapter 3 the newly processed DRAO data combined with some of the CGPS survey data are presented. Additionally, the Virginia Tech Hα data of DTS97 is presented reprocessed to remove the point sources. Colour versions of many of the images have been produced in various combinations as a means to more easily interpret and compare the morphology of the region that is visible in the datasets. These colour images are presented at the end of Chapter 3.

In order to probe the interior of the superbubble or chimney a spectral index map has been produced. The spectral index map may reveal the dominant mode of emission (i.e. thermal or non-thermal) in the region. The spectral index could also suggest whether cosmic rays are present in the superbubble or chimney interior, whether they are transported via diffusion or convection, and if they have sufficient energy to escape. This map is presented in the first part of Chapter 4.

In the second part of Chapter 4 a rotation measure map produced from the polarization data has been produced to explore the magnetic field of the region. This exploration may reveal whether a tangentially oriented (BJM99) magnetic field is reasonable. The rotation measure may indicate the dominant direction of the line of sight component of the magnetic field of the W4 region and in the surroundings. In addition, with the available Hα data of DTS97 the electron density of the region may be estimated. The electron density combined with the rotation measure will make possible an estimate of the magnetic field strength.

In Chapter 5 the discussion focuses on a morphological examination of the radio continuum data at 1420 and 408 MHz as well as radio polarization data at 1420 MHz. We look for morphological evidence and coincidences that support or refute the Hα superbubble evidence of DTS97. The integrated HI image produced by Normandeau (2000) is re-examined in light of the newly processed data. This leads to the scenario of a superbubble that is sufficiently evolved that it is fragmenting.

Some interesting features appear in the polarization and 408 MHz datasets but which are not likely related to W4. These features are briefly discussed at the end of Chapter 5.

2: Galactic Radio Emission: Its Origins and Techniques for its Detection

This chapter describes the background material necessary to understand the analysis. Section 2.1 describes the types of radio emission one expects to detect in the Galaxy including non-thermal synchrotron and thermal emission and some analysis techniques employed on our data. In section 2.2 radio polarization and the important concept of Faraday rotation and its contribution to depolarization is explained. Section 2.3 describes information necessary to understanding the data including Fourier transforms and radio interferometry techniques.

2.1 Radio emission in the Galaxy

At radio frequencies, and for typical interstellar temperatures, we find that $kT >> h\nu$ (i.e. interstellar temperatures, $T >> h\nu/k$ = 0.07 K for ν = 1420 MHz) and one may make an approximation known as the Rayleigh-Jeans limit. In this regime

$$S_\nu(T_B) = \frac{2\nu^2 kT_B}{c^2} = \frac{2kT_B}{\lambda^2} \qquad (2\text{-}1)$$

where S_ν is the radio intensity in Jy/beam, ν is the frequency of observation, c is the speed of light, k is Planck's constant and λ is the wavelength of observation, and T_B is "brightness temperature".

The intensity of radiation at radio wavelengths is often measured in units of brightness temperature which is expressed in Kelvin. In the Rayleigh-Jeans regime, the brightness temperature, T_B, of a radio source is approximately equivalent to the temperature of a blackbody which would produce the detected emission (Rohlfs & Wilson 2000). Note that this is not necessarily equivalent to the thermodynamic temperature of the source as blackbody radiation is not typically the process responsible for the emission.

The thesis data, collected at 1420 MHz and at 408 MHz, is at wavelengths where detected emission at large scales is dominated by synchrotron radiation with a lesser contribution from thermal sources. At smaller scales, such as in star forming regions like W4, thermal radiation contributes significantly to the overall detected emission.

2.1.1 Synchrotron emission

Synchrotron emission occurs when relativistic charged particles, typically free electrons, spiral along the field lines in a strong magnetic field (Bowers and Deeming 1984). To help understand the process of synchrotron emission we examine the simpler radiation, of the same form, that occurs for non-relativistic particles and that is called cyclotron

radiation. An electron, e, moving with a velocity, v, experiences a force, **F**, due to the magnetic field, **B**, equivalent to

$$\mathbf{F} = \frac{ev \times \mathbf{B}}{c} \qquad (2\text{-}2)$$

This force causes the particle to move along a circular path of radius r, since there is no component of **F** along the direction of the field and thus the velocity of the particle in this direction remains constant. The frequency of the circular motion, ν, is

$$\nu = \frac{v}{2\pi r}. \qquad (2\text{-}3)$$

The centripetal acceleration of the particle, $\frac{v^2}{r}$, is equivalent to its magnetic acceleration, $\frac{F}{m}$, where m is the mass of the particle and F is given by Eq. (2-2). Setting these equal to each other and substituting Eqs. (2-2) and (2-3) we find

$$\frac{(2\pi r\nu)^2}{r} = \frac{eB_{\perp} 2\pi r\nu}{mc}. \qquad (2\text{-}4)$$

Here $B_\perp$ is the component of **B** that is perpendicular to v. Solving for ν we find the frequency of the emitted radiation for a non-relativistic particle

$$\nu = \frac{eB_\perp}{2\pi mc}. \qquad (2\text{-}5)$$

Particles attain relativistic velocities when they are accelerated by a shock from an energetic event like a supernova. A shock may also arise from the combined winds of several supermassive O and B-type stars in an OB association. If the particle is moving with relativistic velocities, the frequency of the emitted radiation becomes

$$\nu = \frac{eB_\perp}{2\pi mc}\left(\frac{E}{mc^2}\right)^2 \qquad (2\text{-}6)$$

(Bowers & Deeming 1984) where E is the energy of the particle. Radiation is emitted at ν and at harmonics of ν. In the case of relativistic electrons, the harmonics are closely spaced that produces an essentially continuous spectrum.

The relativistic motion of the electrons cause the emitted radiation to be highly directional. Due to this "relativistic beaming" effect and due to the fact that the electrons spiral along parallel to the magnetic field lines, the observed radiation is confined to a narrow conical shell (not to be confused with the cone shaped "beams" of emission). The cone (Figure 2-1) is characterized by the pitch angle of the electrons helical motion, α,

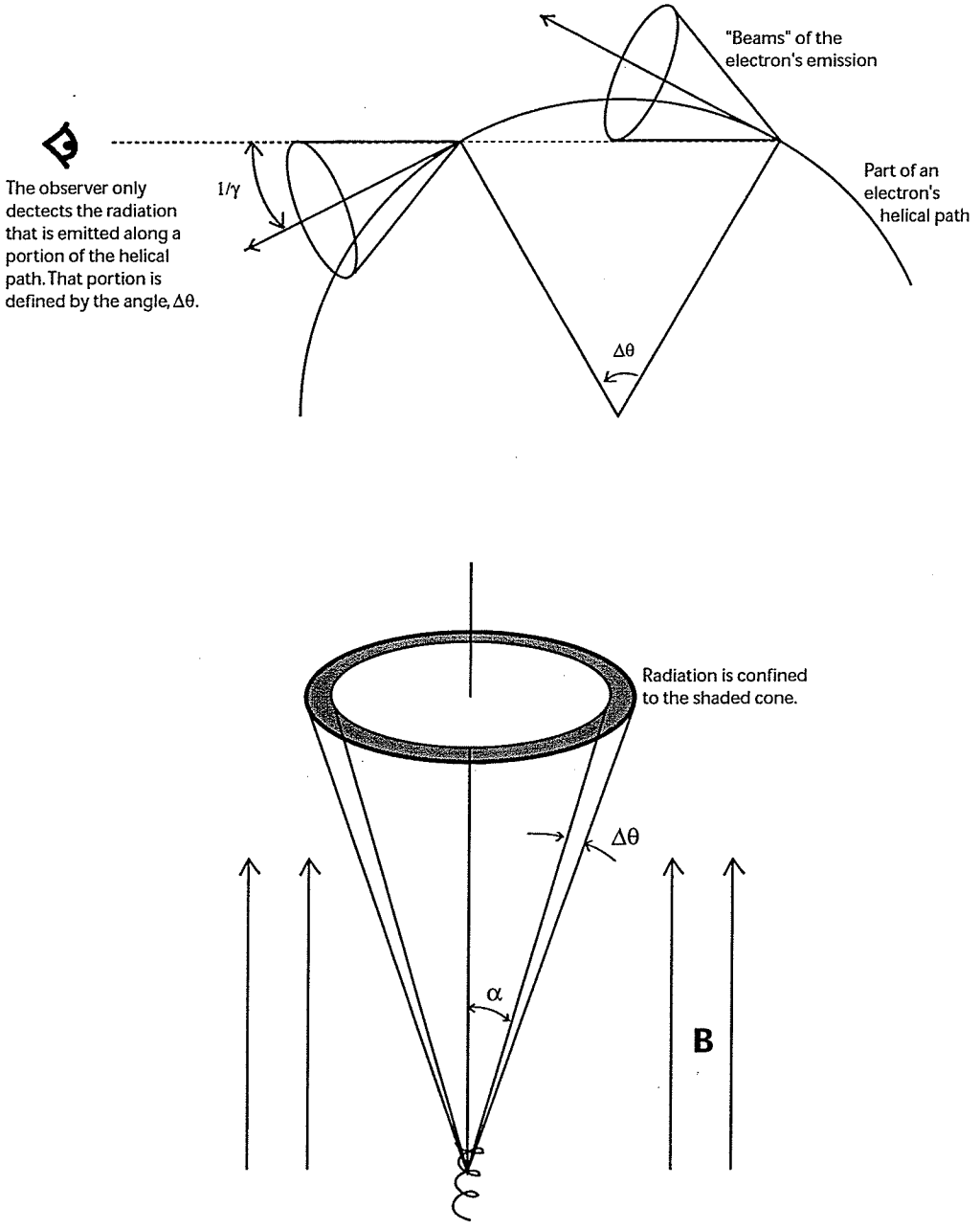

Figure 2-1: Synchrotron emission from a particle with the pitch angle of its helical path, α. The observer sees the radiation confined to a narrow conical shell of width Δθ and of opening angle, α. The relativistic "beams" have an opening angle that depends on the electron's velocity ($\frac{1}{\gamma} = \sqrt{1 - \frac{v^2}{c^2}}$).

Figures adapted from Rybicki & Lightman (1979).

and its axis being parallel to the local magnetic field. This directionally emitted radiation in the presence of a magnetic field leads to the polarized nature of the emission (Bowers & Deeming 1984).

The total power, P, radiated by a relativistic electron is expressed as

$$P = \frac{2}{3}\frac{e^4\gamma^2 B^2(\sin\alpha)^2}{m^2c^3} \text{ where } \gamma = \frac{1}{\sqrt{1-\frac{v^2}{c^2}}} \qquad (2\text{-}7)$$

(Burke & Graham-Smith 1997).

This simplified description is applicable for a single electron when in fact an ensemble of electrons with a distribution of pitch angles and energies must be considered. Rohlfs & Wilson (2000) provide a description of synchrotron radiation from such an ensemble. Thus, emission at radio frequencies can occur with particles of particular energies in a magnetic field of the appropriate strength. For an ensemble of electrons that is isotropic and homogeneous we find that the energy spectrum has a power law form.

2.1.2 Thermal radiation

Less significant to the ambient Galactic emission is the contribution of thermal emission from free electrons. Any hot plasma, such as that found in star forming regions like W4, will emit in the form of thermal radiation at radio wavelengths. This radiation occurs when electrons are rapidly accelerated or decelerated and is sometimes called free-free radiation or Bremsstrahlung, literally "braking" radiation. The acceleration can occur when electrons experience attractive or repulsive forces in the plasma when approaching protons or other electrons.

Absorption may also take place in this process which makes Bremsstrahlung a primary contribution to the opacity of the gas, κ_ν. The absorption is both temperature and frequency dependent. Observations of emission lines in HII regions have implied a temperature of $\sim 10^4$K and thus one can determine the intensity of the expected blackbody radiation that would be observed at a frequency which is opaque to Bremsstrahlung.

At low frequencies a gas becomes completely opaque to Bremsstrahlung and one says the gas is *optically thick*; that is, a gas in which the mean free path is much smaller than the distance through which a photon must travel. The ratio of distance traveled in the medium to its mean free path is referred to as the *optical depth*, τ. The optical depth measures how many mean free paths exist along a particular line of sight (Bowers & Deeming 1984). Optical depth may also be expressed in terms of the opacity, κ_ν

$$\tau_\nu = \int_0^x \kappa_\nu dl \qquad (2\text{-}8)$$

In an optically thick medium, i.e. a medium where $\tau >> 1$, thermal radiation will have a blackbody spectrum.

At higher frequencies the mean free path of an electron is much greater than the distance through which it must travel and the gas is said to be *optically thin.*

Mathematically, the thermal intensity S_ν can be expressed as

$$S_\nu = \frac{j_\nu}{4\pi\kappa_\nu}\left[1 - \exp(-\kappa_\nu x)\right] \qquad (2\text{-}9)$$

(Longair 1997) where j_ν is the emissivity of the gas and is expressed in terms of the Einstein emission coefficient (see Longair 1997). The important thing to note in Eq. (2-9) is that the term in the exponential is the optical depth, τ, integrated along the line of sight from 0 to x. Thus, if $\tau << 1$, Eq. (2-9) reduces to

$$S_\nu = \frac{j_\nu x}{4\pi} \approx \text{constant}. \qquad (2\text{-}10)$$

Similarly, if $\tau >> 1$, Eq. (2-9) reduces to

$$S_\nu = \frac{j_\nu}{4\pi\kappa_\nu} = \frac{2h\nu^3}{c^2}\left[\exp\left(\frac{h\nu}{kT}\right)-1\right]^{-1}$$

$$= \frac{2kT}{c^2}\nu^2 \qquad \text{if } h\nu << kT \qquad (2\text{-}11)$$

(Longair 1997).

Thus an optically thin gas has an approximately constant intensity as frequency is varied but in an optically thick gas S_ν goes as ν^2.

2.1.3 Spectral index

The brightness temperature is related to the frequency of observation, ν, and the *temperature spectral index*, β, by

$$T_B \propto \nu^{-\beta} \qquad (2\text{-}12)$$

(Steinberg & Lequeux 1963). Thus given observations at two frequencies, one may calculate β

$$\frac{T_{\nu_1}}{T_{\nu_2}} = \left(\frac{\nu_1}{\nu_2}\right)^{-\beta} \qquad (2\text{-}13)$$

$$\beta = -\frac{\log\left(\frac{T_{\nu_1}}{T_{\nu_2}}\right)}{\log\left(\frac{\nu_1}{\nu_2}\right)} \qquad (2\text{-}14)$$

The quantity β has characteristic values for particular types of radiation (i.e. thermal and non-thermal) and so may be used to help distinguish between sources of emission. Thus β may help identify which processes are occurring in a particular region. Often the *spectral index*, α, will be discussed instead of the temperature spectral index, β. It is the *flux density*, S_ν, that is proportional to $\nu^{-\alpha}$ instead of the temperature (recall Eq. (2-12)) as with β. If we recall Eq. (2-1) we see that

$$S_\nu \propto T_B \nu^2 . \qquad (2\text{-}15)$$

Thus one finds that the two indices, α and β, are related by

$$\alpha = \beta - 2 . \qquad (2\text{-}16)$$

Table 2-1 outlines some expected values for these spectral indices in specific phenomena.

The values listed in Table 2-1 are typical for an optically thin medium. Recall that is a medium in which the mean free path is much greater than the distance through which a photon must travel. In the case of an optically thin medium, $\tau << 1$ and virtually no scattering or absorption takes place.

From Eq. (2-10) we see that in the case of an optically thin medium that is dominated by thermal emission, the intensity, S_ν, is approximately constant with changing frequency, ν. Since $S_\nu \propto \nu^{-\alpha}$, the spectral index, α, must be close to zero to satisfy the proportionality. From Eq. (2-16), one sees the temperature spectral index, β, is then ~2.0 or 2.1. Such a spectral index is referred to as being "flat".

However, if $\tau \sim 1$, absorption begins to become important and the thermal spectrum "breaks" since for an optically thick medium, $\tau >> 1$ and we find a blackbody spectrum. For an optically thick medium, instead of $\beta = 2.1$, one expects the temperature spectral index for thermal radiation to be 0 giving $\alpha = -2$ or $S_\nu \propto \nu^2$ as in Eq. (2-11). The *break frequency* occurs around 1 GHz for $\tau \sim 1$ which is between our frequencies of interest (i.e. between 0.408 and 1.4 GHz). The break frequency is located at the frequency where the radio brightness spectra stops increasing and then begins to decrease (see Figure 2-2).

Thus when $\tau \sim 1$, towards lower frequencies $\beta = 0$ (i.e. $T_{408} = T_{1420}$, see Eq. (2-14)) and towards higher frequencies $\beta = 2.1$, for thermal radiation. Consequently we find the

temperature spectral index for thermal regions to be somewhere between 0 and 2.1 because our regions are not necessarily optically thin.

Source of the radiation	Expected spectral index ($S \propto \nu^{-\alpha}$)	Expected temperature spectral index ($T_B \propto \nu^{-\beta}$)
HII region (thermal)	$\alpha \approx 0.1$, flat	$\beta \approx 2.1$
Supernova remnant (non-thermal synchrotron)	$\alpha \approx 0.5$	$\beta \approx 2.5$
Diffuse radio emission (non-thermal synchrotron)	$0.5 < \alpha < 1.1$, steep	$2.5 < \beta < 3.1$

Table 2-1: Expected spectral indices for various types of radiation (Lisenfeld & Völk, 2000 and references therein).

In addition, not all synchrotron radiation will have a temperature spectral index, $\beta = 2.5$. Plerionic type supernova remnants (e.g. 3C58) have a thermal-like temperature spectral index, between 2.0 and 2.3 (Safi-Harb 2002), although the radiation is caused by synchrotron processes. This is due to the fact that the radiation in plerionic remnants comes from the pulsar and thus the energy distribution of the electron ensemble differs from the electron energy distribution arising in shock processes. When synchrotron radiation is discussed in this thesis, it is the radiation due to shocks and thus we use $\beta > 2.5$ and call this "steep".

Lisenfeld & Völk (2000) describe how one may distinguish between different modes of

cosmic ray (CR) transport using the spectral index in the context of other galaxies. These modes are diffusion and convection. In diffusion CRs are randomly scattered by a magnetic field and thus undergo substantial energy losses due to emission of synchrotron radiation (Lisenfeld & Völk 2000). In a simple diffusion model, the CRs spread out from the source into a Gaussian distribution. Diffusion is characterised by an energy dependent diffusion coefficient, D which relates the distance traveled, d, in a time, t, by

$$d \sim \sqrt{Dt} \qquad (2\text{-}17)$$

(Condon 1992). Convection is a systematic movement of the CRs outward from the point of origin. The mechanism usually invoked is the Galactic wind, allowing the CRs to travel with some convection velocity, V (Lerche & Schlickeiser 1980, Owens & Jokipii 1977). The convective flow velocity for chimneys is $\sim 10^2$ km/s over a scale length of ~1-3 kpc (Norman & Ikeuchi 1989).

Diffusion models are characterised by a steep spectral index ($\alpha > \sim -0.9$). The associated synchrotron emission may indicate energy losses which in turn imply that the CRs will not be able to escape into the halo. In observations of diffuse emission, a flatter spectral index ($\alpha < \sim -0.6$) suggests that synchrotron emission is not predominant implying that if CRs exist in the region, they are not caught in a magnetic field and subject to high energy losses via emission of synchrotron radiation. Thus, escape via a convection process is plausible. An intermediate value (i.e. $0.8 > \alpha > 0.7$) would make discriminating between the two modes of transport difficult. (Lisenfeld & Völk 2000).

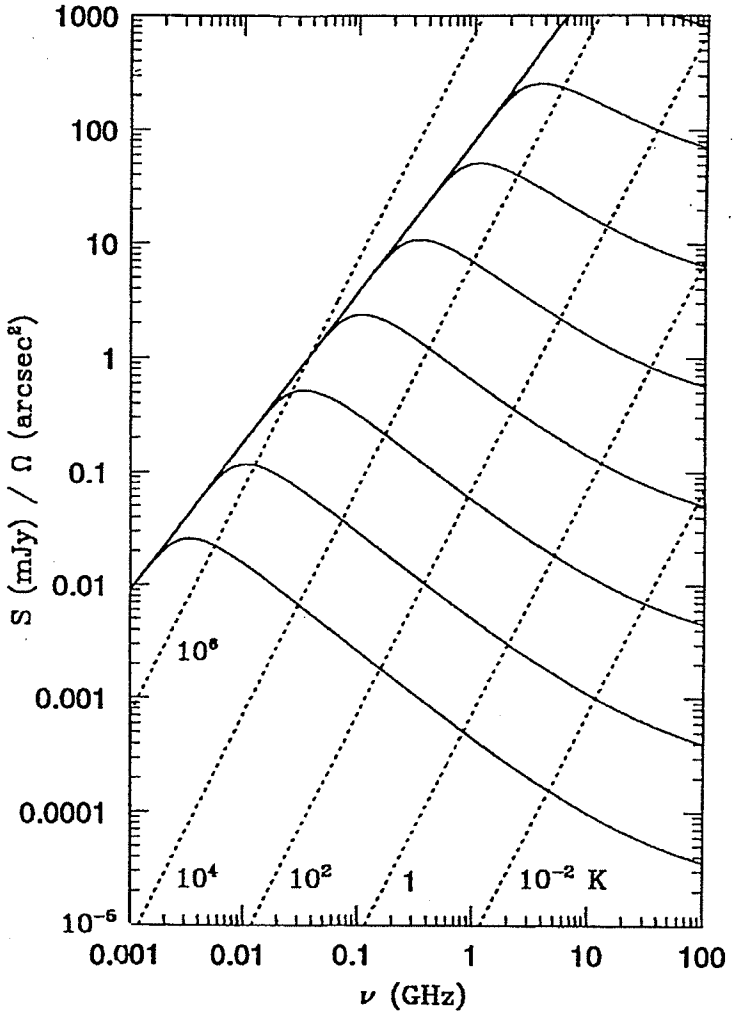

Figure 2-2: Figure reproduced with permission from Condon (1992) illustrating the break frequency. "Successive curves correspond to increasing the frequency ν_1 at which the free-free optical depth is $\tau = 1$: $\nu_1 = 0.003$, 0.01, 0.03, 0.1, 0.3, 1, and 3 GHz." (Condon 1992)

Lisenfeld & Völk's (2000) spectral index analysis is applied to the W4 chimney region because "chimneys" in general are thought to be conduits connecting the disks and halos of galaxies and which are capable of transporting CRs and ionized gas. A diffusion model may dominate if a magnetic field is present within the chimney within which free electrons may become caught, emitting synchrotron radiation and losing the energy necessary to escape. Or there may be an upward directed "wind" in the chimney analogous to the Galactic wind that would carry CRs away from the disk as in the convection model.

2.2 Polarization

It is important to fully understand the concept of polarization in order to interpret the data in this thesis. Radio emission at 1420 MHz is dominated by synchrotron emission which tends to be highly polarized (up to 70%) and in particular, is dominated by linear polarization with a negligible component of circular polarization (Beck 2001).

Linear polarization could be considered the simplest form of polarization and is characterized by an EM wave vibrating parallel to a fixed direction in space and perpendicular to the direction of propagation. That is, when viewed along the axis of propagation (say the z-axis), the motion appears to be in a line (Figure 2-3).

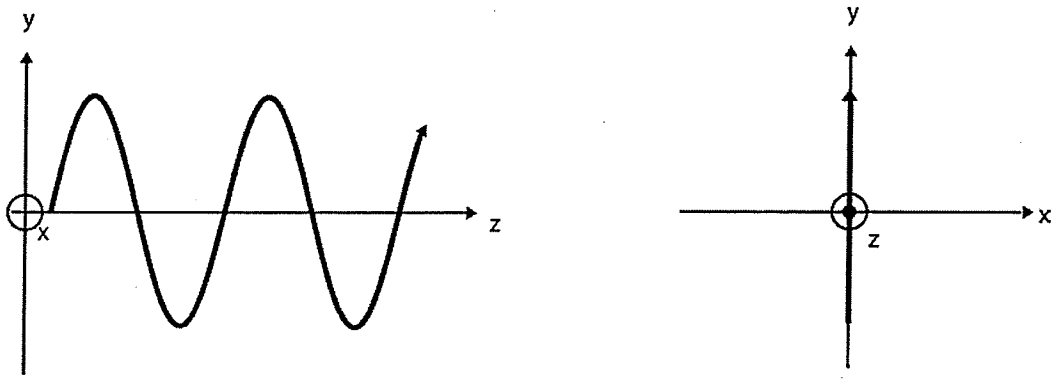

Figure 2-3: A linearly polarized wave propagating along the z-axis.

The following discussion is based largely upon material in Lang (1980). In general, polarized light will be elliptically polarized. Linear and circular polarization are special cases of elliptically polarized light. An arbitrary EM wave moving along the z-axis with frequency ω, can be expressed as the sum of two orthogonal components,

$$\mathbf{E} = \mathbf{i}E_x + \mathbf{j}E_y \ . \qquad (2\text{-}18)$$

Here **i** and **j** are unit vectors in the x and y directions respectively;

$$E_x = E_{0x}\cos\left(\mathbf{k}\cdot\mathbf{r} - \omega t - \delta_x\right) \qquad (2\text{-}19)$$

and $$E_y = E_{0y}\cos\left(\mathbf{k}\cdot\mathbf{r} - \omega t - \delta_y\right) \qquad (2\text{-}20)$$

where E_{0x} and E_{0y} are the amplitudes of the two waves, δ_x and δ_y are the phases, **k** is the wave vector and **r** is the radius vector.

If we define the phase difference between the two waves to be $\delta = \delta_y - \delta_x$, and take the vector combination of equations (2-19) and (2-20), we find a representation of the *observed* wave

$$\left(\frac{E_x}{E_{0x}}\right)^2 + \left(\frac{E_y}{E_{0y}}\right)^2 - \frac{2E_xE_y}{E_{0x}E_{0y}}\cos\delta = \sin^2\delta \qquad (2\text{-}21)$$

which is the equation of an ellipse.

The special cases of linear and circular polarization respectively are given by the conditions that: (a) the two waves are precisely in phase (i.e. $\delta_x = \delta_y \pm m\pi$ or $\delta = \pm m\pi$; m is an integer) and (b) where the waves differ in phase by exactly $\pi/2$ (i.e. $\delta_x = \pi/2 \pm \delta_y$ or $\delta = \pm\pi/2 + 2m\pi$) and $E_{0x} = E_{0y}$ (Figure 2-4). In case (a), Eq. (2-21) will reduce to the equation of a straight line, whereas in case (b), Eq. (2-21) reduces to that of a circle.

For arbitrary δ_x and δ_y one finds an ellipse traced as the wave propagates as viewed along the z-axis. Depending on the values of δ_x and δ_y, the ellipse may be traced in either a clockwise or a counter-clockwise direction. This directional property is termed the "handedness" of the polarization and the wave is said to exhibit right-handedness if it is moving in a counterclockwise direction ($\delta = \delta_y - \delta_x > 0$) and left-handedness if moving

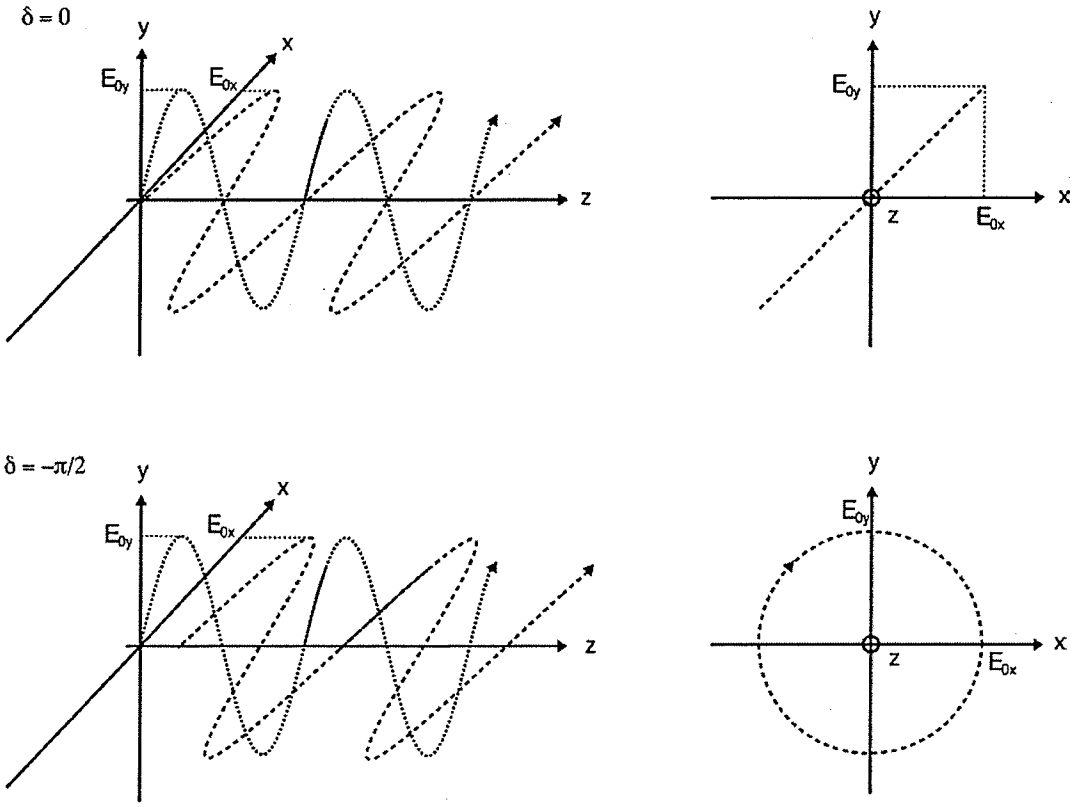

Figure 2-4: Special cases of linear ($\delta = 0$) and circular ($\delta = -\pi/2$) polarization.

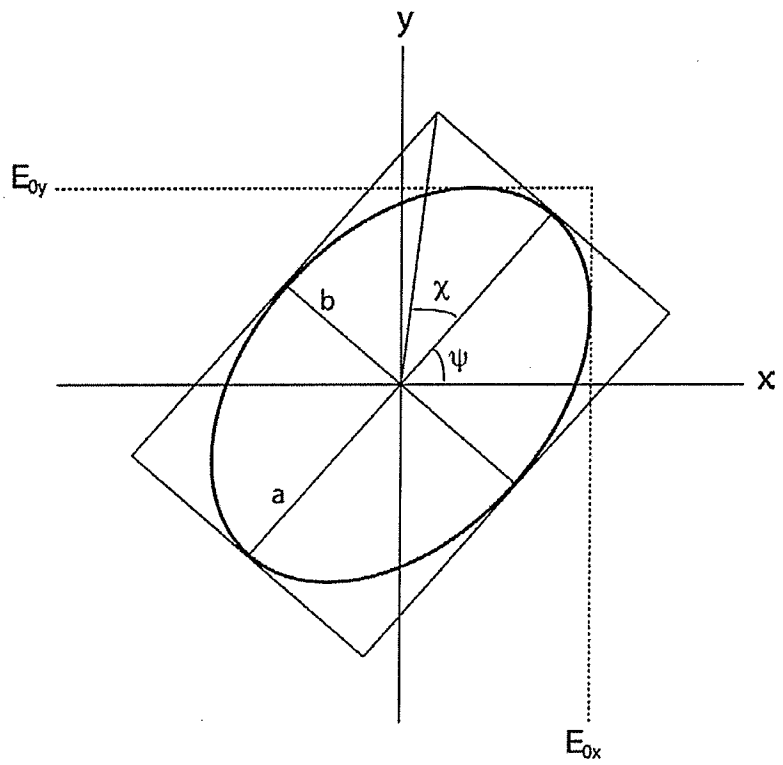

Figure 2-5: The polarization ellipse with semi-major axis, a, and semi-minor axis, b.

clockwise ($\delta = \delta_y - \delta_x < 0$). A right handed vector is defined to be negative (IEEE standard).

This ellipse is characterised by the length of its major and minor axes, 2a and 2b respectively, and by the angle, ψ, between its major axis and the x-axis. An alternative method of describing the ellipse is to use the angle defined by the semi-major and semi-minor axes, χ = arctan(b/a) along with ψ. (Figure 2-5)

2.2.1 Stokes parameters

In 1852, Sir George Stokes introduced one method of describing the state of polarization (the polarization ellipse) using four observable parameters: I, Q, U, and V that have collectively become known as the "Stokes" parameters. In this representation a polarized wave is characterised by a combination of its linearly and circularly polarized components. Other methods of describing the polarization state exist such as the Poincaré Sphere and the Jones vectors, but the Stokes parameters are often the representation adopted in radio astronomy and are what have been adopted here. The four parameters can be expressed equally in terms of the amplitudes and phases of the wave vectors (E_{0x}, E_{0y}, and δ) or in terms of the angular representation of the polarization ellipse (χ and ψ) as follows:

$$I = E_{0x}^2 + E_{0y}^2 \qquad (2\text{-}22)$$

$$Q = E_{0x}^2 - E_{0y}^2 = I\cos(2\chi)\cos(2\psi) \qquad (2\text{-}23)$$

$$U = 2E_{0x}E_{0y}\cos\delta = I\cos(2\chi)\sin(2\psi) \qquad (2\text{-}24)$$

$$V = 2E_{0x}E_{0y}\sin\delta = I\sin(2\chi). \qquad (2\text{-}25)$$

The Stokes I parameter measures the total power of the wave and is not an independent parameter since it can be expressed in terms of the other three

$$I^2 = Q^2 + U^2 + V^2. \qquad (2\text{-}26)$$

This is valid for a completely polarized wave. A more general statement,

$$I^2 \geq Q^2 + U^2 + V^2 \qquad (2\text{-}27)$$

can be made and is applicable to a partially polarized wave, where the total power is greater than the sum of the polarized components.

Stokes Q and Stokes U represent the two orthogonal components of the linearly polarized component of the wave and Stokes V represents the circularly polarized component. The polarization angle, or the tilt of the polarization ellipse, ψ, may be expressed in terms of the Q and U parameters as

$$\psi = \frac{1}{2}\arctan\left(\frac{\sin(2\psi)}{\cos(2\psi)}\right) = \frac{1}{2}\arctan\left(\frac{U}{Q}\right). \qquad (2\text{-}28)$$

Similarly, the intensity of the linearly polarized component of the wave, called polarized intensity (PI) may be determined by

$$PI = \sqrt{Q^2 + U^2}\,. \qquad (2\text{-}29)$$

2.2.2 Detected polarized emission

2.2.2.1 Polarized intensity

As described in section 2.1.1, synchrotron emission, which is emitted when fast moving electrons are spiraling in a magnetic field, is highly polarized. Such emission originates in the ambient Galactic medium but also in localized regions like supernova remnants. HII regions on the other hand contain a high density of thermal electrons and thus their emission is dominated by thermal radiation. They are not strong emitters of polarized radiation.

Since synchrotron radiation is highly polarized (up to 70% linearly polarized) and since the radiation at 1420 MHz is dominated by synchrotron emission both from supernova remnants and from the Galactic background one might expect that the observed polarized fraction, PI/I, would be close to 70%. This is not the case and in fact the detected polarized emission is much less than this, often only ~8% (Gaensler et al. 2001). Furthermore, observations often show an anti-correlation between total power and polarized intensity.

These observations can be explained, at least in part, by understanding that it is possible for the polarization vectors to add up in a way that cancels much of the detected polarized intensity. Understanding the various "depolarization mechanisms" requires first an understanding of polarization angle and Faraday rotation.

2.2.2.2 Polarization angle

Since polarized radiation is a vector quantity, the polarization angle is also as significant a quantity as polarized intensity. Polarized radiation is emitted with some intrinsic angle, ψ_0, but can undergo rotation along the line of sight in a process known as Faraday rotation (Figure 2-6). The amount of rotation is determined by a combination of electron density, n_e (cm^{-3}), the line of sight magnetic field component, $B_{//}$ (μG), the distance along the line of sight, dl (pc), and the wavelength of the radiation, λ (m) as

$$\Delta\psi = K\lambda^2 \int n_e B_{//} dl \qquad (2\text{-}30)$$

where

$$K = \frac{e^3}{2\pi m_e^2 c^4} = 0.812 \qquad (2\text{-}31)$$

(Bowers & Deeming 1984, Brown 2002). A quantity known as rotation measure, RM, is defined: $\Delta\psi = RM\,\lambda^2$. Thus,

$$RM = K \int n_e B_{//} dl \qquad (2\text{-}32)$$

(Bowers & Deeming 1984). Although HII regions are not strong emitters of polarized radiation, their high electron densities make them significant rotators. Thus HII regions may be "observed" in polarization images as the radiation which has lines of sight passing through the region will be rotated more than lines of sight adjacent to the HII region. Thus a region of smoothly varying polarization angle may be "scrambled" if there is an HII region that comes between the source of the smooth radiation and the observer.

In general the ambient Galactic background emission combined with regions of local enhancement means that polarized radiation is being emitted everywhere at some level.

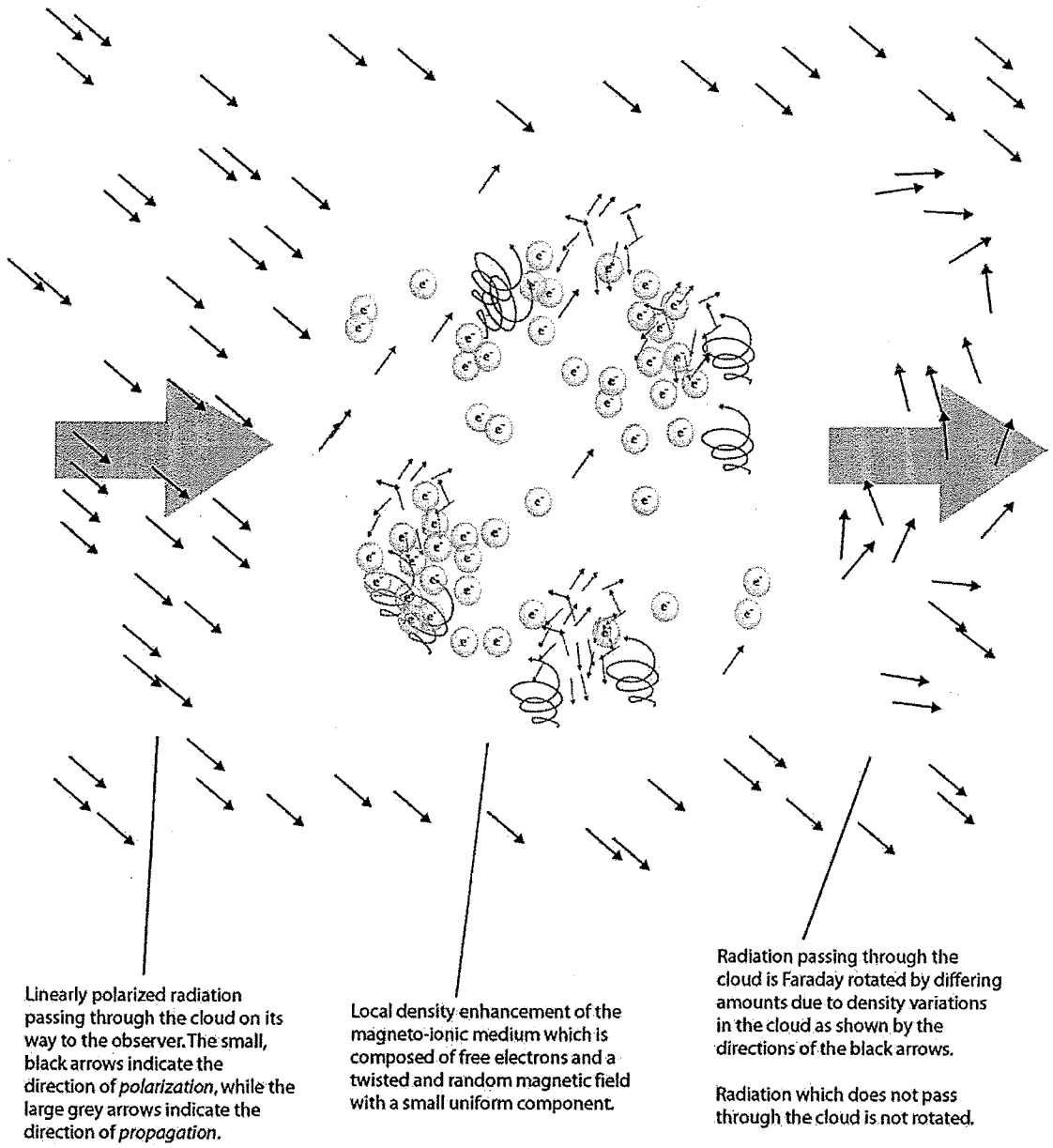

Figure 2-6: Illustration of Faraday rotation.

Regions that rotate the radiation overlap with the background emission, thus the rotating regions co-exist with the emitting regions, further complicating the problem.

2.2.3 Depolarization mechanisms

The cancellation of detected polarized radiation will occur in cases where the polarization angle varies by a significant amount between vectors contributing to a single measurement. The polarization angle may vary in this manner along the line of sight since one looks through a large path length in space, and also within the beam of the telescope. This leads to two separate mechanisms of depolarization: depth depolarization (Figure 2-7) and beam depolarization (Figure 2-8) respectively. A third depolarization mechanism, bandwidth depolarization becomes important if the rotation measure is very high for the wavelength of observation, and thus the angle may change by a large amount across the observing band (Gray et al. 1999).

2.2.4 Polarization horizon

The polarization horizon refers to a distance beyond which polarized emission becomes undetectable due to the effects of both depth depolarization and beam depolarization (Uyaniker et al. 2003). If there is enough scrambled, random emission along the adjacent lines of sight, the polarized emission of an extended and distant enough source will be canceled out. Figure 2-9 illustrates this effect. Knowing the distance to the polarization

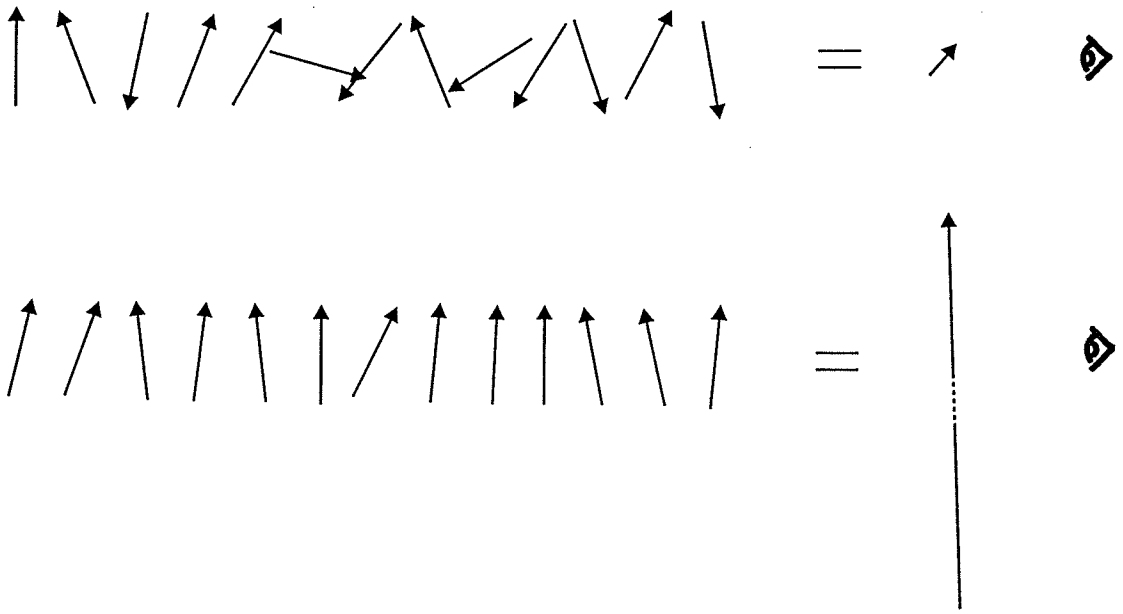

Figure 2-7: Depth depolarization along the line of sight (top). The scrambled vectors "cancel out" as seen by the observer. If the vectors are relatively unscrambled (bottom), the observer sees a higher polarized intensity as indicated by the long arrow.

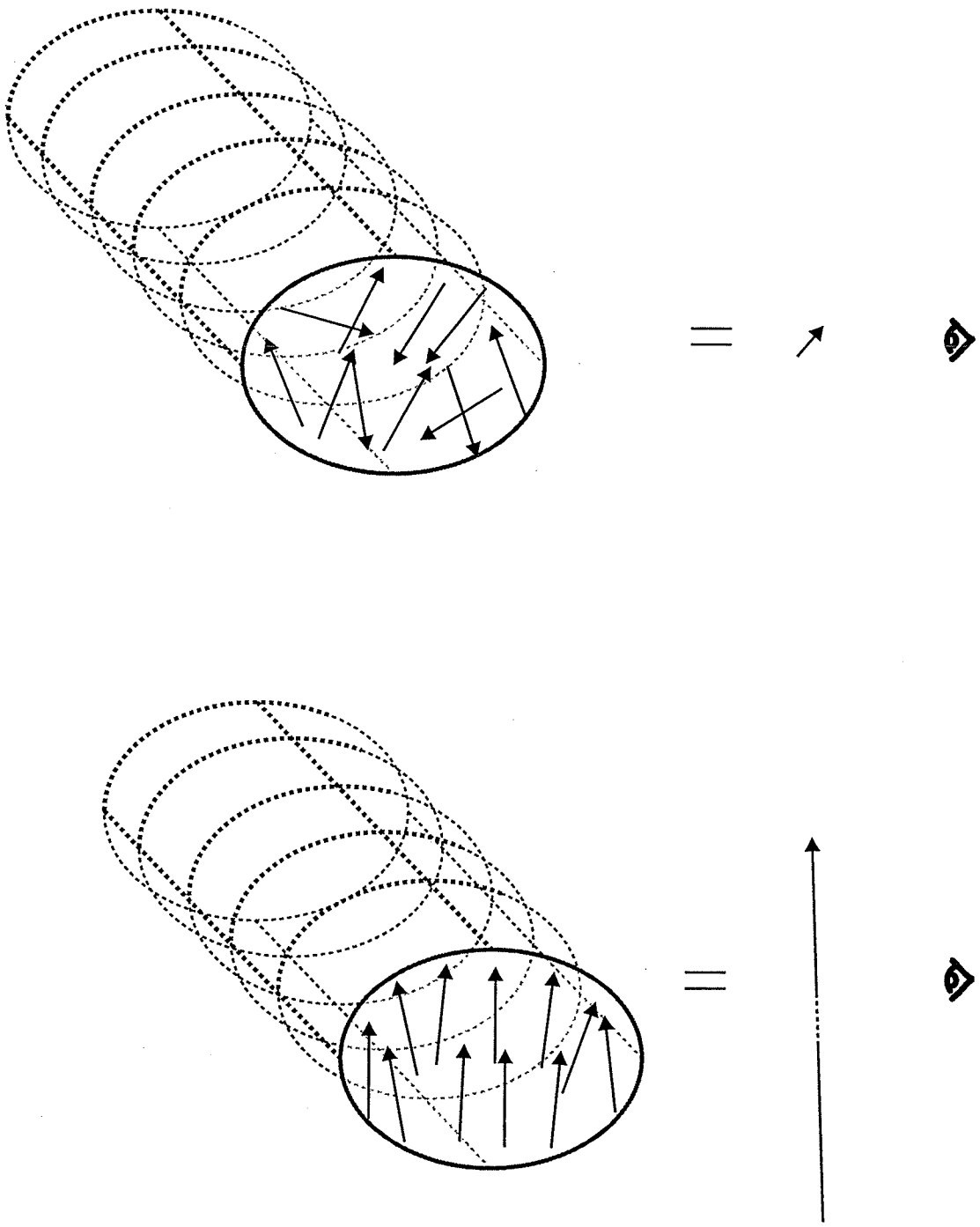

Figure 2-8: Depolarization within the beam of the telescope (beam depolarization). Adjacent infinitesimal lines of sight combine in the telescope's beam (as indicated by the elliptical cylinder in the illustration). Each of these lines of sight combine within the telescopes beam, so if the rotation varies over scales smaller than the beam size, depolarization may occur within.

(d_{ph}) can place limits on the distance to objects visible in Stokes I but not visible in Stokes Q or U.

The distance to the polarization horizon is dependent on the direction of the line of sight through the Galaxy (i.e. the Galactic longitude, l). For $l \sim 85°$, our line of sight is nearly along the direction of the Local arm (Figure 2-10) in which our Sun resides and must pass through all of the material distributed in this direction, increasing the amount of Faraday rotation. Furthermore the local magnetic field is found to be directed along $l \sim 83°$ (Heiles 1996) which increases the line of sight component of the magnetic field. Using Eq. (2-32) we see that this further increases the degree of Faraday rotation and decreases d_{ph}. However for $l \sim 135°$, which is in the direction of the W4 region, or the approximately opposite direction, $l \sim 330°$, the line of sight is more directly across the Local arm and most perpendicular to the corresponding magnetic field (Figure 2-10). Thus one would expect d_{ph} in these directions to be greater. Uyaniker et al. (2003) found d_{ph} ~2 kpc for $80° < l < 96°$ while Gaensler et al. (2001) suggest that observed polarized emission in the region $320° < l < 340°$ is occurring at a distance of 3.5 ± 1.0 kpc which implies $d_{ph} > 3.5 \pm 1.0$ kpc. Similarly, in the W4 region at $l \sim 135°$, there is observational evidence that the ionized gas of the HII region is Faraday rotating polarized emission which is along the same line of sight and must therefore originate behind W4 (Gray et al. 1999). The distance to W4 is believed to be ~2.3 kpc (Nomandeau 2000), thus implying d_{ph} to be greater than this distance.

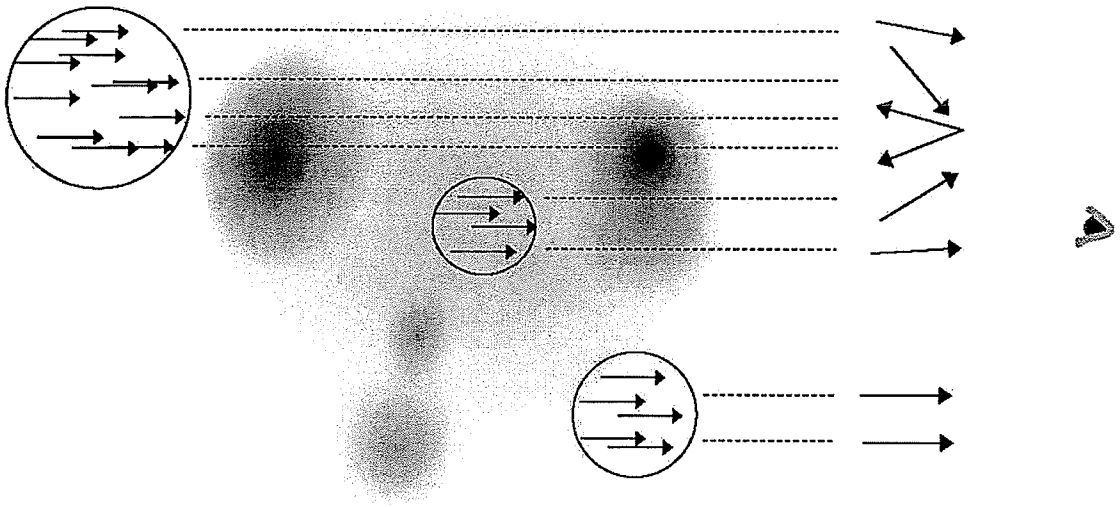

Figure 2-9: Illustration of the polarization horizon. The source at the far left is highly polarized but passes through so much ionized material that it is not detected. The middle source may be detected, but marginally. The source at the right will be detected because its polarized emission is occurring in front of the ionized clouds.

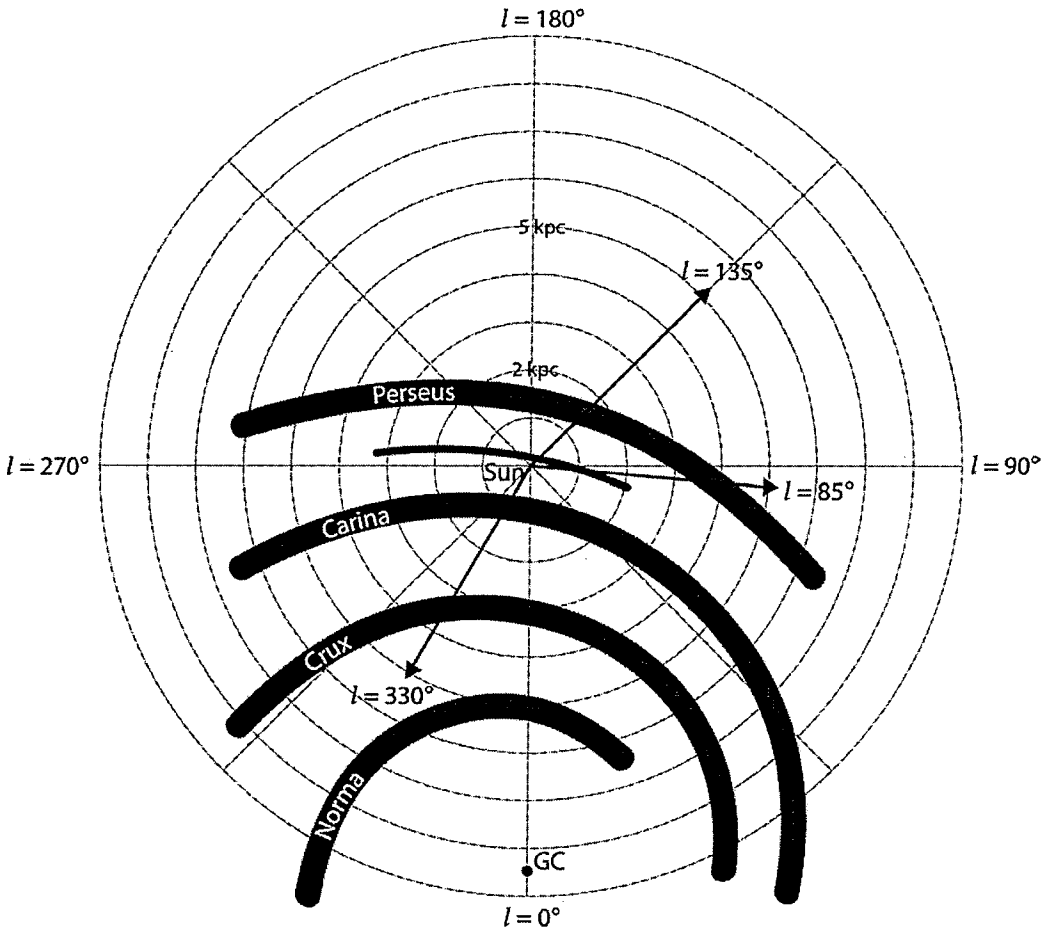

Figure 2-10: Schematic plan-view diagram of the Milky Way Galaxy (looking down on the Galactic plane) adopted from Han et al. (2002). Arrows illustrate lines of sight from the sun for $l \sim 85°$, $l \sim 135°$ and $l \sim 330°$ as discussed in the text. The concentric rings are spaced 1 kpc apart and the approximate Galactic centre is labeled "GC". There also exists a spiral arm beyond the Perseus arm which is referred to as the Outer arm (not illustrated).

2.2.5 Computing rotation measure

Recall from section 0 that the polarization angle is calculated using the Stokes Q and Stokes U images. Thus we can use Q and U and the following relationship (Eq. (2-28)) to determine ψ per pixel:

$$\psi = \frac{1}{2}\arctan\left(\frac{U}{Q}\right). \qquad (2\text{-}33)$$

This quantity is a combination of the intrinsic angle of the emitted radiation and Faraday rotation and may also be expressed by:

$$\psi = \psi_0 + RM \cdot \lambda^2. \qquad (2\text{-}34)$$

Here ψ_0 is the intrinsic angle, RM is the rotation measure and λ is the wavelength of observation. The form of equation (2-34) is that of a linear function of ψ vs λ^2 with a slope equal to RM. A requirement for computing RM is that one has observations of the polarization angle at several wavelengths or *bands* (see Figure 3-1 for an illustration of the bands used in the DRAO data).

In addition, one must use caution when using Eq. (2-34) to compute the RM since the polarization angle will "wrap" at a value of 180 degrees and thus the angle must be "unwrapped" before a value of RM may be obtained.

One method of unwrapping that is often used is that of a χ^2 fit. Here, the RM is first estimated by finding the slope between the polarization angles from the first two bands or wavelengths. Then multiples of π (180 degrees) are added or subtracted from the angles in following bands such that the value closest to the first fit is obtained. The procedure is iterated until χ^2 is minimized (Gaensler, et al. 2001). It is pointed out by Brown (2002) that this method is computationally intensive and an alternative method is suggested that is perhaps more appropriate for the DRAO data. Her method is less computationally intensive and is valid as long as the rotation between adjacent bands is less than π. This is a reasonable assumption to make for the DRAO data since given the total bandwidth of 35 MHz and the observation frequency of 1420MHz, a rotation measure of more than 1400 rad m^{-2} would be required to produce more than one wrap. Typical rotation measures from the Galaxy are on the order of $|100|$ rad m^{-2} (Brown, 2002).

We have chosen to use Brown's method of computing the polarization angles used to calculate RM and will outline the algorithm here.

First an angle, ϕ_n, in each band is obtained from:

$$\phi_n = \arctan\left(\frac{U_n}{Q_n}\right); \text{ where n is the band (A, B, C, and D) and } 0 < \phi_n < 2\pi. \quad (2\text{-}35)$$

(Note that $\phi = \psi/2$, and that ϕ is used to properly resolve the angle.)

Next the differences in angles from adjacent bands are computed:

$$\phi_{n+1,n} = \phi_{n+1} - \phi_n \quad (2\text{-}36)$$

If the difference between two adjacent angles is greater than π it indicates that the angle has wrapped. Unwrapped differences are achieved by the operation:

$$\phi'_{n+1,n} = \arctan\left(\frac{\sin(\phi_{n+1,n})}{\cos(\phi_{n+1,n})}\right) \quad (2\text{-}37)$$

This will leave the angle unaffected if in the range $0 < \psi_{n+1,\,n} < \pi$ (i.e. $0 < \phi_{n+1,\,n} < 2\pi$) and will appropriately wrap angles with values outside this range. Then the corrected differences are added back to the angles starting at band A:

$$\phi_A = \phi_A \quad (2\text{-}38)$$

$$\phi_B = \phi_A + \phi'_{B,A} \quad (2\text{-}39)$$

$$\phi_C = \phi_B + \phi'_{C,B} \qquad (2\text{-}40)$$

$$\phi_D = \phi_C + \phi'_{D,C} \qquad (2\text{-}41)$$

Finally, the polarization angles, ψ_n are calculated by dividing the result by 2, to put the resulting angle in the range $0 < \psi_n < \pi$:

$$\psi_A = \frac{\phi_A}{2} \qquad (2\text{-}42)$$

$$\psi_B = \frac{\phi_B}{2} \qquad (2\text{-}43)$$

$$\psi_C = \frac{\phi_C}{2} \qquad (2\text{-}44)$$

$$\psi_D = \frac{\phi_D}{2} \qquad (2\text{-}45)$$

Table 2-2 works through an example to illustrate how this method operates.

band	ϕ_n	$\phi_{n+1,n}$	$\phi'_{n+1,n}$	unwrapped ϕ_n	ψ_n
A	295			295	148
B	342	47	47	342	171
C	28	-314	46	388	194
D	67	39	39	427	214

Table 2-2: Example calculation of unwrapping algorithm

Once polarization angles in each band are determined, the rotation measure may be calculated by performing a standard weighted least squares fit (eg. Bevington & Robinson 1992) of $\psi(\lambda^2)$ vs λ^2:

$$RM = \frac{\sum \delta\psi_n^{-2} \sum \delta\psi_n^{-2} \lambda_n^2 \psi_n - \sum \delta\psi_n^{-2} \lambda_n^2 \sum \delta\psi_n^{-2} \psi_n}{\sum \delta\psi_n^{-2} \sum \delta\psi_n^{-2} \left(\lambda_n^2\right)^2 - \left(\sum \delta\psi_n^{-2} \lambda_n^2\right)^2} \qquad (2\text{-}46)$$

where the fit is weighted by the error in the polarization angle in each band, $\delta\psi_n^{-2}$.

The error in the polarization angle, $\delta\psi$ is given by

$$\delta\psi = \frac{\sigma_{QU}}{2PI}. \qquad (2\text{-}47)$$

Where σ_{QU} is the noise in the individual Stokes Q or Stokes U image and is given by

$$\sigma_{QU}^2 = \left(\sigma \sqrt{\frac{1}{w_{QU}}}\right)^2 + \left(\alpha_C I\right)^2 \qquad (2\text{-}48)$$

(Brown, 2002). Here σ is the rms noise at the centre of an individual field, w_{QU} is a

weighting factor, α_C is a scaling factor and I is the Stokes I intensity in Kelvin. In the case of the thesis data that has been convolved to 5', $\sigma = 0.01$ K. w_{QU} is a weighting factor, between 0 and 1 assigned to each pixel in the image when the data is mosaicked using the DRAO export software, *supertile* (see Figure 3-2). Pixels at the centre of a field have a weighting factor of 1. The second term accounts for error due to leakage from Stokes I into Stokes Q and U. The factor α_C was determined to be 0.003 (Brown 2002).

2.3 Understanding radio data

2.3.1 Fourier transform in imaging and Fourier filtering

The French mathematician, Jean Baptiste Joseph Fourier developed the theory that any periodic function, no matter the complexity, may be reconstructed by a sequence of sine functions of varying frequencies and amplitudes. This transform between frequency and spatial domains is formalized in the 1-D continuous integral:

$$F(u) = \int f(x)\exp(-i2\pi ux)dx. \qquad (2\text{-}49)$$

where x is the spatial coordinate and u is the coordinate in the frequency domain and $F(u)$ is the Fourier transform of $f(x)$ (Gonzalez & Woods 2002). If the transform is expanded to two dimensions and expressed in a discrete form, it becomes a very useful tool for image processing:

$$F(u,v)=\frac{1}{MN}\sum\sum f(x,y)\exp\left(-i2\pi\left(\frac{ux}{M}+\frac{vy}{N}\right)\right) \quad (2\text{-}50)$$

(Gonzalez & Woods 2002). Here, *F(u, v)* represents the Fourier transformed image with pixel coordinates (u, v). The value of each pixel in *F(u, v)* is given by a sum of every pixel in the spatial image multiplied by an exponential function. M and N are normalising constants representing the dimension of the image. The dimensions are typically restricted to power of two square images (i.e. 256x256, 1024x1024) in order to take advantage of the Fast Fourier Transform method that reduces computation time significantly.

In a Fourier Transform of an image, some information from every pixel of the spatial image is contained in any one pixel of the Fourier transform. This fact allows the entire spatial image to be reconstructed using only a single pixel from the Fourier domain. Of course, this would produce an uninteresting image since most of the information would be lost. However, useful and interesting images may be reconstructed in the spatial domain using only a subset of pixels from the Fourier domain. Such "Fourier filtering" allows one to select specific frequencies in the Fourier domain and then transform the image to produce a new spatial image containing only the selected frequencies. With a (*u, v*) coordinate system such that the origin is located in the centre of the image, low frequency information is located around the origin of the *F(u, v)* image and high frequency information is contained around the edges.

Fourier filtering is achieved by multiplying, pixel by pixel, the frequency image, *F(u, v)* by a filter transfer function, *H(u, v)*. The inverse Fourier transform is then applied to the resulting image, *G(u, v)* to produce a filtered spatial image, *g(x, y)*.

To reduce high frequencies in an image, one would apply a filter that only retains low frequency information, called a lowpass filter, to the original image. A useful lowpass filter transfer function is the Gaussian lowpass filter. The Gaussian lowpass filter is characterised by a half width at half maximum value, D0.

The Stokes Q (Figure 2-11a) and U linear polarization images have been Fourier filtered using a Gaussian lowpass filter with a D0 = 64 pixels. The Fourier transform of the Stokes Q image (Figure 2-11b) shows a distinct circular region of radius ≈ 280 pixels at low frequencies with higher values than the surrounding high frequency information. This circular region is a product of the fact that the image was produced using an interferometer that is sensitive to a specific range of frequencies that in turn are dependent on the spacings (baselines) of the dishes in the array. The relationship between the length of the baseline, ΔL [λ] and the pixel resolution, $\Delta\theta$ [rad] is:

$$\Delta\theta = \frac{1}{N \cdot \Delta L} \qquad (2\text{-}51)$$

where N is the dimension of the image (Gonzalez & Woods 2002). For Figure 2-11a, $\Delta\theta$ = 20" = 10^{-4} rad and N = 1024, thus $\Delta L \approx 10\lambda$. Thus for λ = 0.211 m, ΔL = 10 * 0.211 m

= 2.1 m (per pixel). And since the circular region has a radius ≈ 280 pixels, ΔL for this feature is

$$\Delta L = 280 * 2.1 \text{ m} = 588 \text{ m} \qquad (2\text{-}52)$$

which is approximately equivalent to 604 m, the longest baseline of the telescope (see section 3.1 for a description of the telescope and section 2.3.2 for a description of interferometry). It is important to note that $\Delta\theta$ is not the true image resolution, but rather the sampling resolution. Image resolution is given by the FWHM of the beam of the telescope and is between 2 - 3 times the pixel resolution in the case of the 21 cm (1420 MHz) images.

D0 was chosen by inspection such that much of this low frequency information would be preserved – i.e. take D0 ≈ σ = 64, 4σ = 256 ≈ 280. Figure 2-11c shows the new filtered image in the Fourier domain, G(u, v) and Figure 2-11d shows the inverse transform G(u, v); the new spatial Fourier filtered image, g(x, y). The resulting image is much smoother than the original, having had much of the high frequency information removed. Choosing a larger value for D0 would retain more of the high frequency information, producing an image with less smoothing.

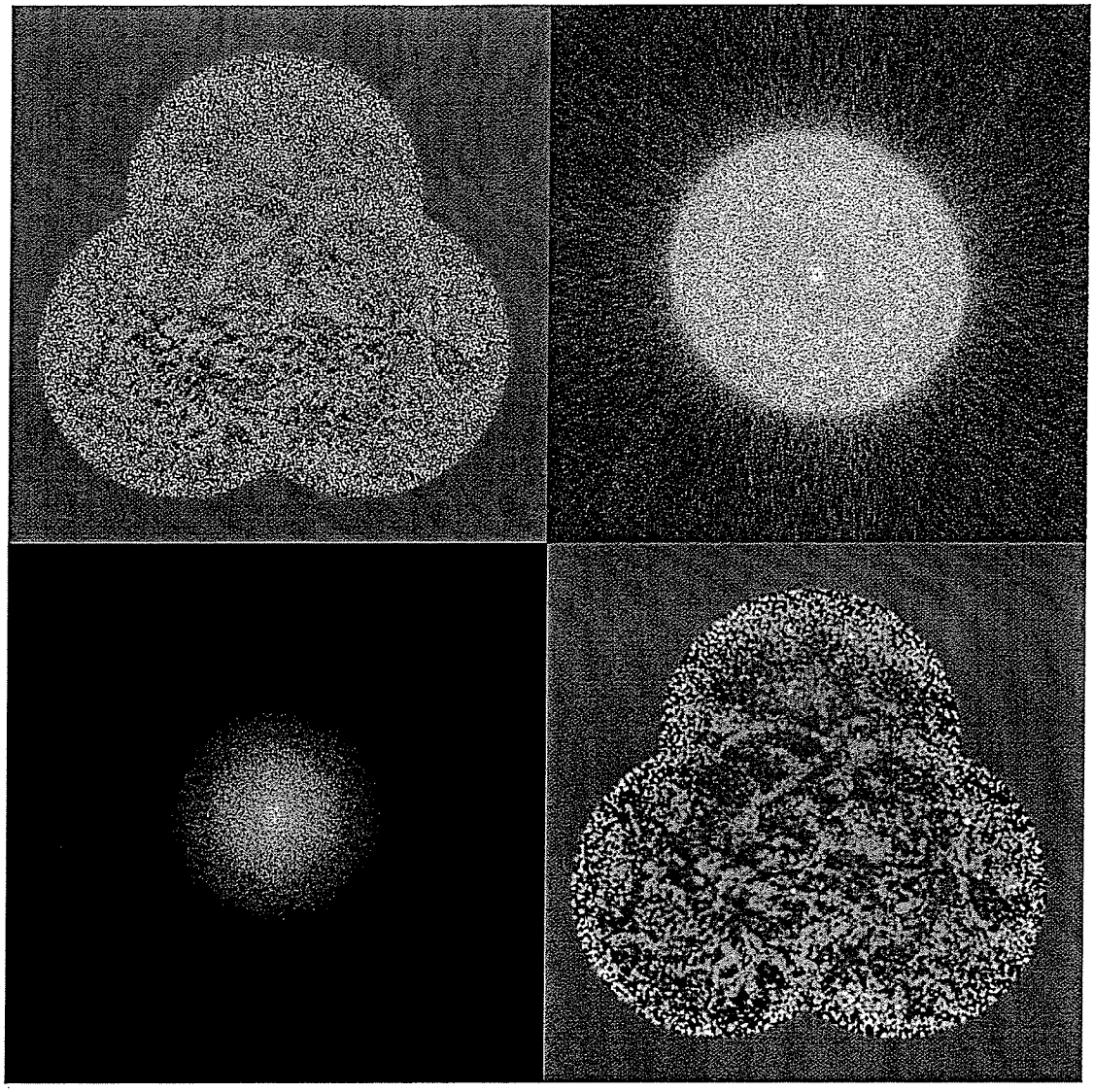

Figure 2-11a-d: a) (top left) Full resolution Stokes Q image.

b) (top right) Fourier transform of (a).

c) (bottom left) Gaussian filter function with D0 = 64, multiplied by (b).

d) (bottom right) Inverse Fourier transform of (c).

2.3.1.1 Convolution theorem

The convolution theorem describes the relationship between the frequency and spatial domains and states that a multiplication in one domain is equivalent to a convolution in the other domain. Stated mathematically,

$$f(x,y) * h(x,y) \Leftrightarrow F(u,v)H(u,v) \qquad (2\text{-}53)$$

(Gonzalez & Woods 2002) where *F(u, v)* and *H(u, v)* are the Fourier transforms of *f(x, y)* and *h(x, y)* respectively.

This means that instead of multiplying the Fourier transform of the image with a Gaussian filter function, one may perform a convolution on the spatial image with the Fourier transform of the Gaussian filter function. And since the Fourier transform of a Gaussian function is also a Gaussian function, the removal of high frequency information may be achieved by convolving the spatial image with a Gaussian filter.

In this thesis, when it is desired to reduce the data to a lower resolution to remove some of the high spatial frequencies, which include the noise, and thus improve the signal to noise ratio, this is achieved by spatial convolution using the DRAO export software *mosconv* (see Appendix 1).

2.3.2 *Radio interferometry*

As one increases the wavelength of observation towards the radio regime it becomes increasingly difficult to achieve a high resolution with a single dish telescope. The diffraction (resolution) limit of a telescope, θ (radians), is given by $\theta = \lambda/d$, where λ is the wavelength of observation in meters and d is the diameter of the telescope also in meters. In the case of radio astronomy, the resolution is measured by the full width at half maximum (FWHM) of the main lobe of the telescope's beam pattern.

For example, to achieve a resolution of $\theta = 1'$ at $\lambda = 0.01$ m, we find $d = 42$ m. While single dishes on the order of this size exist such as the 100 m Effelsberg Telescope, if one wishes to observe at a longer wavelength, say $\lambda = 0.211$ m, and obtain similar resolution, the diameter of the telescope must increase to 885 m. It is a very difficult task to construct a single dish with a diameter of 885 m (especially a steerable dish), however equivalent resolution may be obtained by observing simultaneously with two small dishes spaced 885 m apart – i.e. an interferometer. The difficulty with this approach is a) sensitivity is much less than with a single dish since the collecting area is greatly reduced and b) these two dishes are only sensitive to spatial scales equivalent to the resolution. These problems can be overcome at least in part by using more than two dishes, i.e. an array of antennas spaced at regular intervals. The distance between each pair of antennas in the array is often referred to as a *baseline*. As determined by its length, each baseline contributes information at a particular spatial scale.

A single observation with an interferometer consists of the individual antennas tracking the source over the course of a day (typically 12 hours). Parallel wavefronts approach the earth perpendicular to the azimuth of the source. As the source moves across the sky, the angle between the direction to the source and the line connecting two antennas changes and consequently so too does the arrival time of a particular wavefront change. The time lag between the detections of a single wavefront at each antenna depends on the wavelength of observation, λ (i.e. the space between the wavefronts), the angle between the array and the source, θ, and the length of the baseline, L (Figure 2-12).

In general the antennas will not simultaneously detect signal from the same wavefront (the case of t2 in Figure 2-12 is the exception) and instead they will detect differing points on the incoming wave. In the case where both antennas detect a wave peak, that is when $L \sin\theta$ is equal to an integer number of wavelengths, n, one finds the signals add and one observes constructive interference. In the case where one antenna detects a wave peak while the other detects a wave trough, that is $L \sin\theta$ is equal to $n+1/2$ wavelengths, the signals will cancel and one observes destructive interference.

As the earth rotates on its axis the combined signal between two antennas (i.e. the interference pattern) will change in amplitude. And as Figure 2-12 shows, the angle also changes; in an interval of 12 hours the baseline will have rotated through all possible angles with respect to the source. If the antennas are oriented in a line running from east to west, then as viewed from the source, the baseline will in general trace out an ellipse, with the eccentricity of the ellipse dependent on the declination of the source. If the

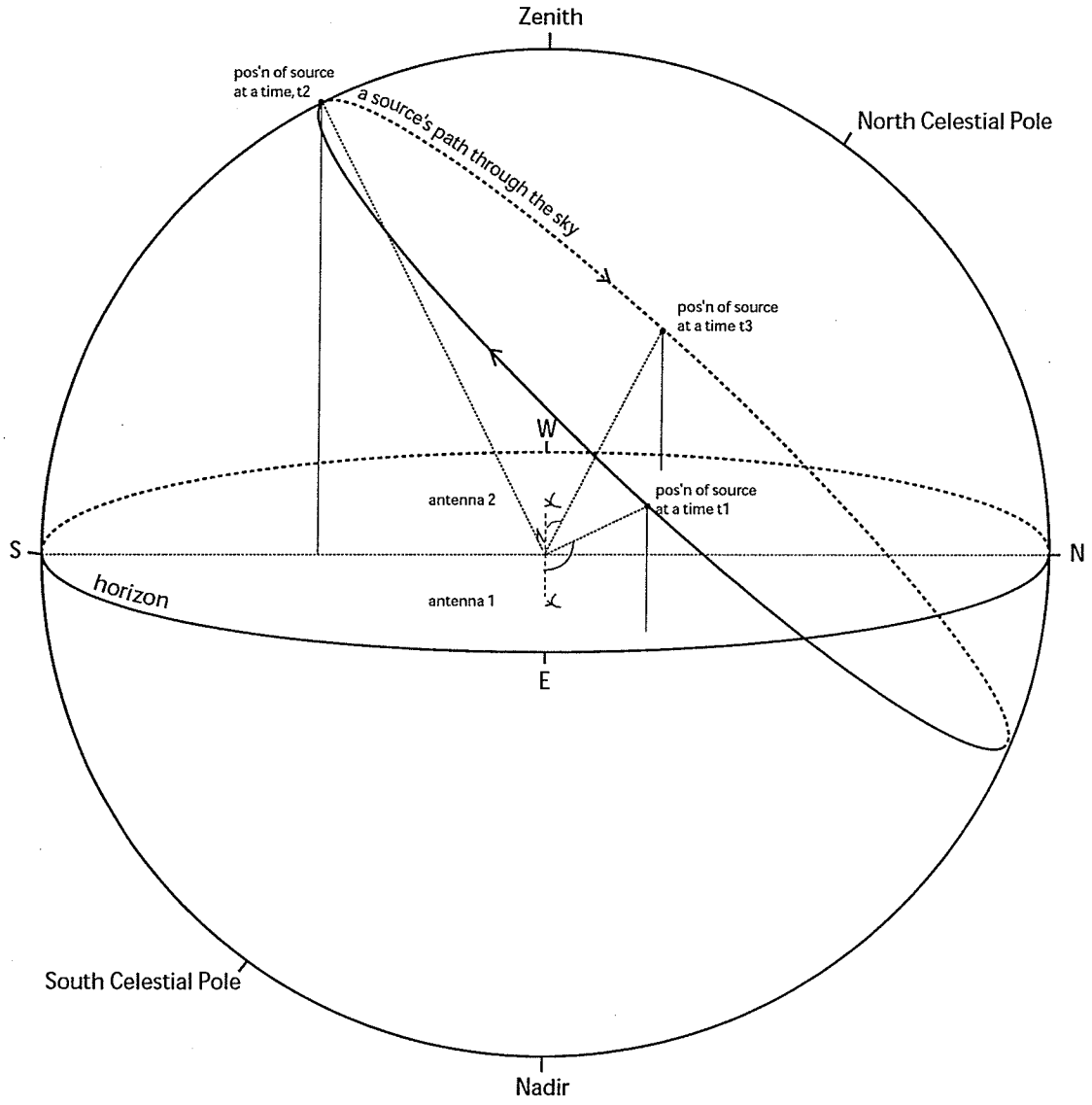

Figure 2-12: The angle between the source and a pair of antennas changes as the source moves across the sky. At t1, antenna 1 detects signal from a particular wavefront before antenna 2. At t2, the source is crossing the celestial meridian and so the antennas, being oriented along an east-west baseline, detect signal from the source simultaneously. At t3, antenna 2 detects signal from a particular wavefront before antenna 1.

source is at a celestial pole, the baseline will trace out a circle with a radius proportional to the length of the baseline. If the source is on the celestial equator then the baseline will trace out a line. This is illustrated in Figure 2-13.

Each spacing between two telescopes in the array contributes information in the form of traced ellipses of different sizes that are specified using u-v coordinates, i.e. in the frequency domain of the final image. The telescope spacing also determines which spatial resolutions are sampled in the u-v plane. Recall the resolution limit of a telescope is

$$\Delta\theta = \frac{\lambda}{L} \qquad (2\text{-}54)$$

where $\Delta\theta$ is the resolution, λ is the wavelength of observation and L is the length of the telescope baseline (previously this equation was expressed with the telescope diameter, d, in place of L). For example, the maximum spacing of the DRAO telescope is 604.29 m (see section 3.1) which means that at $\lambda = 0.211$ m, the telescope can theoretically detect a maximum resolution of $\Delta\theta = 3.5\times10^{-4}$ rad or ~1.2'. The minimum spacing of the telescope is 12.86 m which means that it can detect a maximum spatial scale of $\Delta\theta = 0.016$ rad or ~56'. The implication of this is that the telescope is insensitive to diffuse emission that varies on scales larger than ~56'. Thus the addition of single dish telescope data is required to recover this lost emission since single dish telescopes detect all of the flux from all spatial scales. (see Burke & Graham-Smith 1997 or Steinberg & Lequeux 1963 for further details on radio interferometry)

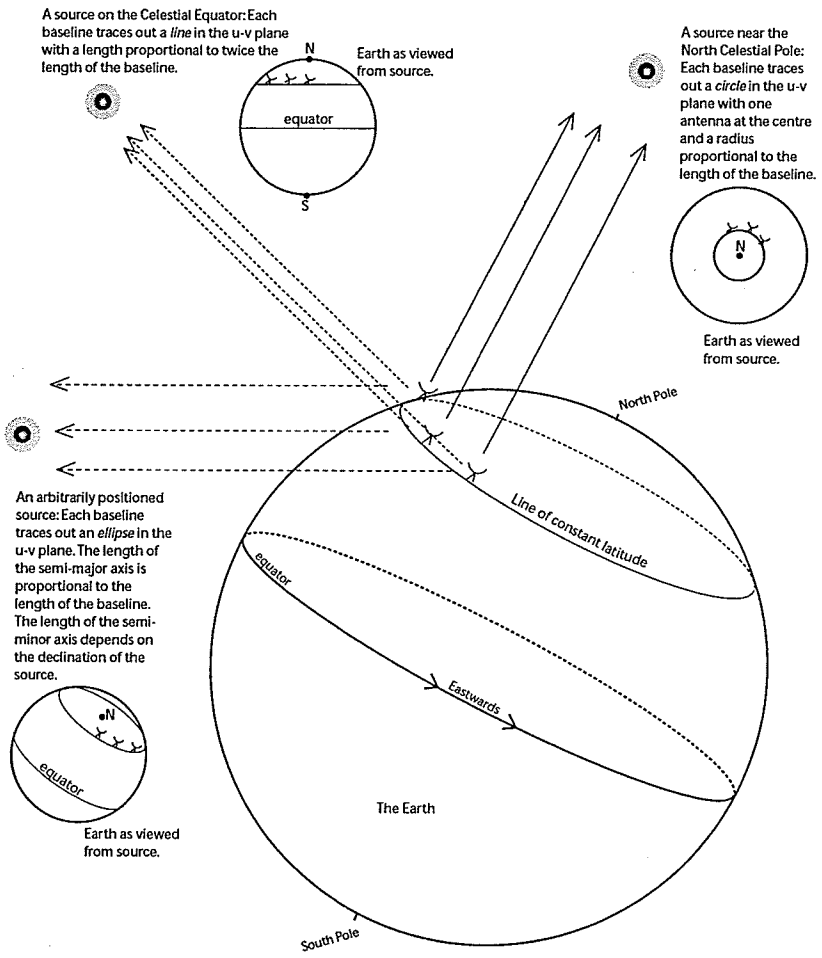

Figure 2-13: An east-west oriented array on the earth in general traces out an ellipse as the earth rotates and as viewed from a source. The special cases of a circle and a line can be observed if the source is at a pole or on the celestial equator, respectively.

3: Data and Results

This chapter describes the data used in this thesis. Section 3.1 describes necessary details of the telescope and in section 3.2 the manipulation of the original raw data is explained. The images are presented in section 3.3 in the original greyscale form. Also presented in section 3.3 are some images that have been processed by convolution. In section 3.4, some of the data are combined into false colour images that serve to enhance morphological features discussed in this study and allow easier comparisons between the various datasets. Mean intensity measurements for 56 10'×10' boxes are given in section 3.5.

3.1 The Dominion Radio Astrophysical Observatory (DRAO) Synthesis Telescope

Landecker et al. (2000) provides a complete description of the Dominion Radio Astrophysical Observatory (DRAO) synthesis telescope located in Penticton, British Columbia, Canada. The telescope is an east-west array of seven dishes with diameters ~9 m. Of these seven, four are fixed and three are movable allowing sampling of baselines from 12.86 m to 604.29 m in steps of 4.29 m. When observing at $\lambda = 0.211$ m, this works out to be equivalent to sampling between 61 λ and 2864 λ at intervals of 20 λ. This provides full u-v plane coverage for spatial frequencies between about 1' and 56'

(see section 2.3.2). In order to sample all baselines and achieve a single full synthesis observation, 12 individual observations of 12 hours each are required.

3.2 Observations

The DRAO synthesis telescope has been recently used to complete Phase I of the Canadian Galactic Plane Survey (CGPS) (Taylor et al. 2003). The CGPS is a relatively high resolution (~1') data set with a sensitivity of 0.28 mJy/beam (Landecker et al. 2000) and covering 73.1° of longitude from $147.3° > l > 74.2°$ along the Galactic plane of the Milky Way. The latitude extent covers $-3.6° < b < +5.6°$.

The data consists of several complementary components: spectral line of atomic hydrogen at 1420MHz, total intensity continuum emission at 1420MHz and 408MHz, and Stokes parameters Q and U which combined represent linear polarized intensity (see section 2.2, Lang 1980; Brown 2002) at 1420MHz. These are summarized in Table 3-1. Combining high resolution and sensitivity with wide coverage of the Galactic plane, the CGPS is one of the best data sets available for investigation of detailed gas structure in our Galaxy. The radio continuum and polarization data will be used in this investigation. The high latitude fields of M. Normandeau (private communication), which have been observed on the same grid as the CGPS but which are not officially part of the survey, play an essential role in our analysis.

The radio continuum fields at 1420 MHz are observed in four discrete 7.5 MHz bands, labeled A, B, C, and D and centred at $\nu \pm 6.25$ MHz and $\nu \pm 13.75$ MHz from the HI spectral line frequency of $\nu = 1420.406$ MHz (Figure 3-1). This leaves a 5 MHz gap at the central frequency, which is sufficient to avoid contamination from the HI spectral line. The central 1 MHz of the gap is used for the spectral line observations. The 7.5 MHz bands are combined into a single 1420 MHz radio continuum image.

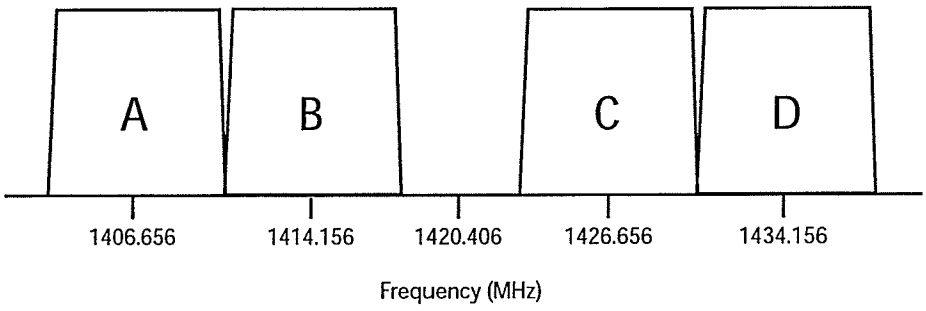

Figure 3-1: Illustration of the observing bands used in the 1420 MHz observations at DRAO (adapted from Brown 2002).

At 1420 MHz the field of view of the synthesis telescope has a full width at half maximum (FWHM) of 107'.2. At 408 MHz, the FWHM of the field of view is 332'.1. The survey region has been observed on a regular hexagonal grid with 112' between field centres. Mosaics of images are created using *supertile* which is part of the DRAO export package (see Appendix 1). The mosaics produced for this thesis consist of 11 CGPS fields plus an additional 3 fields obtained by M. Normandeau (private communication) observed at latitudes greater than b = +5.6°. Figure 3-2 shows the arrangement and

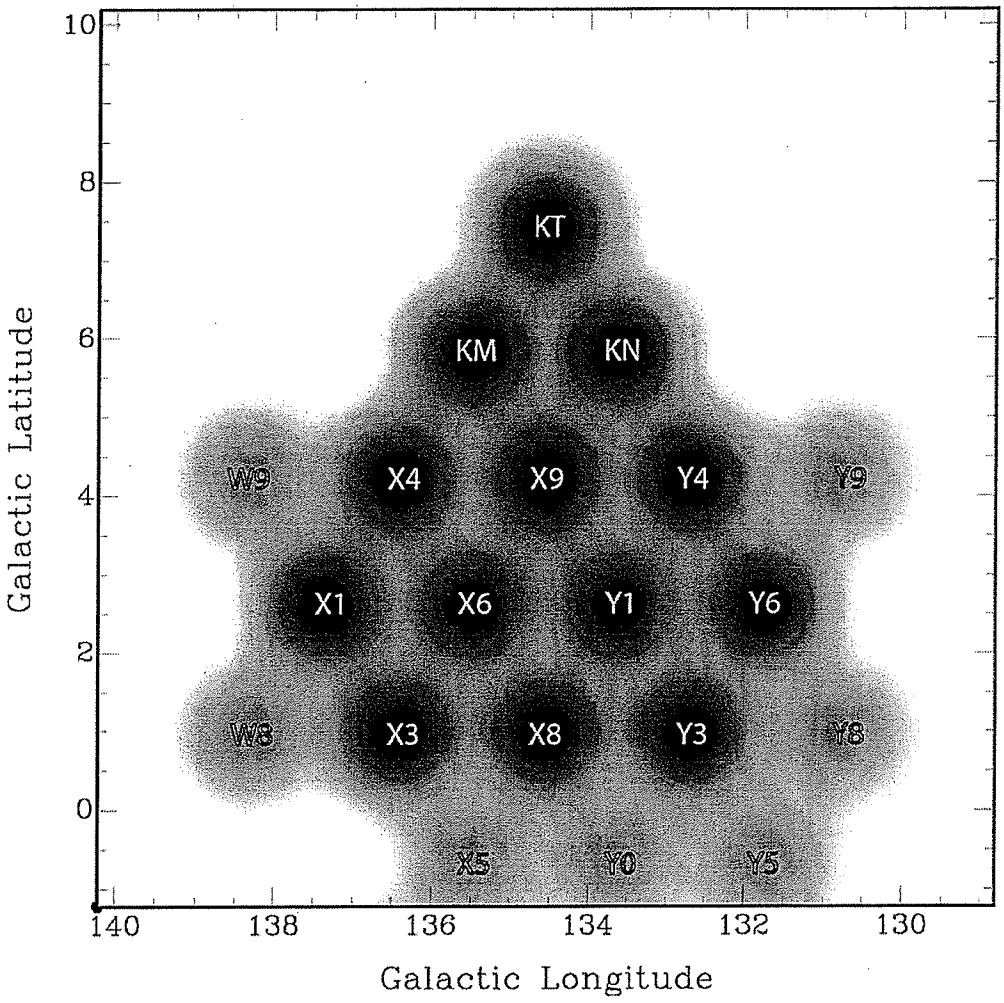

Figure 3-2: Arrangement and Galactic coordinates of the images used to create the mosaics used in this thesis. The light grey fields W8, W9, X5, Y0, Y5, Y8, and Y9 are fields included only in the polarization mosaics while the remaining central fields are included for all of the CGPS mosaics. The Grey scale for these central fields represents the weights applied to each pixel when the fields are combined into a mosaic. Black represents a weight of 1 (the centre of the individual fields) and white represents a weight of 0. The latitude and longitude scales shown have units of degrees.

Galactic coordinates of these fields. The individual fields are named according to the convention established at DRAO. Those labeled KM, KN, and KT are the additional, non-CGPS fields.

Taylor et al. (2003) indicate that there is an uncertainty in the absolute scale of the 408 MHz data of up to ~15% due to uncertain calibration data. The internal precision of the data is unaffected by this error.

The CGPS survey has motivated 2 other radio surveys acquiring similar data sets which when combined will offer a nearly complete survey of the entire Galactic plane ($\Delta\lambda$ = ~270°, $\Delta b = \pm 3°$). These are the Southern GPS (SGPS) that uses the Australia Telescope Compact Array and the VGPS which uses the Very Large Array in Socorro, NM. Additionally, the CGPS was extended to cover more longitude. Collectively these data sets have become known as the International Galactic Plane Survey (IGPS).

Additionally, there exist other public data sets that have been regridded to the same resolution as the IGPS and which are useful in this thesis. These include infrared data from the Infrared Astronomical Satellite (IRAS) and molecular line data from the Five Colleges Radio Astronomy Observatory (FCRAO). A summary of all data sources is presented in Table 3-1.

Frequency (Wavelength)	Bandwidth	Source	Spatial resolution ('(EW)x'(NS))	ISM Component Identified in Data	Reference
1420 MHz (21 cm)	Spectral line 1 MHz with 256 channels	DRAO/ CGPS	1.00 x 1.14	Atomic hydrogen spectral line	NTD97*
1420 MHz (21 cm)	30 MHz Continuum	DRAO/ CGPS	1.00 x 1.14	Ionized gas, relativistic plasma	NTD97*
1420 MHz (21 cm)	30 MHz Linear polarization, Stokes Q & U	DRAO/ CGPS	1.00 x 1.14	Magnetic fields	NTD97*
408 MHz (74 cm)	4 MHz Continuum	DRAO/ CGPS	3.5 x 4.0	Ionized gas, relativistic plasma	NTD97*
115 GHz (2.6 mm)	256 channels x 10 kHz per channel	FCRAO	~0.8 x ~0.8	CO spectral line (J = 1-0 transition)	Heyer 1995
3 & 5 THz (100 & 60 microns)		IRAS (hi-res) from Caltech	~2 x ~2	dust grains	Kerton & Martin 2001
12 & 25 THz (25 & 12 microns)		IRAS (hi-res) from CITA**	~2 x ~2	dust grains, PAHs (polycyclic aromatic hydrocarbon)	Kerton & Martin 2001
* Normandeau, Taylor & Dewdney 1997 **Canadian Institute for Astrophysics					

Table 3-1: Summary of data sources available for this thesis project as part of the CGPS (IGPS). For some of the analysis the 1420 MHz data has been convolved with a Gaussian beam matching that of the 408 MHz data. In other cases the 1420 MHz data has been convolved to 5' and 10' to improve the signal-to-noise ratio. CGPS data is available at the CADC website (http://cadcwww.dao.nrc.ca/).

3.2.1 Addition of single dish telescope data

Since the minimum spacing of the telescopes is 12.86 m, the very large scale structures are not present. To regain this missing information it is necessary to add short spacing data (also known as zero-spacings) from larger single dish telescopes. Single dish telescopes detect all flux at all spatial scales, but only the flux due to the missing spatial scales are added into the final images.

At 1420 MHz, single dish data is obtained from the 100 m Effelsberg telescope (Taylor et al. 2003, Reich et al. 1990, 1997) with a resolution of 9'. This survey does not have adequate latitude coverage and thus fields above $b \sim 4°$ instead use single dish data from the Stockert 25-meter northern sky survey (Taylor et al. 2003, Reich 1982, Reich & Reich 1986) which has a resolution of 35'. The Effelseberg data was absolutely calibrated using the Stockert survey data which ensures consistency amongst the contribution to our data from the short spacing data. Short spacing information is only added to the 1420 MHz continuum maps (Stokes I) and not to the Stokes Q or Stokes U polarization maps. At 408 MHz, short spacings are obtained from the all sky map of Haslam et al. (1982) with a resolution of 51' (Taylor et al. 2003).

3.2.2 Processing

The processing of all CGPS data fields (i.e. all fields in Figure 3-2 with the exception of the higher latitude fields, KM, KN, and KT) and the addition of short spacing data in all fields were carried out by members of the CGPS data processing team (Taylor et al. 2003). Processing of the fields KM, KN, and KT and mosaicking of fields were carried out by the author with the assistance of Roland Kothes. Short spacing information was added to these data by Dave Del Rizzo. See appendix 1 for details on image processing.

The CLEAN (Högbom 1974) algorithm was used in processing the fields. The

assumption of the algorithm is that the sky may be represented by a sum of point sources. In an iterative procedure, CLEAN uses a model of the telescope's "dirty beam" to subtract off each point source in the image. Each source is then convolved with a Gaussian beam and then added to the residual image to make the final "CLEAN map".

3.2.3 Sensitivity

The rms sensitivity of the telescope in the 1420MHz continuum data is 0.28 mJy/beam (Landecker et al. 2000) which is equivalent to 0.05 K for a 1' beam. Much of the data has been convolved to lower resolution to improve the signal to noise ratio. The noise is proportional to the beam area so, since resolution is proportional to the square root of the area, convolving the data from 1' to 5' will reduce the noise by ~5 times.

3.3 Greyscale image catalogue

The data discussed in this thesis is presented in Figure 3-3 to Figure 3-12. Details about each image are included in the figure captions.

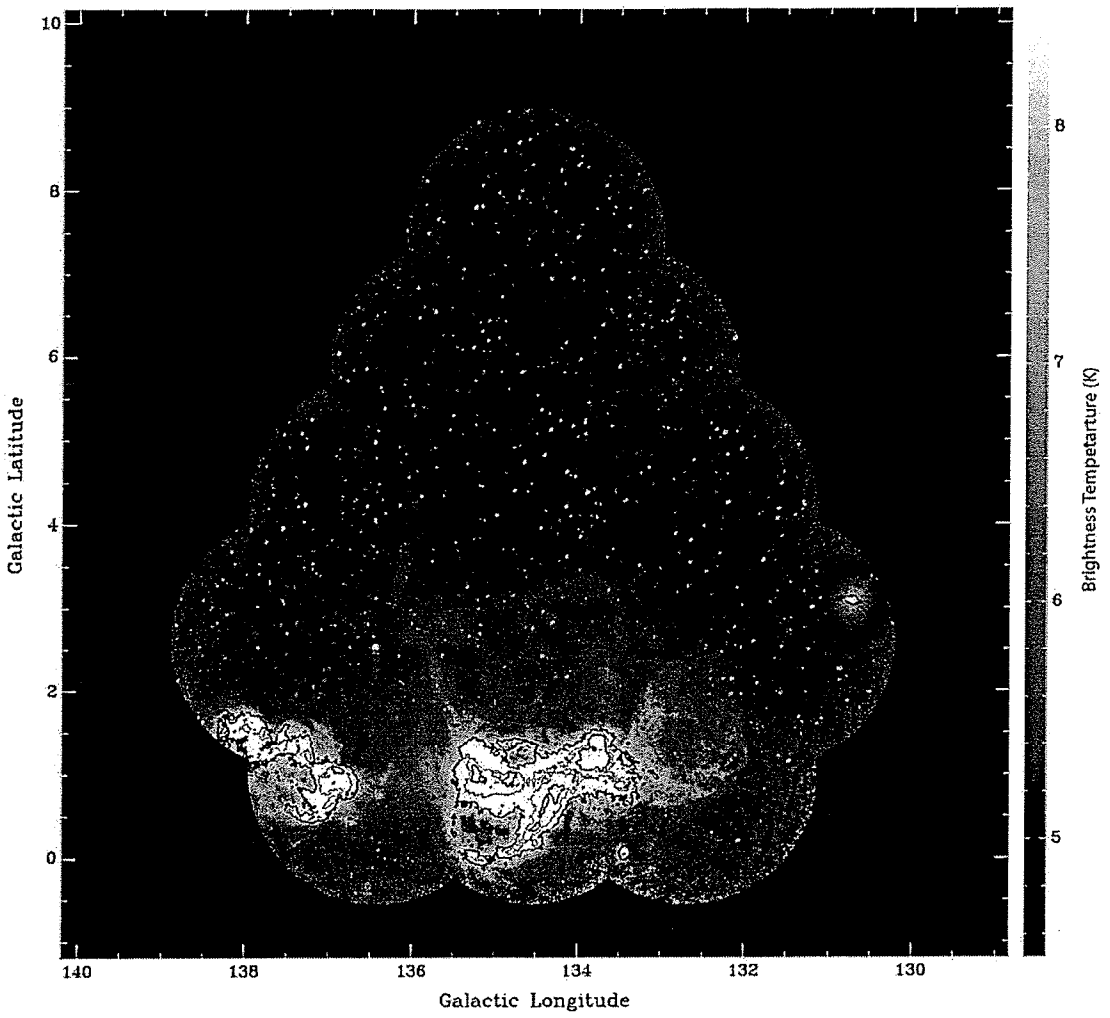

Figure 3-3: 1420 MHz (21 cm) Stokes I continuum image at full resolution linearly scaled to show the brighter regions with contours defining the clipped regions. Grey scale is brightness temperature in Kelvin ranging from 4.5 K (black) to 8.5 K (white) and is shown at right. Contours in black are for 16K and 8.5 K. The grey contour is at 11 K. The latitude and longitude scales shown have units of degrees.

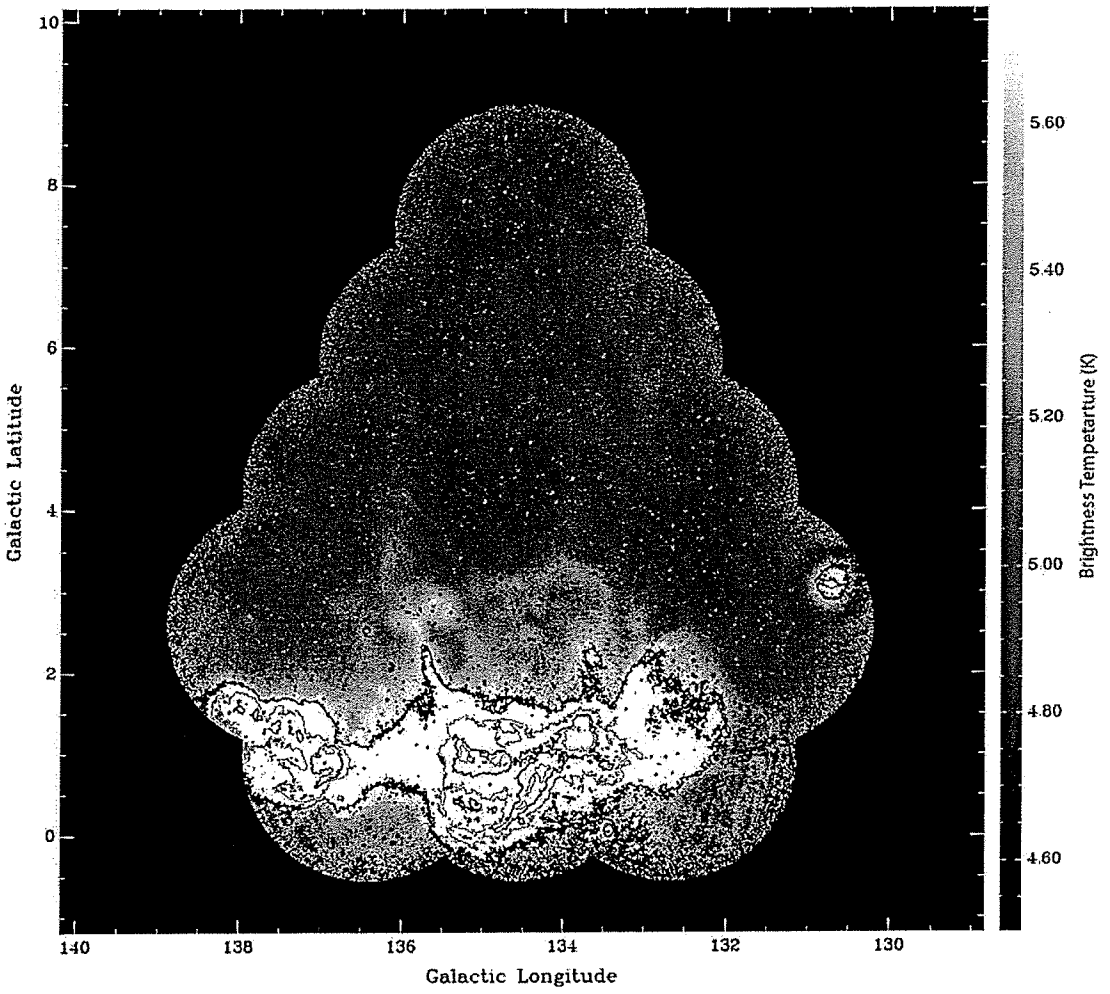

Figure 3-4: 1420 MHz (21 cm) Stokes I continuum image at full resolution linearly scaled to show the fainter emission with contours defining the clipped region. Grey scale, shown at right, is brightness temperature which has been linearly stretched between 4.75 K (black) and 5.75 K (white) in order to emphasize the faint high latitude emission. Contours in grey are at 16 K and 8 K. Black contours shown are 11 K and 6 K. Note the distinctive, elliptically shaped low emission region above W4 and centred at l = ~135°, b = ~4° (see discussion, section 5.1). The "walls" of the region can be seen extending vertically upwards at l = ~136° and at l = ~133.5°. The latitude and longitude scales shown have units of degrees.

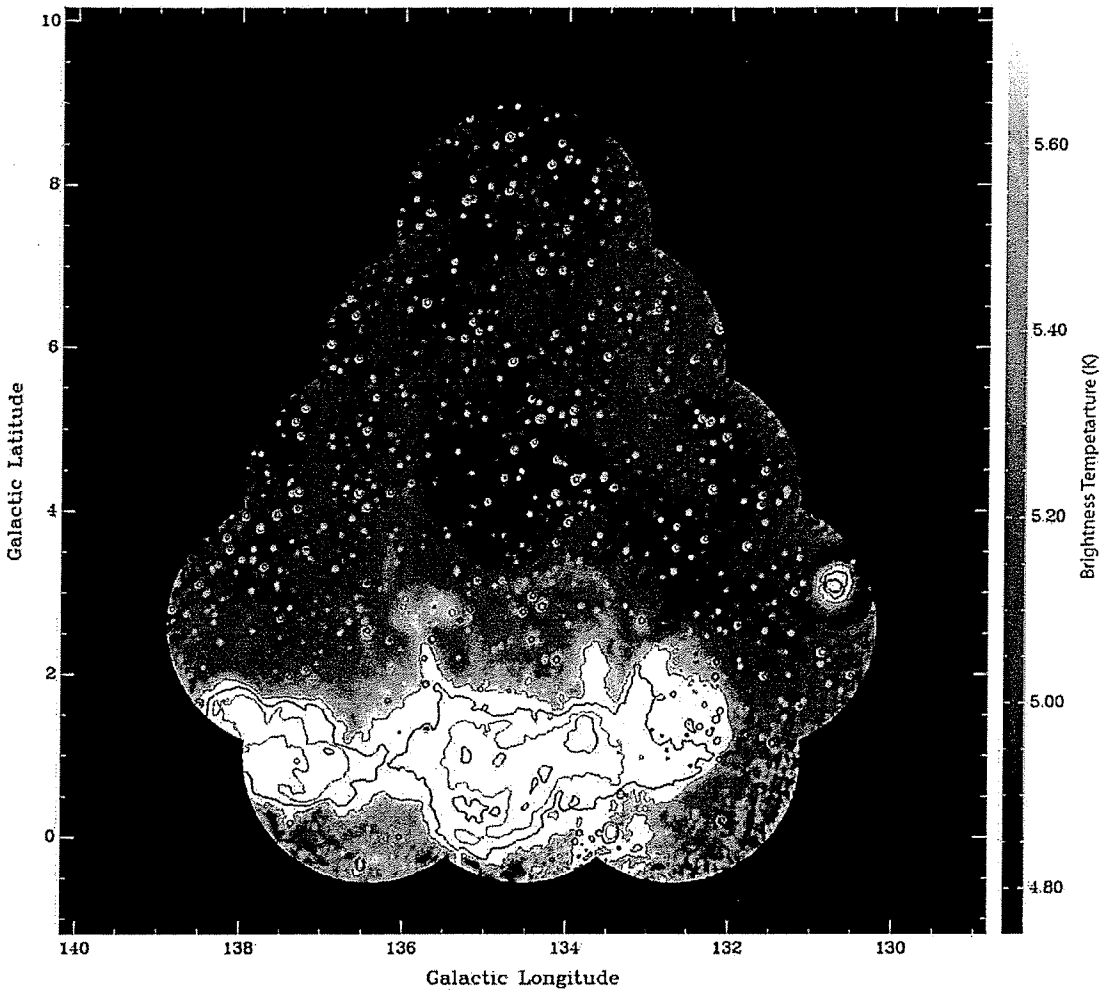

Figure 3-5: 1420 MHz (21 cm) Stokes I continuum image convolved to the resolution equivalent to the 408 MHz data and linearly scaled to show the fainter regions. Grey scale, shown at right, is brightness temperature which has been linearly stretched between 4.75 K (black) and 5.75 K (white). Black contours are set at levels of 16 K and 6.5 K and grey contours are set at 8.5 K and 5.75 K. The latitude and longitude scales shown have units of degrees.

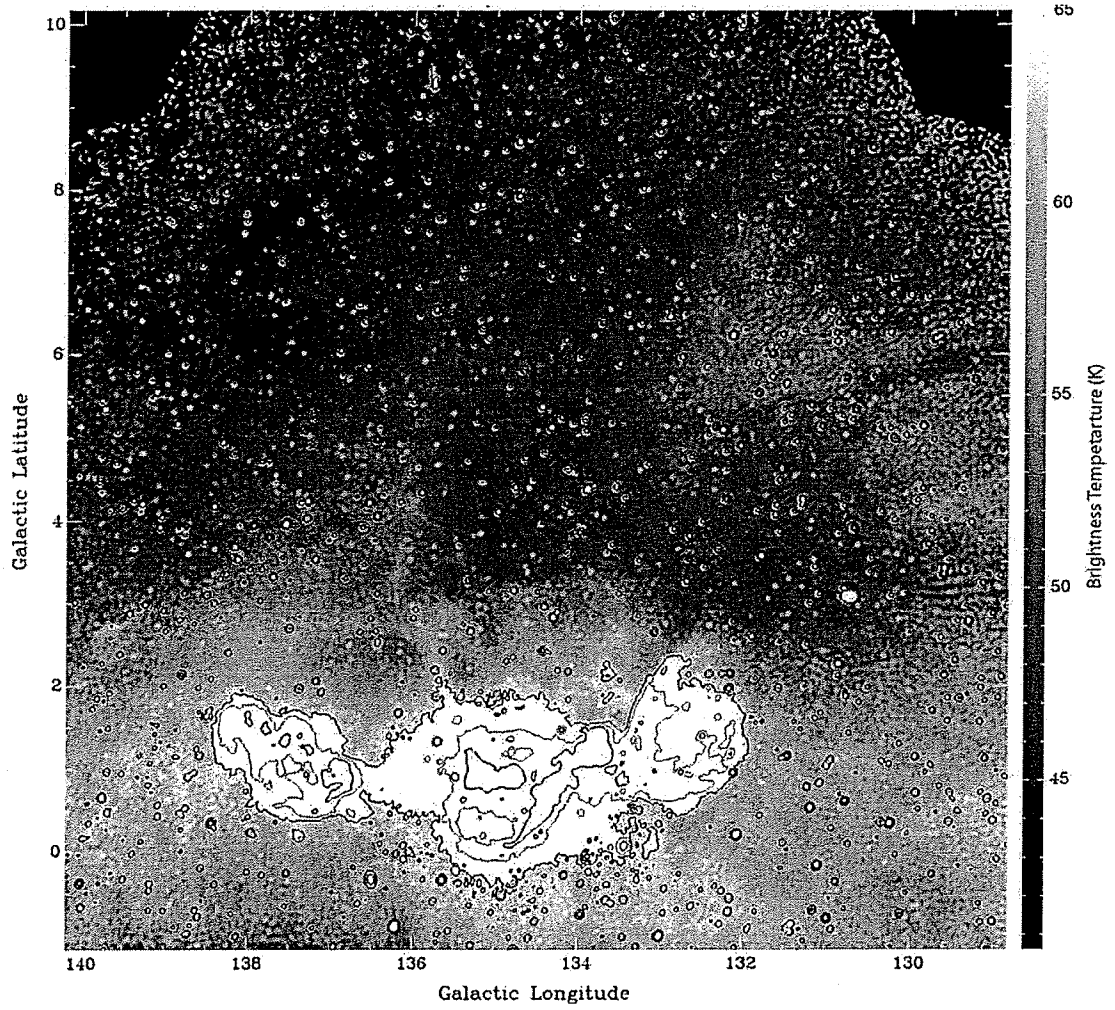

Figure 3-6: 408 MHz (74 cm) continuum image linearly scaled to show the faint emission. Grey scale, shown at right, is brightness temperature which has been linearly stretched between 40 K (black) and 65 K (white). The black contours are at levels of 120 K and 65 K. The grey contour is at 80 K. Note the dark ring of ~1.4° radius, centred at l = ~137°, b = ~7° (see discussion section 5.1.5). The latitude and longitude scales shown have units of degrees.

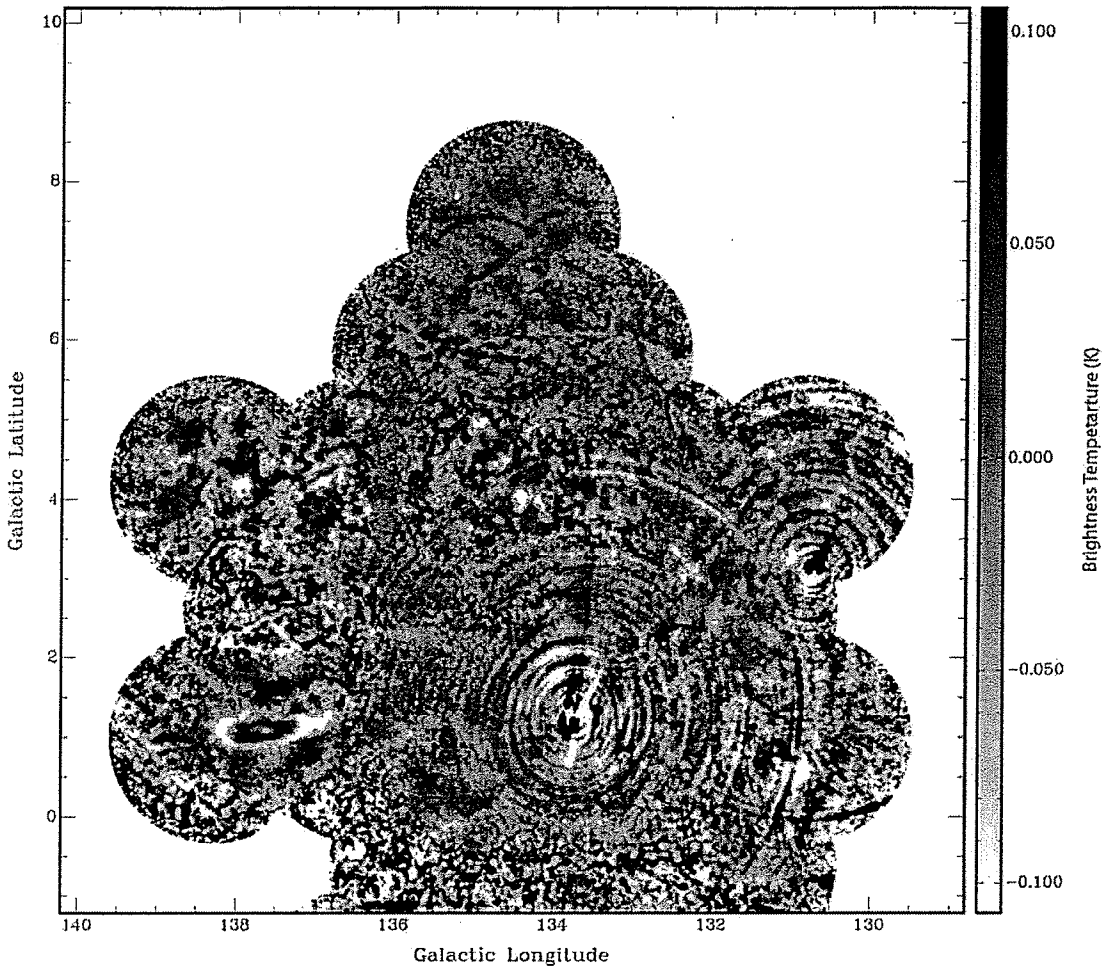

Figure 3-7: 1420 MHz (21 cm) Stokes Q image convolved to a resolution of 5' (see section 2.3.1). Rings are artefacts due to the bright sources W3 (centre) and 3C58 (right) (see Figure 3-21). Grey scale is in Kelvin and runs from ~-0.1 K (white) to ~0.1 K (black). The latitude and longitude scales shown have units of degrees.

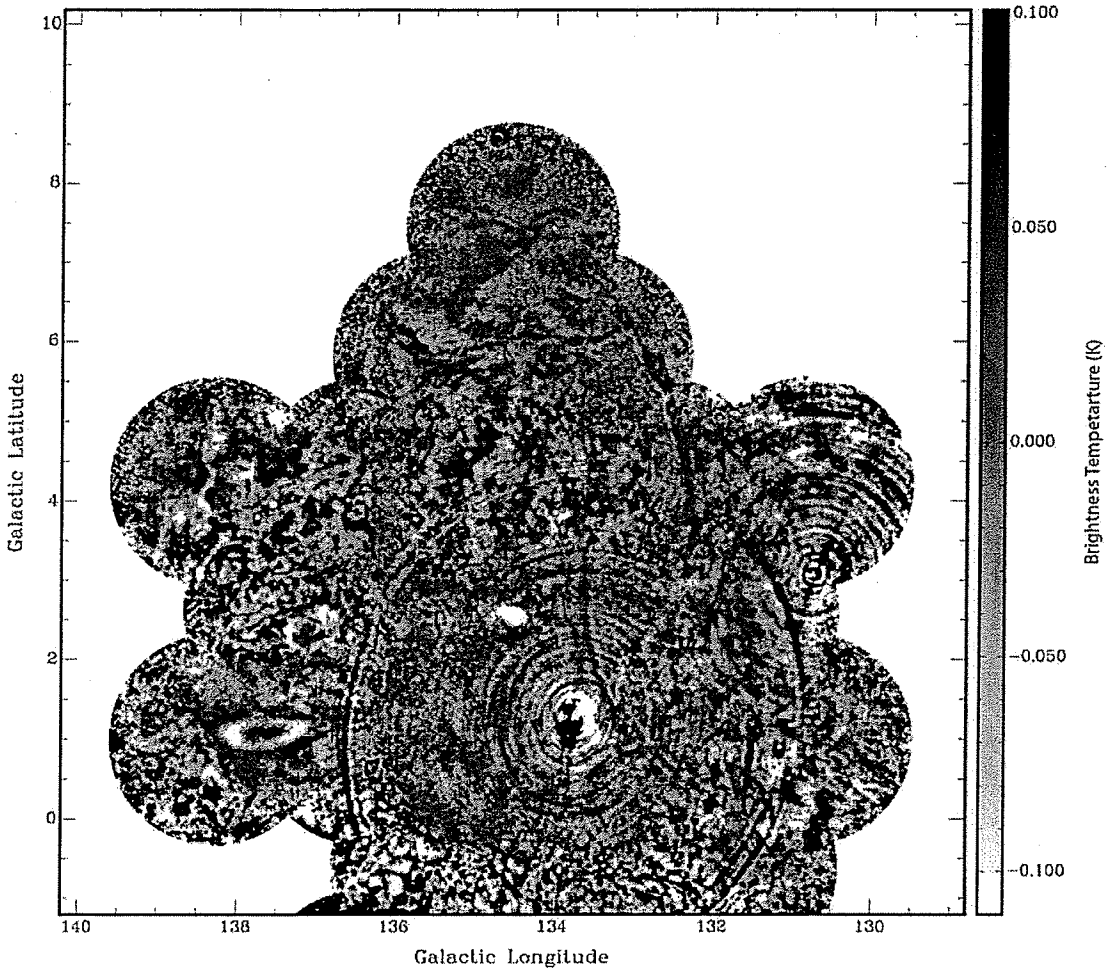

Figure 3-8: 1420 MHz (21 cm) Stokes U image convolved to a resolution of 5' (see section 2.3.1). Rings are artefacts due to the bright sources W3 (centre) and 3C58 (right) (see Figure 3-21). Grey scale is in Kelvin and runs from ~-0.1 K (white) to ~0.1 K (black). The latitude and longitude scales shown have units of degrees.

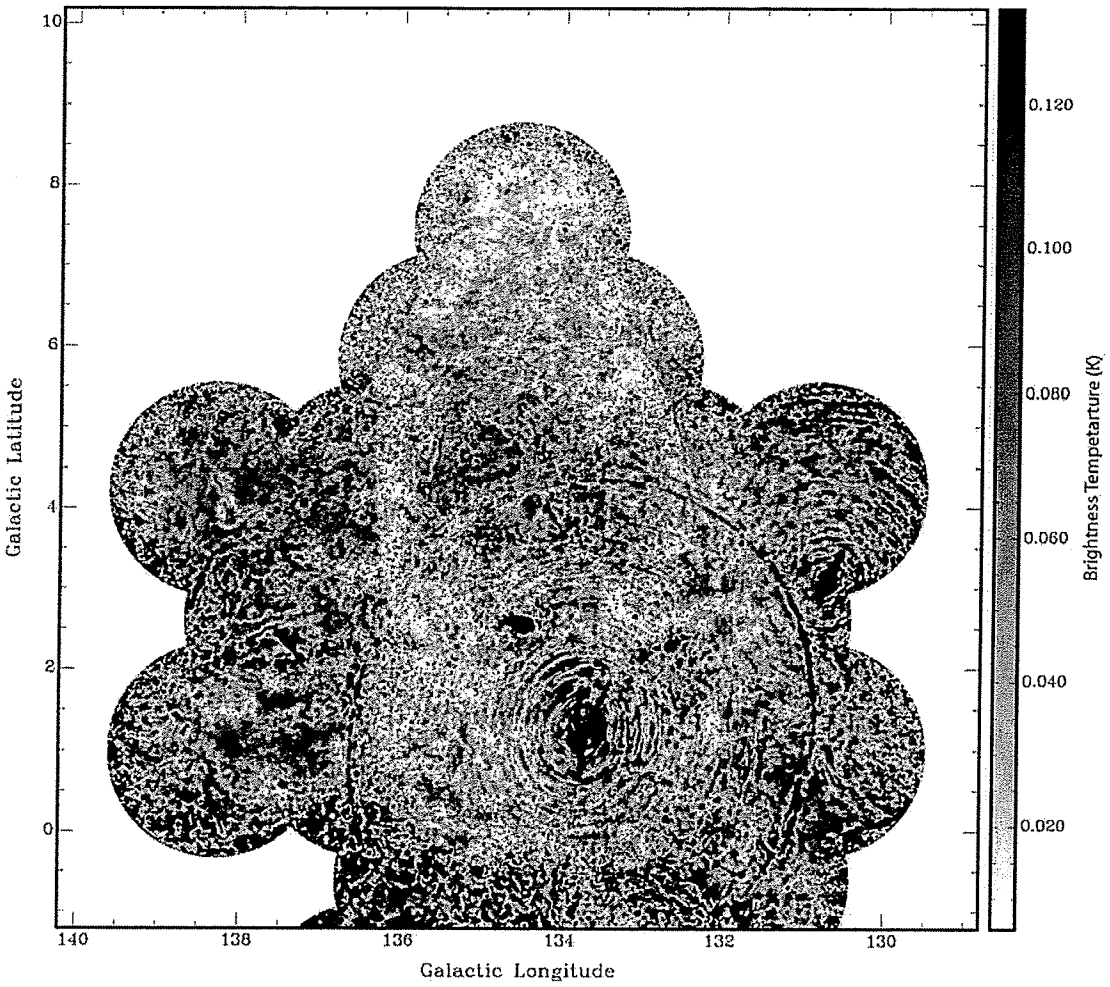

Figure 3-9: Polarized intensity, PI, image ($PI = \sqrt{Q^2 + U^2}$) (see section 2.2.2.1). The Q and U images were both convolved to a resolution of 5' and thus the PI map is also at a resolution of 5'. Grey scale is in Kelvin with and runs from 0 K (white) to 0.140 K (black) so that highly polarized regions appear black and depolarized regions show white. Note the depolarization along the "walls" of the region extending vertically upwards at l = ~136° and at l = ~133.5°. The "wishbone" (see section 5.1.4.1) shows grey with approximate centre coordinates l = 134.9°, b = 7.17°. Note also, the bright polarized "knot" (see section 5.1.4.2) centred at approximately l = 134.5°, b = 2.58° and showing as black. The latitude and longitude scales shown have units of degrees.

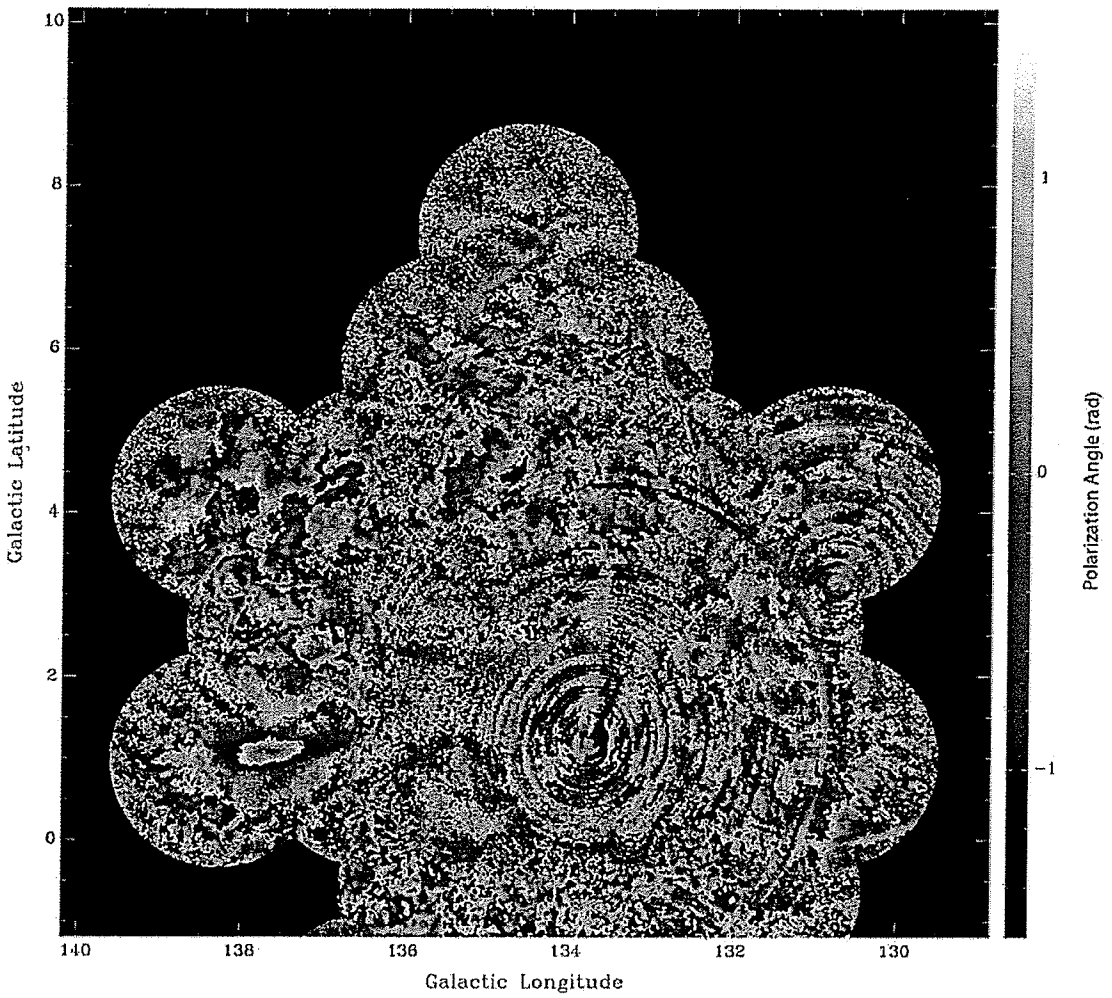

Figure 3-10: Polarization angle, ψ, map ($\psi = \frac{1}{2}\arctan\left(\frac{U}{Q}\right)$) (see section 2.2.2.2). The "wishbone" (see section 5.1.4.1) having approximate centre coordinates $l = 134.9°$, $b = 7.17°$ is especially evident here as a region of smoothly varying polarization angle. The interesting lenticularly shaped feature centred at approximately $l = 137.5°$, $b = 1°$ is roughly coincident with W5 but was discussed as likely being due to a foreground object by Gray et al. (1998, 1999). Note that depolarization along the "walls" of the region extending vertically upwards at $l = \sim 136°$ and at $l = \sim 133.5°$ which is seen as regions of low polarized intensity (Figure 3-9) can be seen here as a region having a small "cell size" (region over which ψ varies by 180°; Gray et al. 1999, see 5.1.1). The latitude and longitude scales shown have units of degrees.

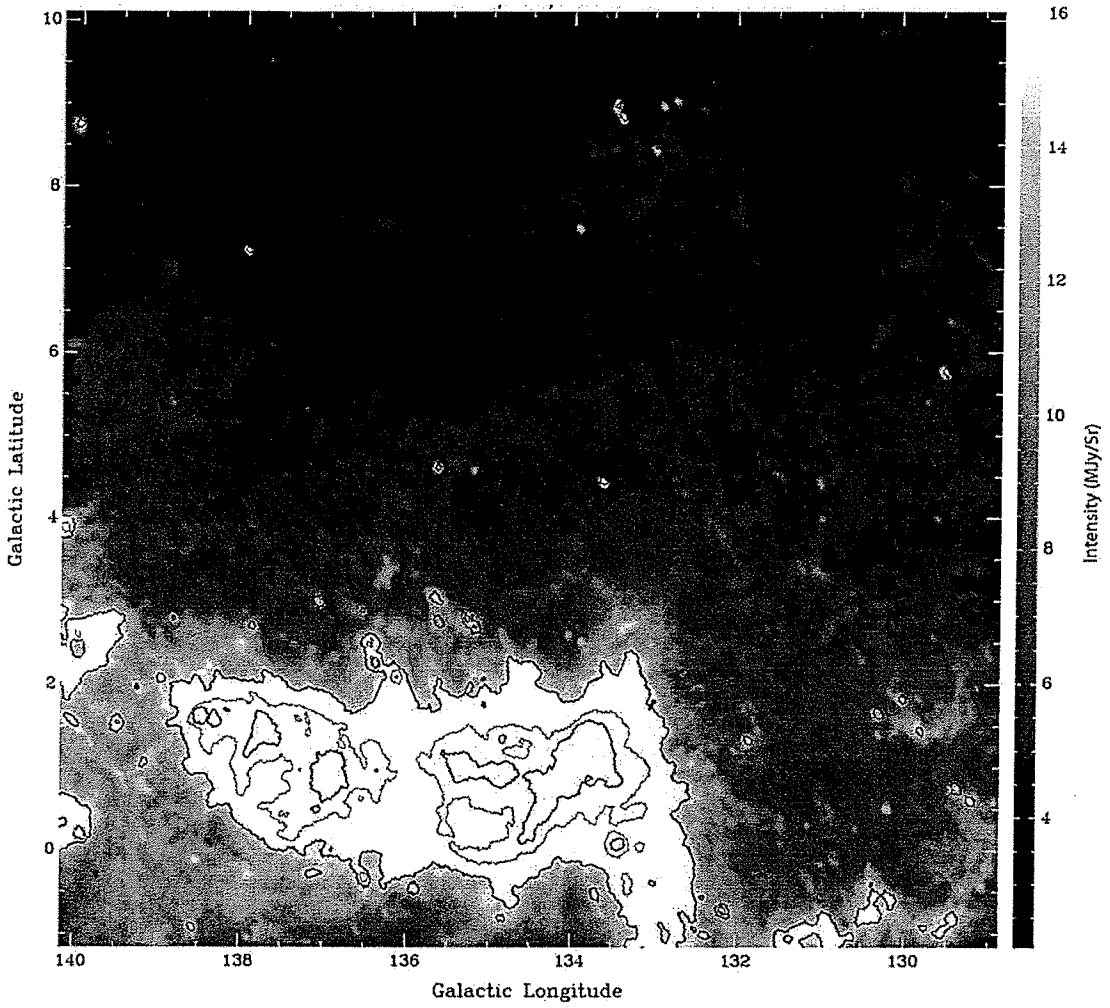

Figure 3-11: 60 μm infrared image from the IRAS survey linearly scaled to highlight faint emission. The grey scale runs from 2 MJy/SR to 16 MJy/SR. Black contours are set at 100 MJy/SR and 16 MJy/SR. The grey contour is at 40 MJy/SR. The "v" shaped feature with its apex at l = 134.5°, b = 2° is coincident with the "rabbit ears" visible in HI spectral line data and identified by Normandeau (1996) (see Figure 1-2). The latitude and longitude scales shown have units of degrees. Since the field of interest extends beyond the regular CGPS survey area, this image was obtained from SkyView (http://skyview.gsfc.nasa.gov/).

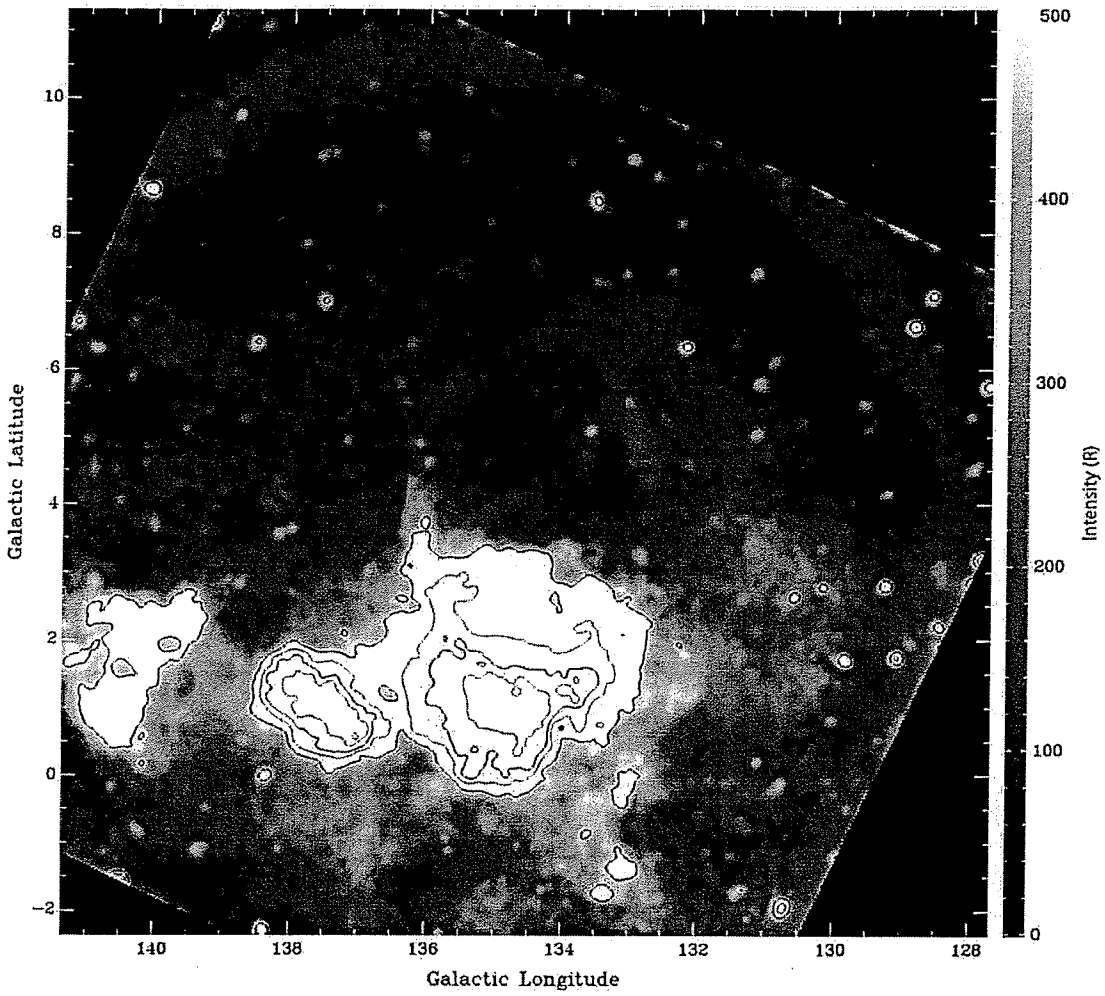

Figure 3-12: Hα image (DTS97) acquired for the Virginia Tech Spectral-Line Survey (VTSS), which is supported by the National Science Foundation. Grey scale is in units of Rayleighs [R] (see section 4.2.1 for a definition) and has been linearly scaled from 0 R (black) to 500 R (white) to highlight faint emission. Regions above 500 R are defined with contours. Grey contours are at levels of 4000 R and 1000 R. Black contours are set at 2000 R and 500 R. Image has been regridded to Galactic coordinates by the author using *mapconvrt* which is part of the DRAO export software package. The image has also been processed using DAOPHOT to remove many of the point sources. Note that the dark arc across the upper portion of image is an artefact of the image. See Figure 1-5 or Figure 4-2 for unprocessed versions of this image. The latitude and longitude scales shown have units of degrees.

3.4 Colour image catalogue

To aid in comparing the information in different images with each other, several false colour images were produced. The images were first log scaled to emphasize the faint emission. Each image is coloured and then placed in a "layer" in an image processing package. The layers are then combined using the "screen" algorithm. A combination of software was used for this processing. The log scaling was done in ImageJ (see Appendix 2). This software takes the natural log (base e) of the value of each pixel in the image. This was done twice resulting in a log scaling of base $e^e \approx 15$. The colouring and combining of the images was done using Gimp[3]. Further labeling was done using Adobe Illustrator[4].

Several colour images were produced which show the data in various combinations. Figure 3-13 to Figure 3-17 show the individual images coloured and log scaled since they are in the final combined images. Figure 3-18 shows the combined radio data, i.e. the 1420 MHz and 408 MHz images. Figure 3-19 includes the radio data as well as DTS97's Hα data and Nomandeau's (2000) HI. Finally, Figure 3-20 combines data at 1420 MHz, 408 MHz, Hα and 60 μm infrared data from the IRAS satellite.

---

[3] http://www.gimp.org/

[4] http://www.adobe.com/products/illustrator/main.html

In these data we have emission from the HII regions W3, W4 and W5, the supernova remnants HB3 and 3C58, as well as the spiral galaxy, Maffei 2. Additionally there are features which become more easily seen when combining the data such as the Hα superbubble identified by DTS97. We have drawn a 3D morphological bubble over this feature that is referred to as the *egg*[5]. We also define a *fork* which seems to be a continuous branch of emission coming off the main shape of the *egg*. Figure 3-21 shows these features labeled on the colour image of Figure 3-20. These features are discussed further in Chapter 5.

There are some additional features labeled in Figure 3-21. The "rabbits ears", the HI filaments, and the high latitude HI "spur" are neutral hydrogen features thought to be associated with the chimney and were identified by Normandeau (1996, 2000). The "wishbone" is a wishbone shaped feature centred at ~134.9°, 7.17° and most prominent in the polarization data (see Figure 3-7 to Figure 3-10). All are labeled here for positional reference purposes.

---

[5] Note that this "egg" is not based on the Kompaneets model of BJM99 but is instead a morphological contour of the intensity in the combined colour image.

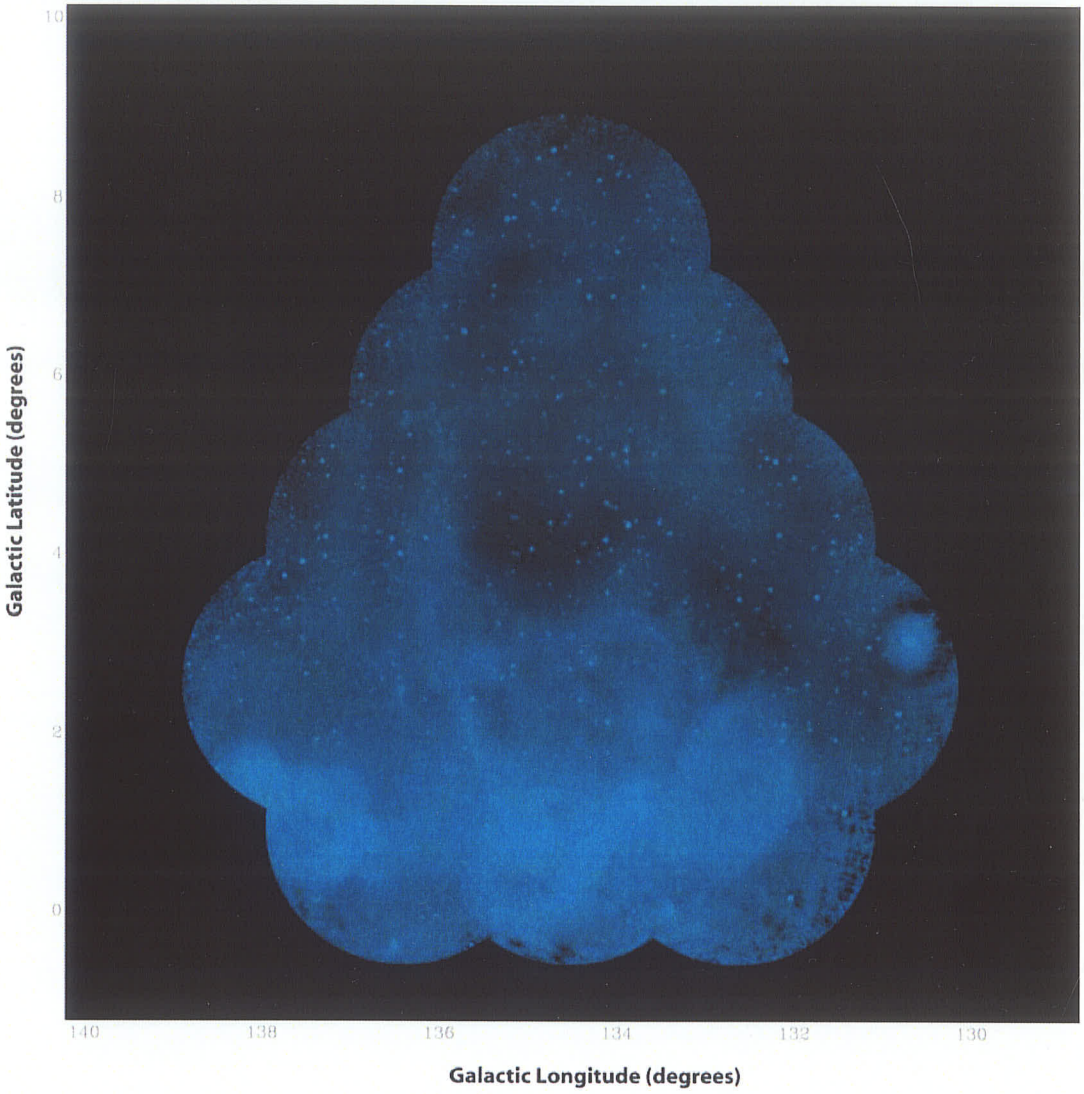

Figure 3-13: 1420 MHz image. Coloured turquoise and log scaled as described in the text.

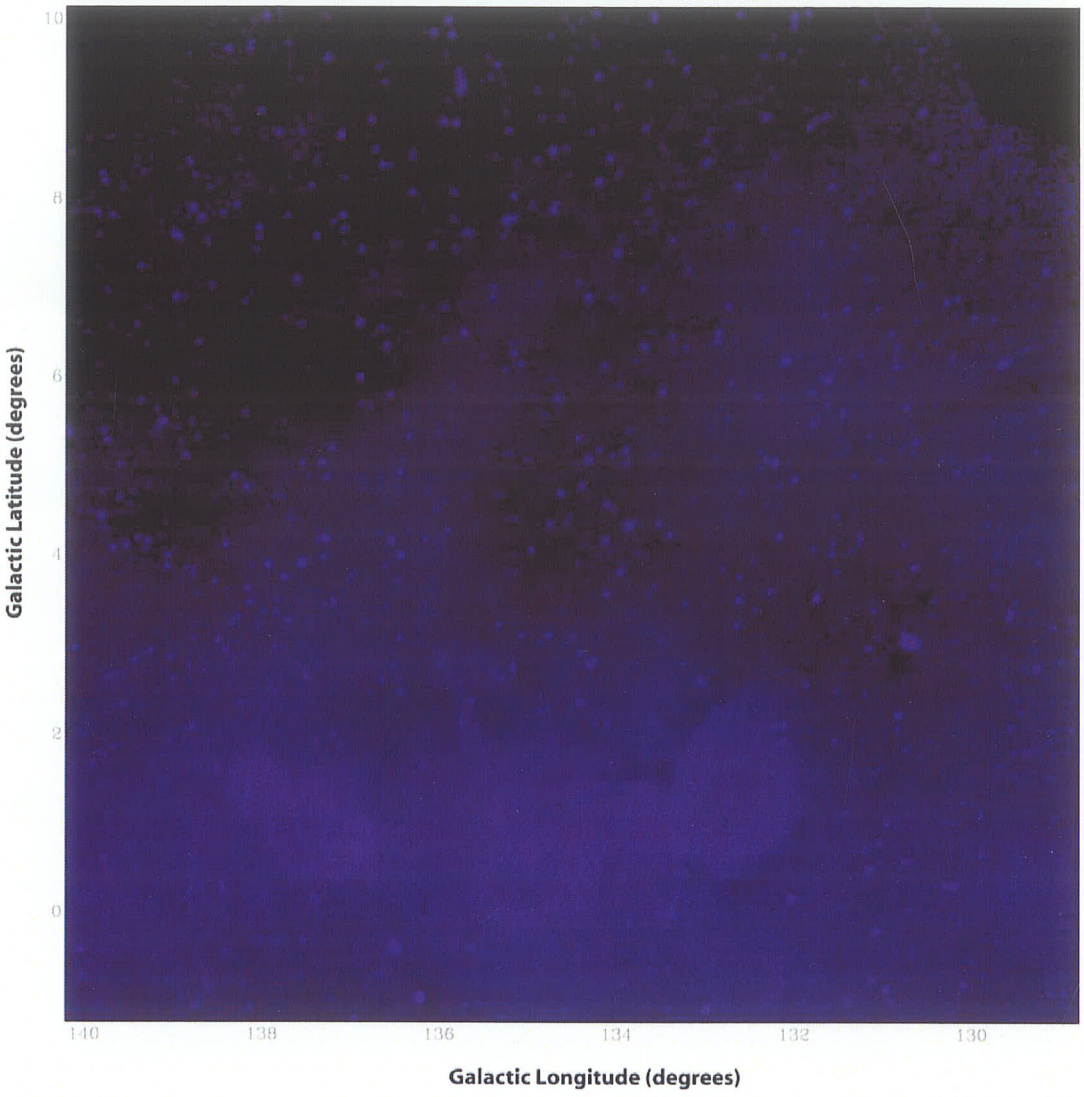

Figure 3-14: 408 MHz image. Coloured purple and log scaled as described in the text.

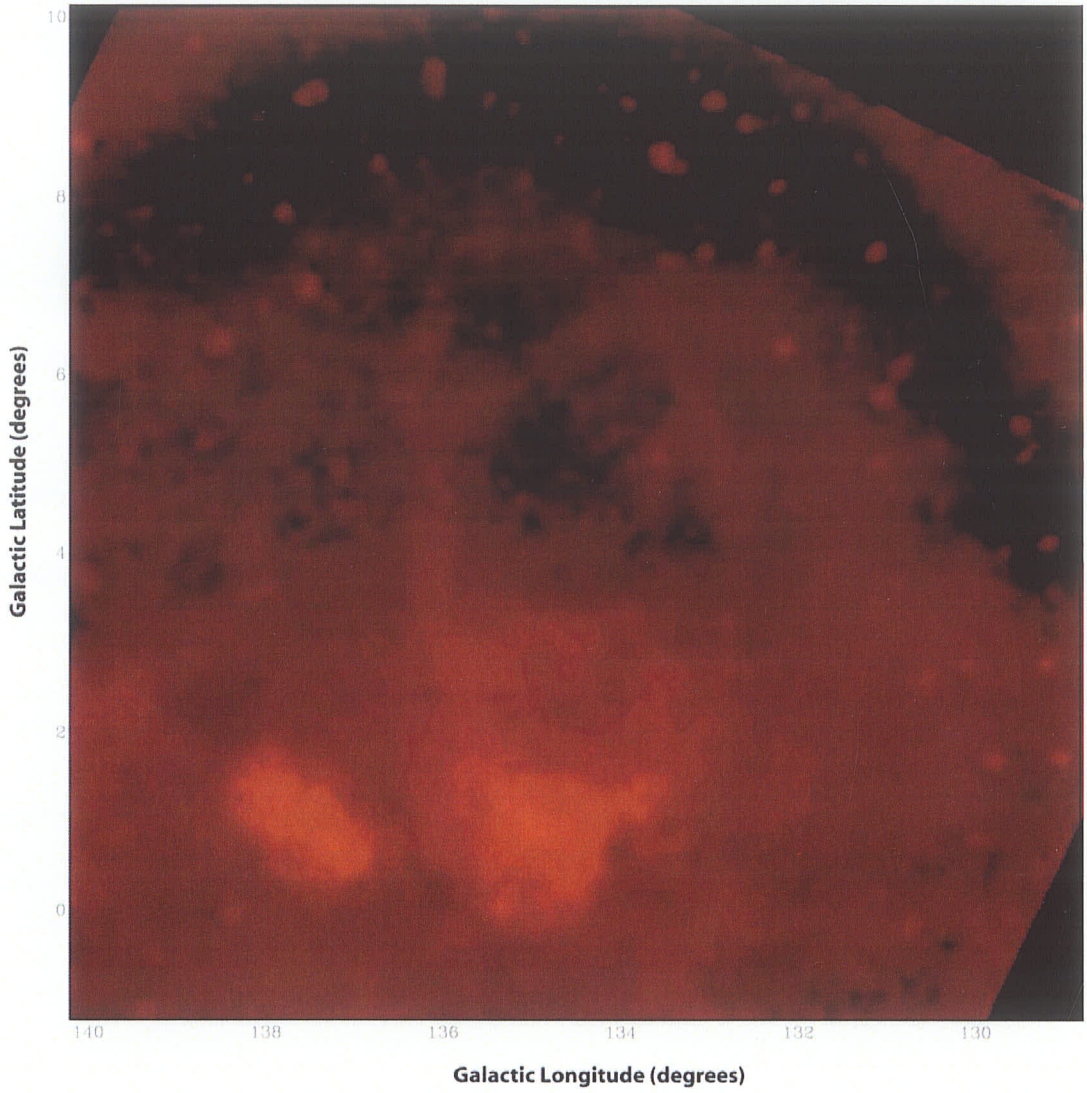

Figure 3-15: DTS97 Hα image. Coloured red and log scaled as described in the text.

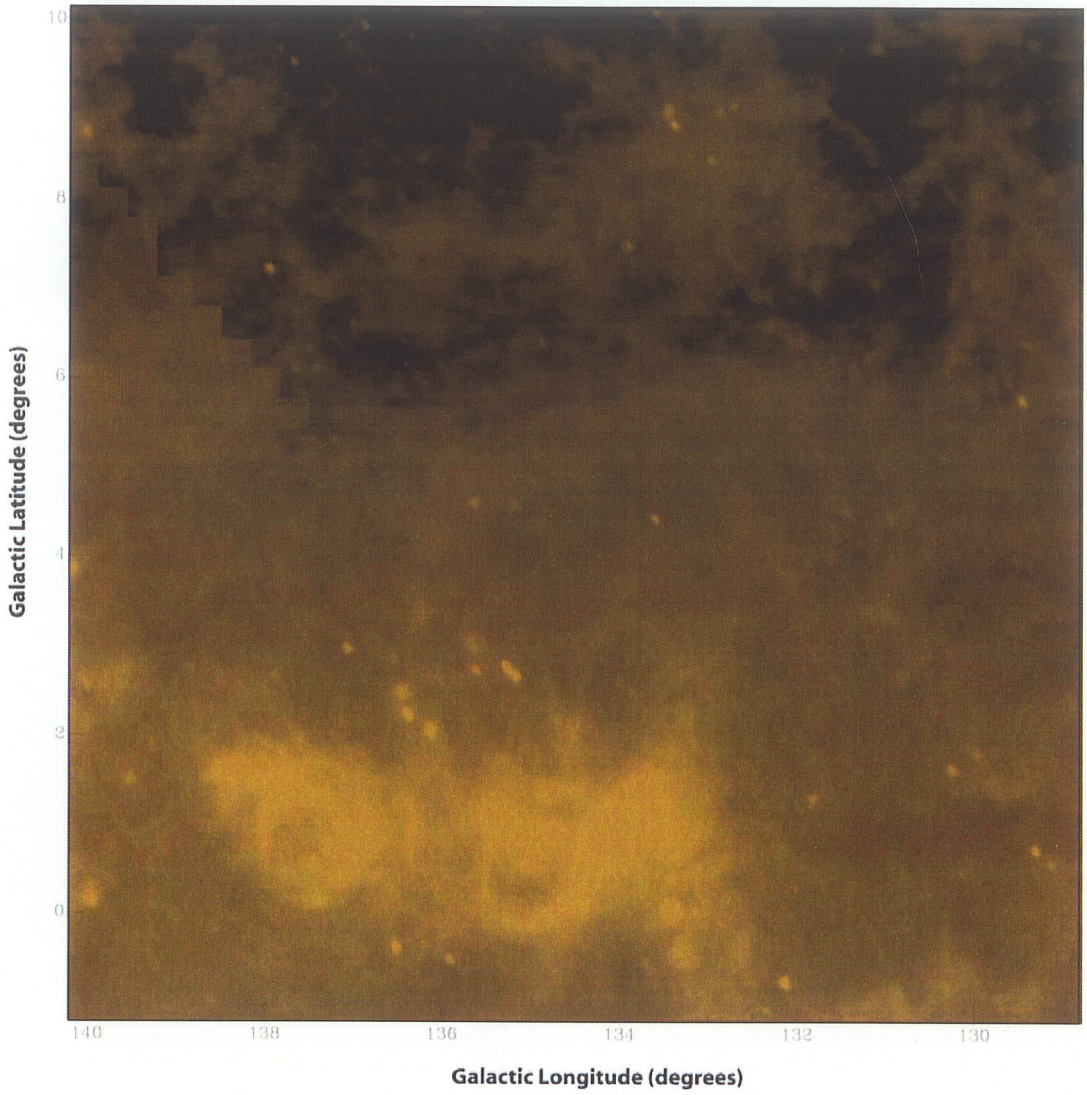

Figure 3-16: 60 μm IRAS image. Coloured yellow and log scaled as described in the text.

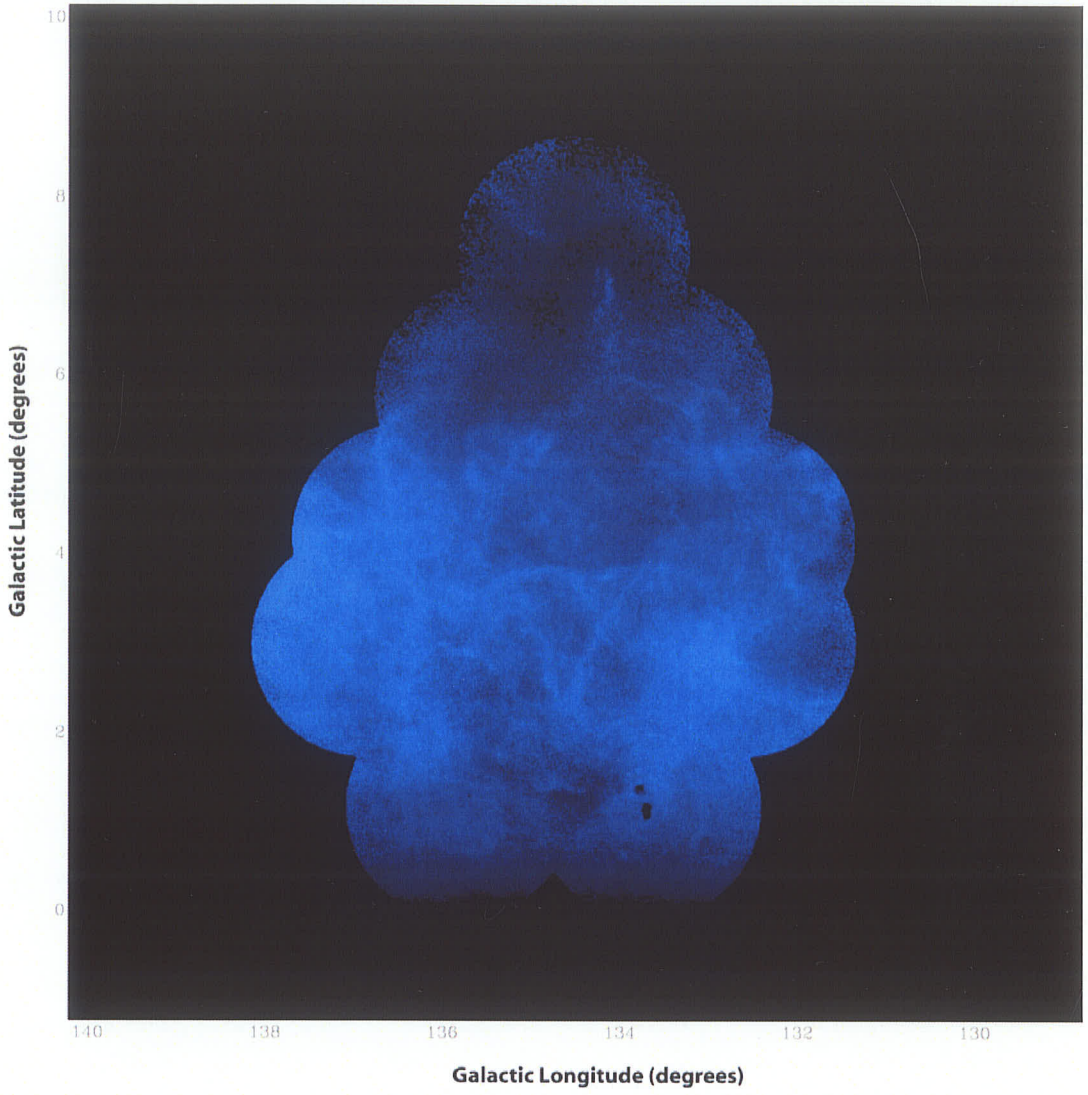

Figure 3-17: HI image from Normandeau (2000). This image has been coloured blue. A sin *b* scaling has been applied to this image as in Normandeau (2000) instead of a log scaling. The sin *b* scaling more effectively emphasizes the faint high latitude "spur" of HI emission that extends from ~(134.15°, 6.083°) to ~(134.175, 7.25).

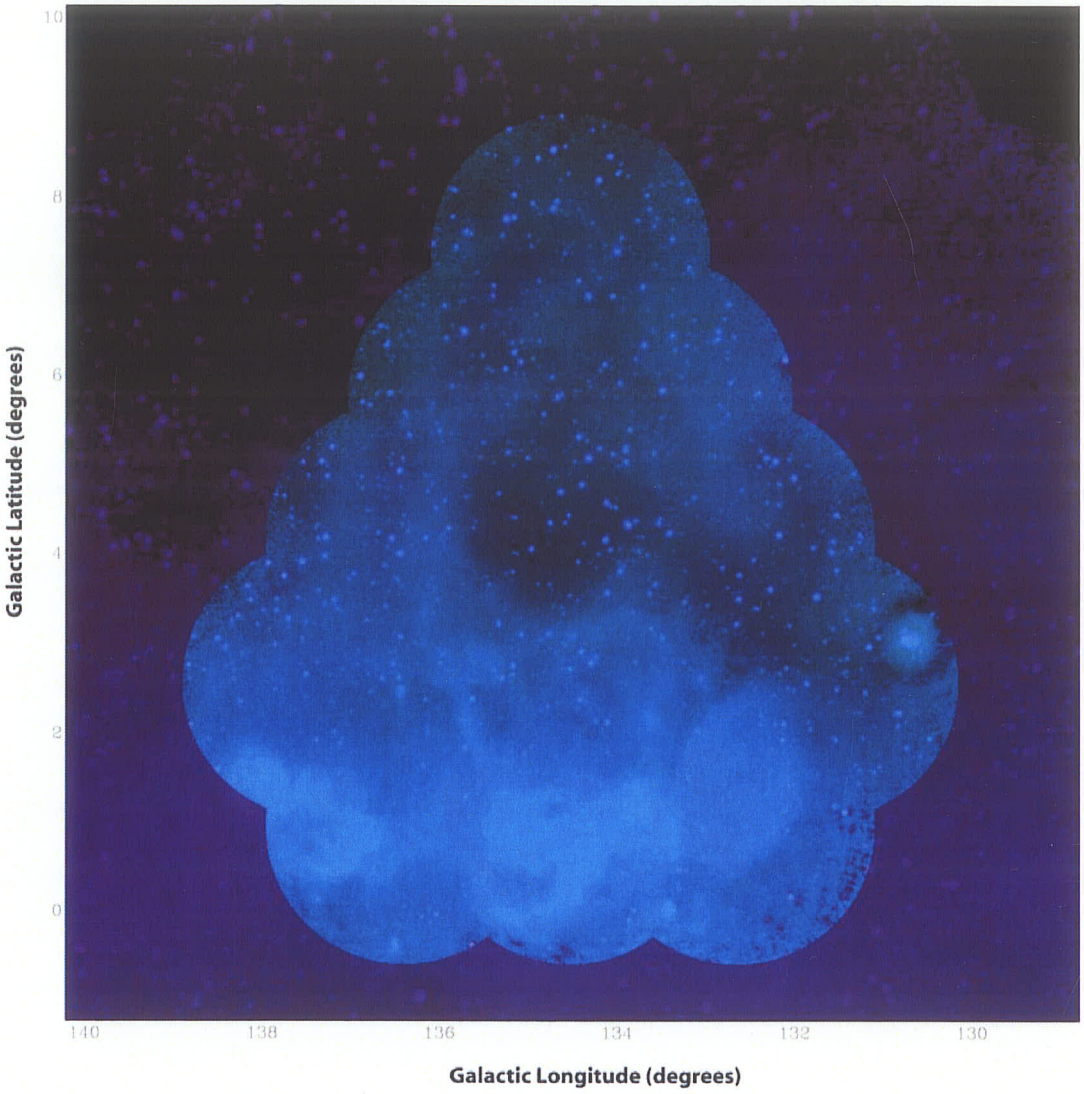

Figure 3-18: Combined radio data at 1420 MHz (turquoise) and 408 MHz (purple). Regions where overlap between the two datasets takes place show as blue. Greenish regions indicate that there the 1420 MHz dominates, while more purple regions indicate dominant 408 MHz emission.

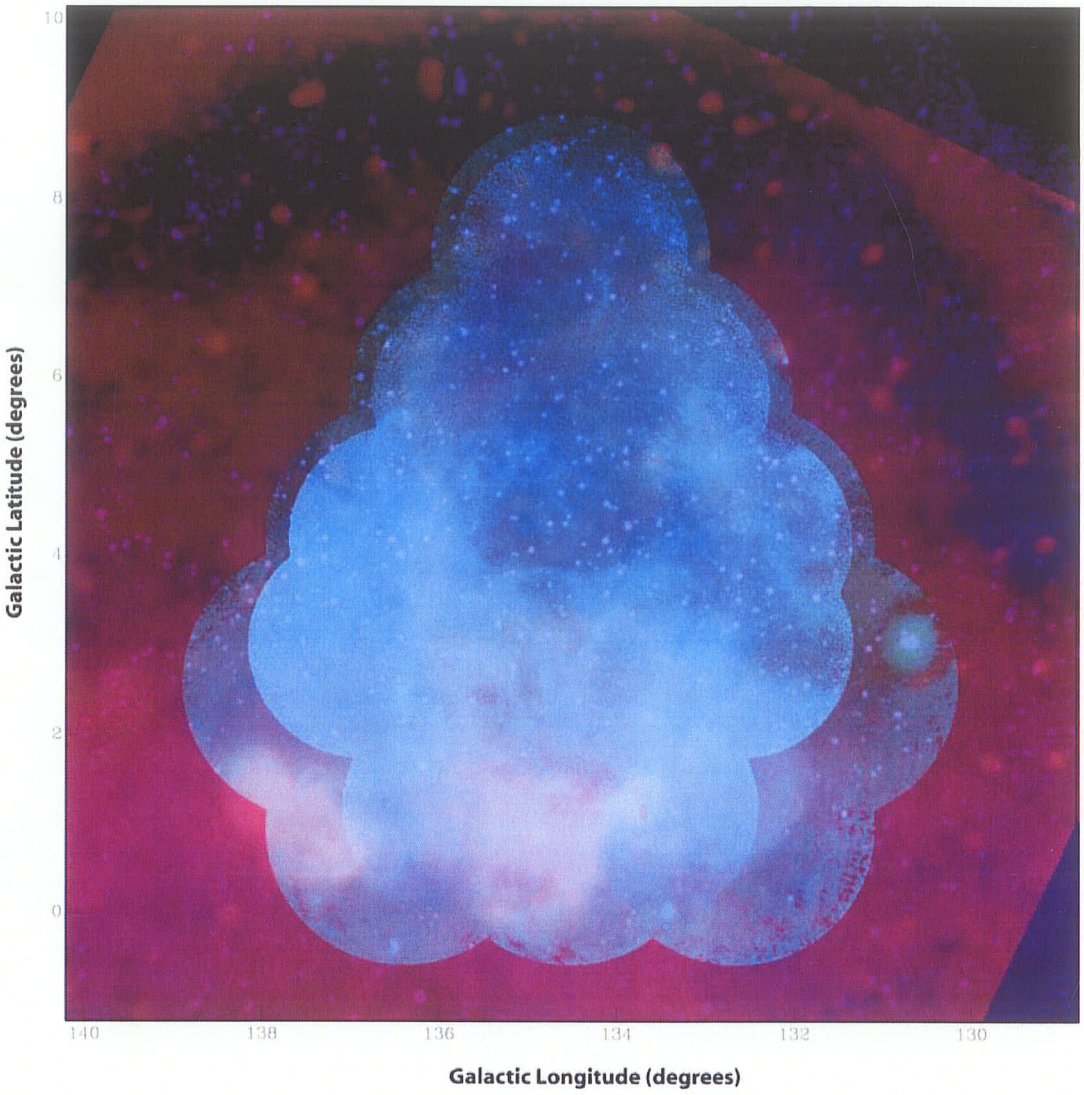

Figure 3-19: Combined radio data at 1420 MHz (turquoise) and 408 MHz (purple) with Hα (red) and HI (blue). Regions of overlap between all datasets show as purple-pink. The HI shows blue.

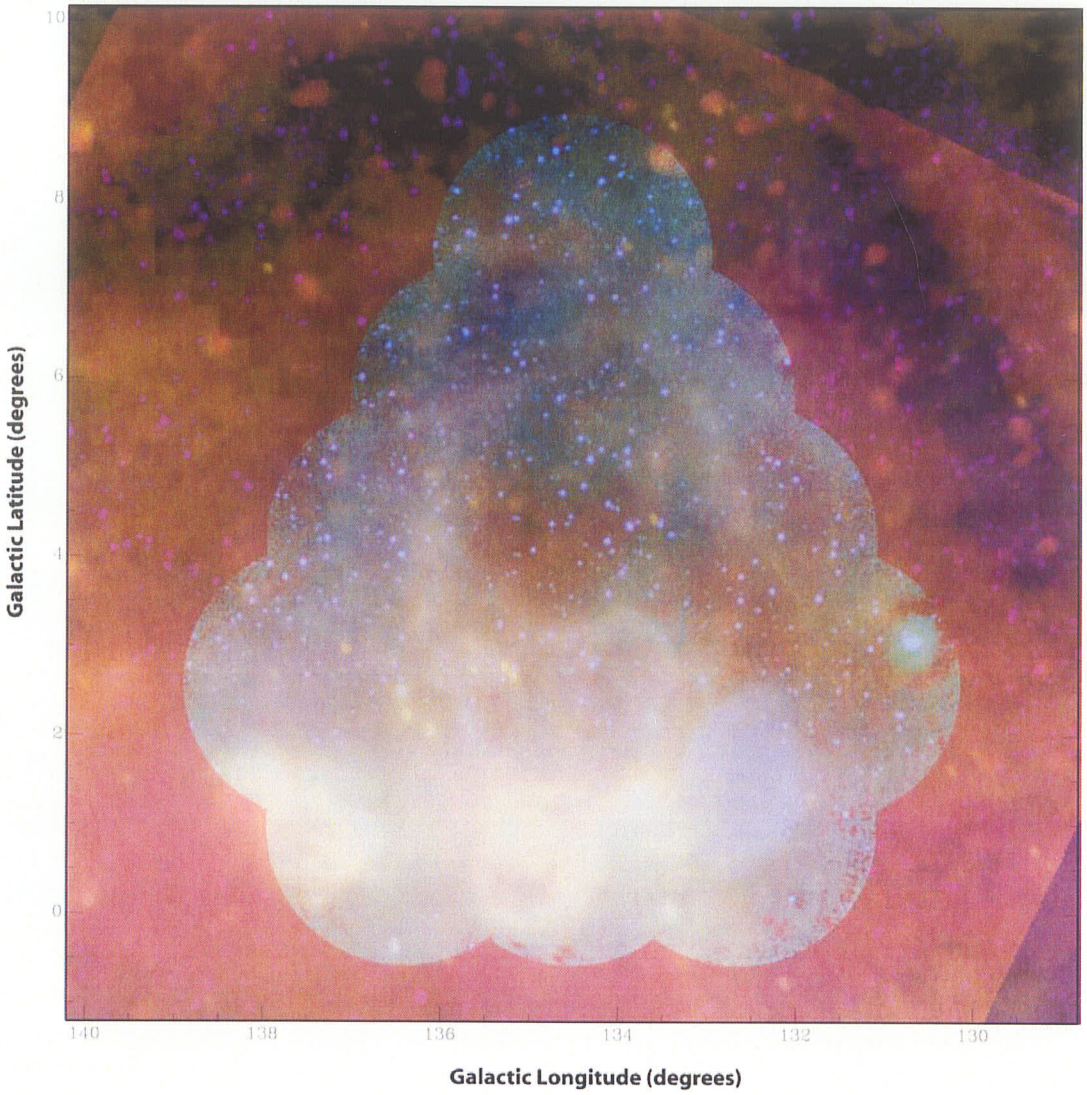

Figure 3-20: Combined 1420 MHz (turquoise), 408 MHz (purple), Hα (red), and 60 μm IRAS (yellow). Note the supernova remnant, HB3 shows a distinct purplish colour indicating dominant emission at 1420 and 408 MHz. Regions showing prominently as yellow have high dust emission.

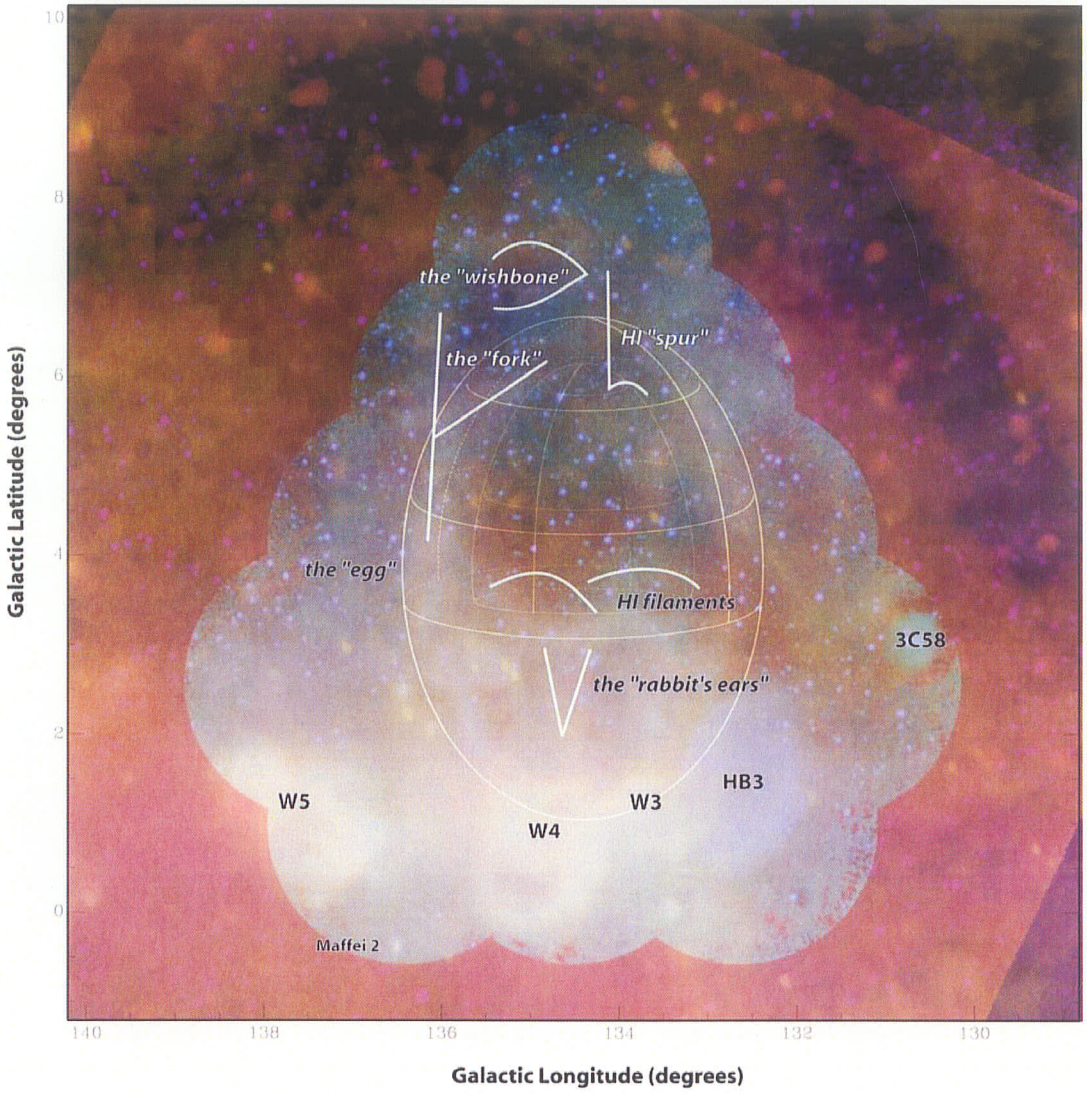

Figure 3-21: Colour image as described in Figure 3-20 with labels identifying objects with catalogue designations as well as prominent features visible in the data sets. The *egg* traces the contiguous structure apparent in these data. At our adopted distance of 2.3 kpc, the projected ellipse of the *egg* that measures ~4° wide by ~5.5° high and is ~165 pc wide by ~225 pc high. The "wishbone" is a feature visible in the polarization data. The "rabbit's ears" and filaments are HI spectral line features.

3.5 Measured intensity

The intensity of 56 regions that have been chosen to sample the interesting features are measured in the 1420 MHz and 408 MHz datasets as well as in polarized intensity. The discussion in Chapter 5 will make reference to these measurements. In addition, these measurements may be useful for further studies of the W4 region.

The 1420 MHz data are convolved to the same resolution as the 408 MHz data. The polarized intensity has been convolved to 5'. These regions are square boxes measuring 10' × 10' (30 × 30 pixels). The Galactic Longitude and Galactic Latitude of the centre of these 56 boxes, as well as the mean and standard deviation for each box are given in Table 3-2. The positions of these boxes are labeled in Figure 3-22. The regions are numbered by latitude, starting closest to the mid-plane.

			1420 MHz		408 MHz		Polarized Intensity		
Region #	l (°)	b (°)	mean (K)	σ	mean (K)	σ	mean (K)	σ	Comments on position
1	135.22	0.02	9.192	0.753	98.09	7.72	0.043	0.022	lower, small W4 loop, "C" (DTS97)
2	134.71	0.12	10.015	1.146	108.36	15.66	0.038	0.016	lower, small W4 loop, "D" (DTS97)
3	133.97	0.32	6.407	0.221	68.78	1.12	0.049	0.018	
4	135.49	0.37	7.695	0.382	83.68	6.41	0.053	0.024	lower, small W4 loop
5	135.32	0.43	6.397	0.306	72.22	2.08	0.066	0.017	lower, small W4 loop
6	132.22	0.52	5.110	0.040	59.44	0.85	0.047	0.020	below HB3
7	134.30	0.74	17.038	2.278	189.76	24.59	0.039	0.019	near "E" (DTS97)
8	132.40	0.85	6.565	0.168	81.56	6.08	0.035	0.018	HB3
9	136.02	0.86	6.496	0.068	69.80	0.59	0.030	0.015	between W4 & W5
10	134.79	0.96	16.505	3.495	193.78	41.65	0.033	0.014	OCl352, "SC" (DTS97)
11	135.20	0.97	16.451	1.900	179.69	20.00	0.062	0.029	"A" (DTS97)
12	136.87	1.05	13.982	2.626	152.03	31.63	0.066	0.028	W5
13	133.71	1.16	108.179	97.120	807.60	399.93	1.611	1.535	W3
14	133.21	1.32	7.196	0.124	83.50	4.59	0.075	0.023	between W3 & HB3
15	134.81	1.34	9.376	1.029	103.62	13.32	0.034	0.015	upper, small W4 loop, "O" (DTS97)
16	135.41	1.45	7.419	0.419	78.46	4.16	0.032	0.015	
17	135.61	2.02	6.112	0.192	64.78	2.18	0.025	0.013	near "F" (DTS97)
18	132.83	2.06	6.059	0.140	70.07	3.51	0.047	0.020	HB3
19	137.75	2.22	5.070	0.012	59.68	0.77	0.084	0.025	
20	133.64	2.26	6.076	0.191	63.86	2.01	0.050	0.019	near "M" (DTS97)
21	135.87	2.54	5.535	0.125	57.23	1.34	0.022	0.013	*ridge* (5.1.2)
22	134.47	2.58	5.224	0.067	57.60	1.09	0.191	0.048	polarized knot (5.1.4.2)
23	135.04	3.01	5.188	0.013	54.23	1.33	0.047	0.021	*ridge* (5.1.2)
24	132.49	3.05	4.824	0.016	51.19	0.63	0.050	0.021	side "break" (5.1.1)
25	133.96	3.23	5.283	0.044	54.17	0.99	0.046	0.016	*ridge* (5.1.2)
26	136.12	3.22	5.239	0.039	54.71	0.79	0.022	0.011	*eggshell*
27	134.85	3.54	4.881	0.022	49.90	0.50	0.080	0.017	low emission region (5.1.1)
28	133.01	3.78	4.807	0.013	51.15	0.66	0.049	0.020	side "break" (5.1.1)
29	136.11	3.96	5.104	0.011	54.04	0.65	0.035	0.011	near "G" (DTS97)
30	134.39	4.07	4.817	0.094	48.44	2.13	0.111	0.017	low emission region (5.1.1)
31	133.22	4.23	4.905	0.036	49.98	0.71	0.041	0.017	side "break" (5.1.1)
32	135.32	4.29	4.746	0.016	48.78	0.48	0.072	0.013	low emission region (5.1.1)
33	134.16	4.42	4.786	0.011	48.68	0.77	0.058	0.018	low emission region (5.1.1)
34	136.04	4.41	5.039	0.012	52.81	0.87	0.032	0.014	*eggshell*
35	134.92	4.44	4.774	0.011	47.90	0.50	0.076	0.014	low emission region (5.1.1)
36	137.08	4.47	4.990	0.010	51.82	0.73	0.086	0.018	
37	131.98	4.57	4.857	0.012	50.77	0.71	0.042	0.015	
38	135.91	4.85	4.965	0.013	51.79	0.47	0.048	0.024	*eggshell*
39	132.83	4.85	4.984	0.007	52.67	0.55	0.038	0.018	*eggshell*

			1420 MHz		408 MHz		Polarized Intensity		
Region #	l (°)	b (°)	mean (K)	σ	mean (K)	σ	mean (K)	σ	Comments on position
40	134.91	4.95	4.838	0.010	48.77	0.60	0.097	0.018	low emission region (5.1.1)
41	133.23	5.07	4.984	0.009	49.48	0.48	0.035	0.015	*eggshell*
42	135.38	5.08	4.876	0.047	49.40	0.63	0.058	0.019	
43	135.69	5.45	4.926	0.015	51.14	0.54	0.028	0.014	*eggshell*, near "H" (DTS97)
44	134.06	5.64	4.935	0.013	48.81	0.60	0.039	0.012	
45	133.14	5.75	5.053	0.031	51.37	0.65	0.019	0.009	*eggshell*, near "K" (DTS97)
46	135.39	5.78	4.945	0.012	50.48	0.85	0.043	0.022	*eggshell*
47	133.56	6.26	5.013	0.013	49.66	0.75	0.030	0.012	*eggshell*
48	134.34	6.52	4.937	0.014	47.89	0.55	0.023	0.012	*eggshell*
49	134.09	6.57	4.932	0.010	47.65	0.61	0.027	0.011	top "break" (5.1.1)
50	133.79	6.71	4.990	0.017	47.52	0.58	0.033	0.014	*eggshell*, near "J" (DTS97)
51	135.54	6.79	4.846	0.012	49.45	0.83	0.028	0.014	
52	134.93	6.84	4.947	0.049	49.99	0.86	0.039	0.014	polarized *wishbone* (5.1.4.1)
53	135.89	7.16	4.962	0.026	46.69	0.65	0.025	0.040	*fork* (5.1.1)
54	135.16	7.27	4.803	0.008	49.10	0.88	0.027	0.011	
55	134.37	7.29	4.942	0.042	48.66	0.65	0.038	0.012	polarized *wishbone* (5.1.4.1)
56	135.14	7.52	4.852	0.020	48.07	0.80	0.032	0.014	polarized *wishbone* (5.1.4.1)

Table 3-2: Mean intensity and standard deviations (σ) for the fifty-six 10'×10' boxes shown in Figure 3-22. Measurements were done for the 1420 MHz data (convolved to the resolution of the 408 MHz data), 408 MHz data, and polarized intensity (convolved to 5'). Comments indicate where correspondences exist with significant features. Features are discussed in the sections indicated in parentheses. Where a box is co-spatial with a point measured by Dennison et al. (DTS97) (points "A" through "O", Figure 4-2), the point is indicated.

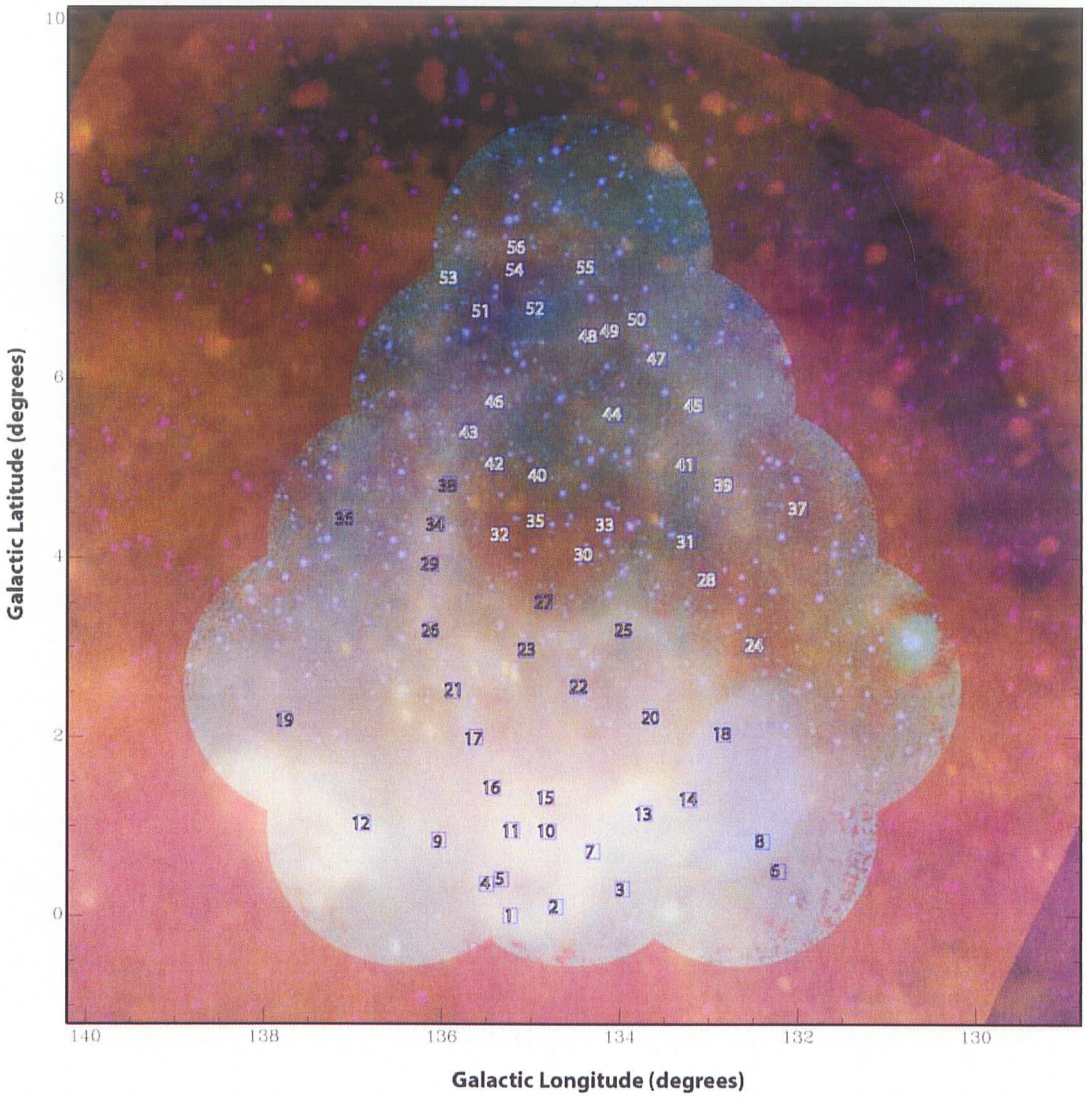

Figure 3-22: The mean intensity was measured for each of the fifty-six 10' × 10' boxes shown. Measurements are given in Table 3-2. Colour is the same as in Figure 3-20.

4: Analysis

In section 4.1 emission levels at 1420 and 408 MHz are compared by means of a spectral index map. This is done as an effort to determine whether the emission of a particular region is thermal or non-thermal. The relevance of this analysis in assessing the W4 chimney candidate is explained.

Section 4.2 presents an exploration of the magnetic field in the W4 region by means of producing a rotation measure map and utilising the Hα data of DTS97 to estimate the *egg*'s electron density.

4.1 Spectral index

4.1.1 Computing the spectral index map

A relatively flat temperature spectral index ($\beta < 2.6$) for the interior of the W4 *egg* region would support the chimney model for this region since it would suggest that cosmic rays (CRs) are transported by convection and have the energy necessary to escape. If this is also true at higher latitudes then the chimney could be a contributer to the observed CRs in the halo. See section 2.1.3 for additional information. To investigate this, a temperature

spectral index map over the W4 region was produced using the CGPS 408 MHz and 1420 MHz continuum data.

Often plots of ν_1 vs ν_2, referred to as T-T plots, are used to determine spectral indices as opposed to producing a map. T-T plots offer some advantages such as having the ability to identify an offset in the data. However T-T plots are dominated by the low resolution information where maps are not, offering the advantage of being able to spatially discriminate features which is particularly desirable in this case.

Temperature spectral index maps for the W4 region have been produced by both Kallas, Reich, and Haslam (1983, hereafter KRH83) and Reich and Reich (1988, hereafter RR88). In both cases the resolution of the maps is much lower than the ~4' resolution of the 408 MHz data; 48' in the case of KRH83 and 2.5° for the RR88 map. The higher resolution in the CGPS data will provide some additional insight into the morphology of the region.

The maps of KRH83 and RR88 use the same data that have been added to the CGPS data in the form of short spacings (recall section 3.2.1, the data in the spectral index maps of KRH83 and RR88 have been convolved to match other datasets). Thus it is reasonable to apply results from their maps to our data.

We are interested in computing the spectral index for the W4 region itself and therefore we wish to remove the emission that is occurring in front of W4 (i.e. ambient Galactic

foreground emission), behind W4 (i.e. extra-Galactic contributions), contributions from the Cosmic Microwave Background (CMB), and instrumental contributions.

The KRH83 map presents results for the "background" radiation that is in fact the ambient "foreground" radiation and thus does not include the radiation from the W4 region. They find that in the region along the line of sight to W4 there is an intervening large scale "Steep Spectral Feature" (SSF) extending from l = 110° to l = 170°. Comparisons with maps of starlight polarization show a striking alignment of polarization vectors with the SSF and imply distances of 100 to 200 pc. Other observations imply distances up to 500 pc, but this is still much closer than the adopted distance to W4 of 2300 pc. The results from this map are important since they define the spectral index of this intervening foreground emission. This result is used to remove the contribution of the SSF from our map.

The results of RR88 are also useful since they calculate an offset temperature, T_{off}, which includes the contributions to the brightness temperature, T_B, (see section 2.1) at 1420 MHz and 408 MHz from the cosmic microwave background radiation and from extra-Galactic sources as well as zero-level corrections to the data. Their values for these quantities were subtracted from our data before making the spectral index map. Table 4-1 summarizes the offset correction of T_{SSF} from KRH83 and T_{off} from RR88.

	T_{SSF} [K] (KRH83)	T_{off} [K] (RR88)
1420 MHz	~0.48	2.8 ± 0.03
408 MHz	~20.5	3.7 ± 0.85

Table 4-1: Offset corrections for the spectral index map.

The contributions to the detected emission from the various descriptions presented in the literature are summarized

$$T_{observed} = T_{ambient} + T_{\substack{total \\ map}} + T_{instrumental} \qquad (4\text{-}1)$$

where

$$\begin{aligned} T_{ambient} &= T_{CMB} + T_{extragalactic} \\ T_{off} &= T_{ambient} + T_{instrumental} \\ T_{observed} &= T_{\substack{total \\ map}} + T_{off} \end{aligned} \qquad (4\text{-}2)$$

$$\therefore T_{\substack{total \\ map}} = T_{observed} - T_{off}.$$

$T_{\substack{total \\ map}}$ is the sum of all Galactic objects along the line of sight including contributions from HII regions and supernova remnants (SNRs) but also includes the contribution of the steep spectral feature detected by KRH83. Therefore to find $T_{\substack{W4 \\ region}}$, T_{SSF} must be subtracted

$$T_{\substack{W4 \\ region}} = T_{\substack{total \\ map}} - T_{SSF} \qquad (4\text{-}3)$$

and in terms of contributions of the components of Galactic emission (see section 2.1.3)

$$T_{\substack{W4 \\ region}} = T_{\substack{HII \\ regions}} + T_{SNR} + T_{\substack{residual \\ diffuse \\ non-thermal}} \quad . \qquad (4\text{-}4)$$

The high spatial resolution of the CGPS data enable one to distinguish T_{SNR} (i.e. HB3) from $T_{\substack{HII \\ regions}}$ (i.e. W3/W4/W5).

The third term in Eq. (4-4) is the *residual* diffuse non-thermal emission since T_{SSF} is largely due to diffuse non-thermal emission in the Galaxy and most of the diffuse component has been subtracted off when creating the map. We note that this is likely a significant contribution to the error in our map since some of the emission from T_{SSF} may be originating in the W4 region itself. Without subtracting the SSF, the map steepens on average by about 0.2 to 0.3.

Additionally, there may be ~15% systematic error in the CGPS data (see section 3.2). This contributes to an error in our temperature spectral index map such that the absolute level of this spectral index map is uncertain by ~5% and internally there is ~2.5% error. For this reason, the map must be discussed in *relative* terms (i.e. steeper vs flatter). It is possible to make a reasonable estimate at the absolute scale by comparing the values in the map with expected values (see Table 2-1) since the region contains several HII regions and the supernova remnant, HB3. Further indication of the absolute scale can be

found by comparing our data with previously published results. See section 4.1.2.1 for these comparisons.

Since the 408 MHz data is at a lower resolution (3.5' × 4') than the 1420 MHz data (1' × 1.14'), the latter must be convolved so that the two data sets have matching resolution (Figure 3-5). This was accomplished using *mosconv* which is part of the DRAO export software package (see Appendix 1).

The spectral index map was produced by applying Eq. (2-14) pixel by pixel to the 1420 MHz and 408 MHz images after the baselevel corrections were made according to Eq. (4-3) and using the values from Table 4-1. This was accomplished using the public domain program, ImageJ (see Appendix 2).

4.1.2 Results of the temperature spectral index map

Figure 4-1 illustrates the resulting temperature spectral index map.

4.1.2.1 Comparing our map with values from the literature

By comparing the values in the temperature spectral index map with expected canonical values (see Table 2-1) and with previously published results we may attempt to establish

an absolute scale for the map. The regions compared are the HII regions, W3/W4/W5 and the supernova remnant HB3.

The HII regions should have a temperature spectral index from $0 < \beta < 2.1$ (see section 2.1.3). In our map the HII regions have $\beta < 2.1$, ranging between 1.9 and 2.0 over much of the region. This was determined visually using the image visualization tool kview which is part of the Karma[6] package. Karma's pseudo-colourmap Glynn Rogers1 was applied and adjusted to show the maximum colour discrimination over the range of interest (i.e. from about $\beta = 1.5$ to $\beta = 2.2$). In the case of W3 the temperature spectral index goes as low as ~1.6. These comparisons indicate that the β from our map are within the expected range.

Supernova remnants have on average, $\beta \approx 2.5$ (see Table 2-1). In the case of HB3, its spectral index has been previously published. Normandeau (1996) and references therein give values of $\alpha = 0.5 \pm 0.2$, 0.64 ± 0.01 and 0.60 ± 0.04 for the integrated emission of HB3. These correspond to $\beta = 2.5 \pm 0.2$, 2.64 ± 0.01 and 2.60 ± 0.04 respectively. Our map indicates that the filaments of the SNR have a β between 2.3 and 2.4, as determined by visual inspection. These results indicate that the values on our map are too low by between 0.2 and 0.3. We note that this result is equivalent to the difference found when producing a temperature spectral index map without first subtracting the SSF.

---

[6] http://www.atnf.csiro.au/computing/software/karma/

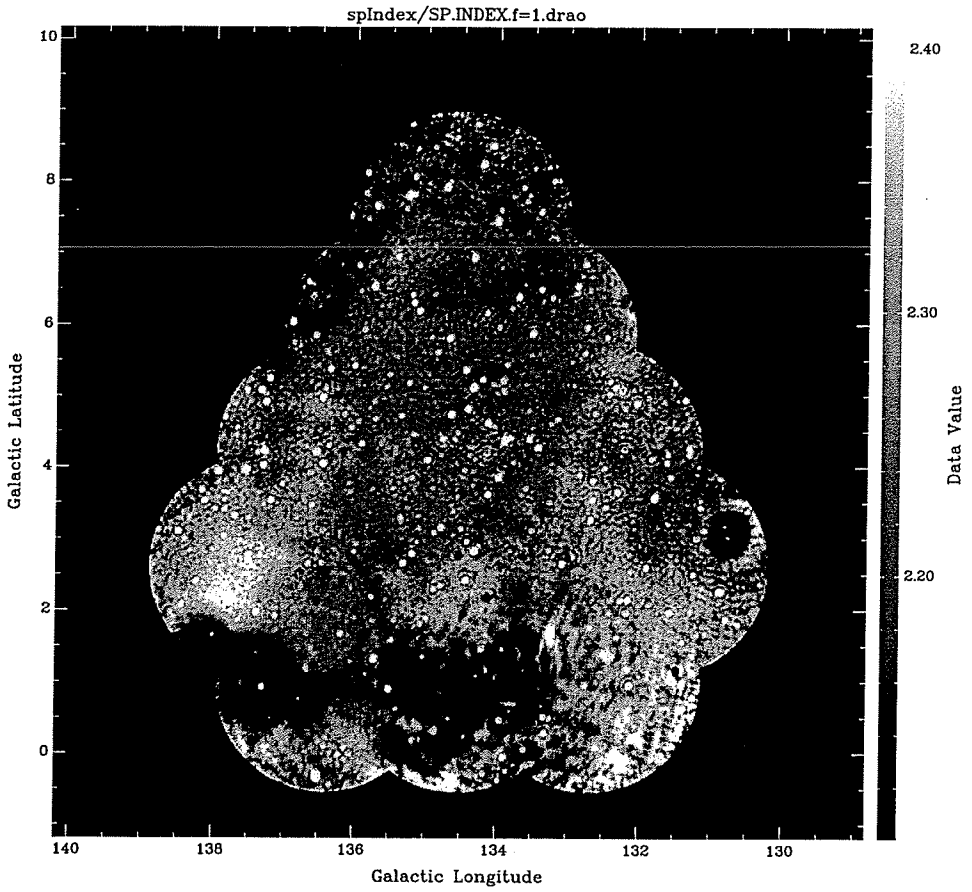

Figure 4-1: Temperature spectral index map after subtracting the irrelevant contributions to the detected emission. Steep, non-thermal values of β are shown white and flatter, thermal β values are shown as black. Note that the HII regions (i.e. W3/W4/W5) have an expected thermal temperature spectral index. Note also that the *egg* region is traced by a flatter (darker, blacker) temperature spectral index than the surrounding region. The latitude and longitude scales shown have units of degrees.

We considered adopting an offset value of +0.2 when discussing values of temperature spectral index from our map to correct for the difference of HB3 from previously published results. This would essentially be equivalent to using the map without the SSF removed. KRH83 provide evidence that the SSF is in fact a feature occurring in front of W4 and thus we argue its removal is necessary to distinguish between W4 and the foreground emission. Additionally the values of β from our map are consistent with expected values for thermal regions. Therefore, this offset is not adopted, but it is, at times, considered when discussing the results.

4.1.2.2 Features of the temperature spectral index map

The following are notable features of the spectral index map (Figure 4-1). The values of β given have been determined by visual inspection:

1. The regions immediately surrounding W3/W4/W5 exhibit a thermal spectral index ($\beta \approx 1.9$). The supernova remnant, HB3 has a steeper, synchrotron spectral index ($\beta \approx 2.3$ to 2.4).
2. A flatter temperature spectral index ($\beta \approx 2.1$ to 2.3) is evident over much of the region defined by the *egg* (Figure 3-20) as compared to the "exterior" region outside the *egg* (but which is not obviously part of W3/W4/W5 or HB3). The exterior region has $\beta > 2.3$ which is consistent with diffuse synchrotron emission.

3. The higher longitude "wall" of the chimney ($l \approx 136°$) exhibits a spectral index gradient. It has a thermal spectral index at low latitudes and gradually steepens by about 0.1 from $\beta \approx 2.1$ to $\beta \approx 2.2$. The lower longitude "wall" ($l \approx 133.5°$) exhibits a sharper profile, abruptly changing spectral index by ~0.1 at $b \approx 2.2°$.
4. There is a roughly horizontal band of flatter temperature spectral index of $\beta \approx 2.1$ at $b \approx 3°$ which runs between the walls and separates two steeper regions above and below. The difference between the flat region and the steeper regions is $\geq$~0.1. The region below this band is especially steep ($\beta \approx 2.3$).
5. At high latitudes ($b > 6.5°$) the spectral index is flat ($\beta \approx 2.1$) over most of the region including the chimney with the exception of a local steepening to $\beta \approx 2.3$ in a roughly elliptical region centred at ~(135.5°, 7°) with a position angle ~45° and with dimensions ~1° × 0.7° which is coincident with the "wishbone" (see Figure 5-7).
6. The steepest extended regions (not including the point sources) on the image are directly above W5 at $l \approx 137.5°$ running from $b \approx 1.5°$ to $b \approx 3°$ with $\beta \approx 2.4$ and several small steep regions below W4 and some west of HB3 near the bottom of the image. These small regions have $\beta \geq 2.5$.

The fact that the temperature spectral index map traces the region of the *egg* is supportive of the idea that the region is associated and a single coherent structure. The spectral index within the structure is not very steep which according to Lisenfeld & Völk (2000), rules out diffusion transport of CRs. The flatter spectral index, i.e. $\beta \approx 2.3$, indicates that convection is possibly occurring and that energy losses due to synchrotron radiation are

not significant. Note that even with the offset of 0.2 added, the temperature spectral index is less than 2.6 which is still flat enough to suggest a convection model.

The additional spectral index features noted here will be discussed further in Chapter 5 in the context of the other data.

4.2 Magnetic field of the egg-shaped structure

Basu et al. (BJM99) propose a swept up magnetic field, tangential to the shell, is present in the W4 chimney/superbubble that potentially has a stabilizing effect on the structure. If the field is predominantly in a direction along the shell, then it should have only a small component along the line of sight. An examination of the rotation measure will give us the line of sight component of the magnetic field that may help reveal some of the magnetic field of the structure.

If one can determine both the rotation measure and the electron density in a region, one may use Eq. (2-32) to determine the line of sight component of the magnetic field in that region. The absolute Hα flux measurements presented by Dennison et al. (DTS97) provide a means for computing the electron density in the region.

Assuming that one observes a limb brightened shell, with the front and back "skin" of the shell of comparable electron density to the observed edges, one may find the electron density in the edges of the shell and then derive the electron density at the front and back of the shell using geometrical considerations. This "skin" of electrons acts as a Faraday rotator to the background polarized radiation.

Although the Faraday rotation along the limbs of the *egg* are severe enough to nearly completely depolarize the region, the projected centre of the *egg* is still somewhat polarized since there is less path length through the rotating medium. Thus the rotation

measure will be determined for the polarized emission in the projected centre of the *egg* and also for polarized emission with lines of sight not passing through the *egg*. By comparing these it may be possible to estimate the amount of rotation due to the *egg*'s skin and using Eq. (2-32) the magnetic field in its shell may be determined.

4.2.1 Calculating the electron density in the eggshell

DTS97 determined absolute Hα fluxes for the shell in units of Rayleigh; where 1 Rayleigh [R] is defined as $10^6/4\pi$ photons cm^{-2} s^{-1} sr^{-1}. From the Hα fluxes and some assumptions about geometry, one may determine an electron density in the shell.

DTS97 assume a spherical geometry for a shell with a radius, r. They define a shell thickness, s, and determine a radius to thickness ratio, r/s = 12. This is reasonable since the wall thickness is between 0.25° and 0.5° and the total height of the shell is ~6.5°. Taking half of the height to be equal to the radius and a thickness of 0.3°, one finds a ratio, 3.25/0.3 ≈ 11. A shell thickness of 0.27° would give a ratio of 12. At a distance of 2.3 kpc (Normandeau 2000) a shell thickness of between 0.25° and 0.5° corresponds to a physical size between 10 pc and 20 pc.

Using the spherical geometry assumed by DTS97, it can be determined that

$$EM_S = EM_\perp \sqrt{1+\frac{2r}{s}} \qquad (4\text{-}5)$$

(DTS97), where EM_S is the emission measure in the shell as seen along the line of sight and $EM_\perp$ is the emission measure perpendicular to the shell. In Hα, emission measure is defined as the square of the electron density, n_e, integrated over the path length, l

$$EM = \int_0^l n_e^2 dl . \qquad (4\text{-}6)$$

If $r/s = 12$, using Eq. (4-5) DTS97 find

$$EM_S \approx 5 EM_\perp . \qquad (4\text{-}7)$$

And from Eq. (4-6)

$$EM_\perp = n_e^2 s . \qquad (4\text{-}8)$$

Assuming a temperature of 10^4K, which is the temperature expected in warm ionized gas regions, 1 R is equivalent to an emission measure, $EM = 2.8$ pc cm^{-6}. Using this, EM_S can be found from DTS97's Hα flux measurements. Then using Eqs. (4-7) and (4-8) the flux measurements may be converted to electron densities. The Hα flux was measured at four locations in the shell labeled H, I, J and K (Figure 4-2). Table 4-2 gives these values and

the corresponding electron densities that have been calculated for the shell and for our line of sight towards the shell.

4.2.2 Computing the rotation measure

Recall from section 2.2.5 that rotation measure (RM) may be computed from Eq. (2-34) which we remind the reader is

$$\psi = \psi_0 + RM \cdot \lambda^2 \qquad (4\text{-}9)$$

where ψ_0 is the intrinsic angle, RM is the rotation measure and λ is the wavelength of observation. The form of Eq. (4-9) is that of a linear function of ψ vs λ^2 with a slope equal to RM. Eq. (4-9) may be used if one has Stokes Q and Stokes U observations at several different frequencies.

Since the polarization data from the Dominion Radio Astrophysical Observatory is acquired in four separate 7.5 MHz bands (plus a 5 MHz gap at the H-spectral line; see Chapter 3), it is possible to plot ψ vs λ^2 and obtain a value for the rotation measure for every pixel in the image. The Stokes Q and U images are typically examined (and used to create polarized intensity and polarization angle images) with the four bands merged. However, to create the rotation measure map, the images from the individual bands,

Location	Hα flux [R] (DTS97)	EM_S [pc cm^{-2}]	EM_L [pc cm^{-2}]	n_e [cm^{-3}] (s = 10 pc)	n_e [cm^{-3}] (s = 20 pc)
H	6.7	18.76	3.75	0.61	0.43
I	0.7	1.96	0.39	0.20	0.14
J	2.7	7.56	1.51	0.39	0.27
K	5.8	16.24	3.25	0.57	0.40
Average	4 ± 3	11 ± 7	2.2 ± 1.5	0.44 ± 0.19	0.31 ± 0.13

Table 4-2: Electron density calculation.

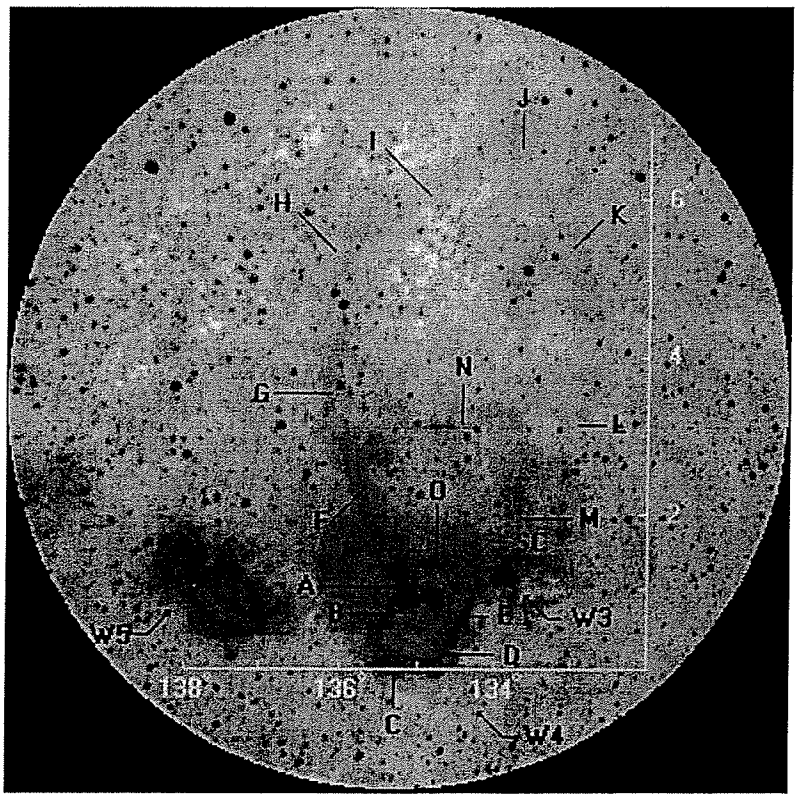

Figure 4-2: Hα image and labels reproduced with permission from DTS97. The electron density was computed at points H, I, J, and K.

labeled A, B, C and D, for both Stokes Q and Stokes U are required (8 images). At each wavelength the polarization angle, ψ must be obtained.

We use Brown's (2002) method for "unwrapping" the polarization angles (see section 2.2.5). The RM is evaluated for each pixel of the image using the procedure of calculating the polarization angle for each band and performing a least squares fit to the resulting values as described in section 2.2.5.

4.2.2.1 Confidence in the RM values

Reliable values of RM may only be obtained for pixels that are sufficiently polarized and for which a sufficiently confident least squares fit may be obtained. Thus some criteria are needed to eliminate unreliable pixels before the RM map may be examined.

The polarized intensity for each pixel was computed from Q and U maps which were convolved to a resolution of 5' (see Figure 3-9). Pixels with a polarized intensity less than the 5σ value of 0.05 K (see section 3.2.3) were flagged and RMs for those pixels are not included in the final map.

Secondly, the linear correlation coefficient, r, was computed for each fit of $\psi(\lambda^2)$ vs λ^2. The linear correlation coefficient is a means to measure the probability that a linear relationship exists between two variables. For N = 4 points, r is given by:

$$r = \frac{N\sum \lambda_n^2 \psi_n - \sum \lambda_n^2 \sum \psi_n}{\sqrt{N\sum \left(\lambda_n^2\right)^2 - \left(\sum \lambda_n^2\right)^2} - \sqrt{N\sum \psi_n^2 - \left(\sum \psi_n\right)^2}} \quad (4\text{-}10)$$

(Bevington & Robinson 1992). This coefficient is calculated for each least squares fit for each pixel. Pixels with $r < 0.9$ (i.e. the probability of linear correlation is 90%) are also flagged and the RM for these pixels are not considered.

The RM was calculated for each pixel according to Eq. (2-46). After computing a complete map, pixels not meeting the above criteria were set to zero. An averaged map was then computed by dividing the map into a grid of small, square boxes measuring 5.3' × 5.3' and finding the average value of pixels contained in each box, excluding pixels with a value of zero. An annotation file for the Karma image analysis tool was then produced to graphically display the map (see Figure 4-3). These computations were done using a set of locally developed plugins for the image analysis software, ImageJ (see Appendix 2).

4.2.3 The rotation measure map

Figure 4-3 (see also Figure 4-4 and Figure 4-5) presents a graphical representation of the rotation measure map that uses square and circle symbols of different sizes overlaid on the polarized intensity map. The squares, coloured yellow, represent a negative sign of the rotation measure while the circles, coloured blue, indicate rotation measure with a positive sign. From Eq. (2-32) it can be seen that the direction of the magnetic field will

determine the sign of the rotation measure as electron density is a scalar quantity and path length is defined to be positive in a direction from the source to the receiver. This results in a positive rotation measure when the line of sight component of the magnetic field is directed *towards* the observer. Conversely, a negative rotation measure will result when the line of sight component of the magnetic field is directed *away* from the observer.

We wish to determine an expected value for the rotation measure in the extended emission of the ambient Galactic medium and distinguish this from the W4 chimney candidate. Since the RM varies across extended regions, rotation measure histograms were produced for 1.3° × 1.3° regions on the image. Regions of this size were chosen because the RM seems to vary from positive to negative over regions of this scale (see Figure 4-3). Since the rotation measure map values were obtained by averaging square boxes measuring 5.3' × 5.3' (see section 4.2.2.1), each 1.3° × 1.3° region contains 225 RM measurements which gives statistically significant counts given a chosen bin size of 32 rad/m^2. The histograms show how the rotation measure varies in the region and to compare the values, the mean, mode, and standard deviations were computed in each region (see Table 4-3).

Regions 1 and 2 in Figure 4-6 are positioned in the projected central region of the *egg*. Region 10 is positioned over a portion of the *egg*'s "shell" (*eggshell*) which has sufficient polarized intensity according to the criteria in section 4.2.2.1 for computing a reliable RM.

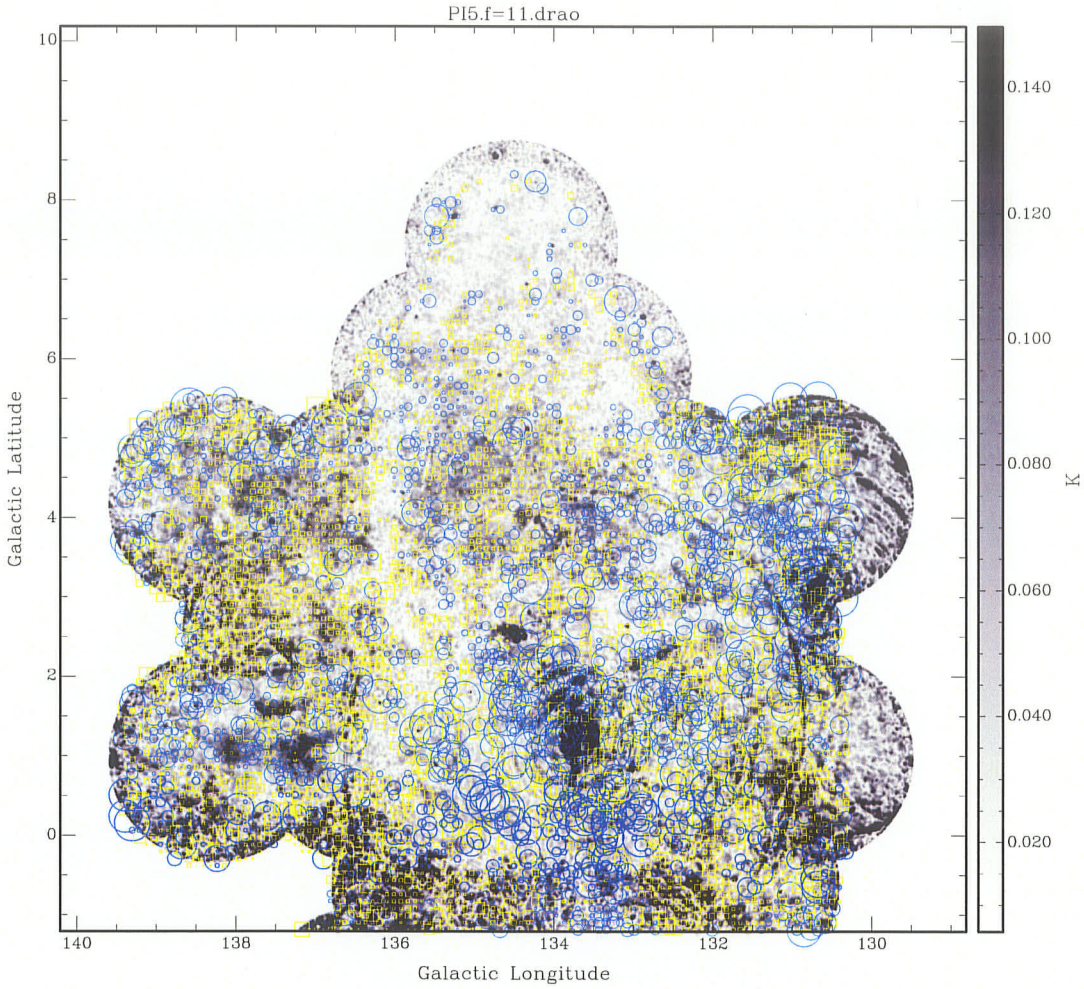

Figure 4-3: Rotation Measure map. Grey scale is polarized intensity convolved to a resolution of 5' and which has been inverted so that high intensity shows black while low intensity regions show white. Yellow squares indicate negative rotation measures and blue circles indicate positive rotation measures. The sizes of the squares and circles are proportional to the magnitude of the RM. The latitude and longitude scales shown have units of degrees.

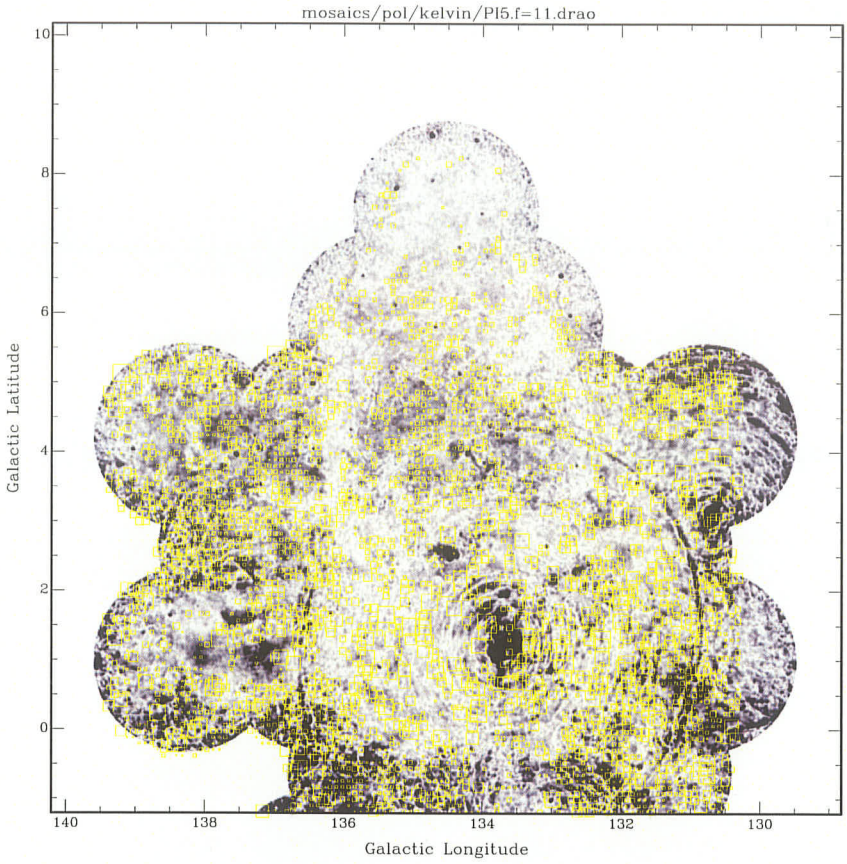

Figure 4-4: Map showing only negative RMs. Grey scale as in Figure 4-3.

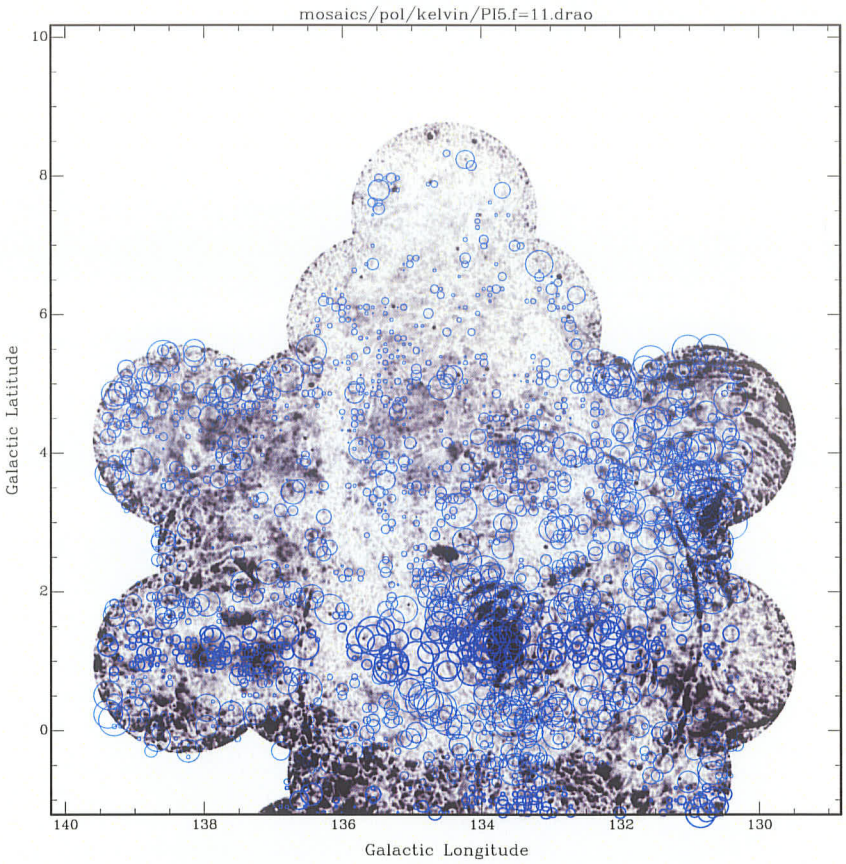

Figure 4-5: Map showing only positive RMs. Grey scale as in Figure 4-3.

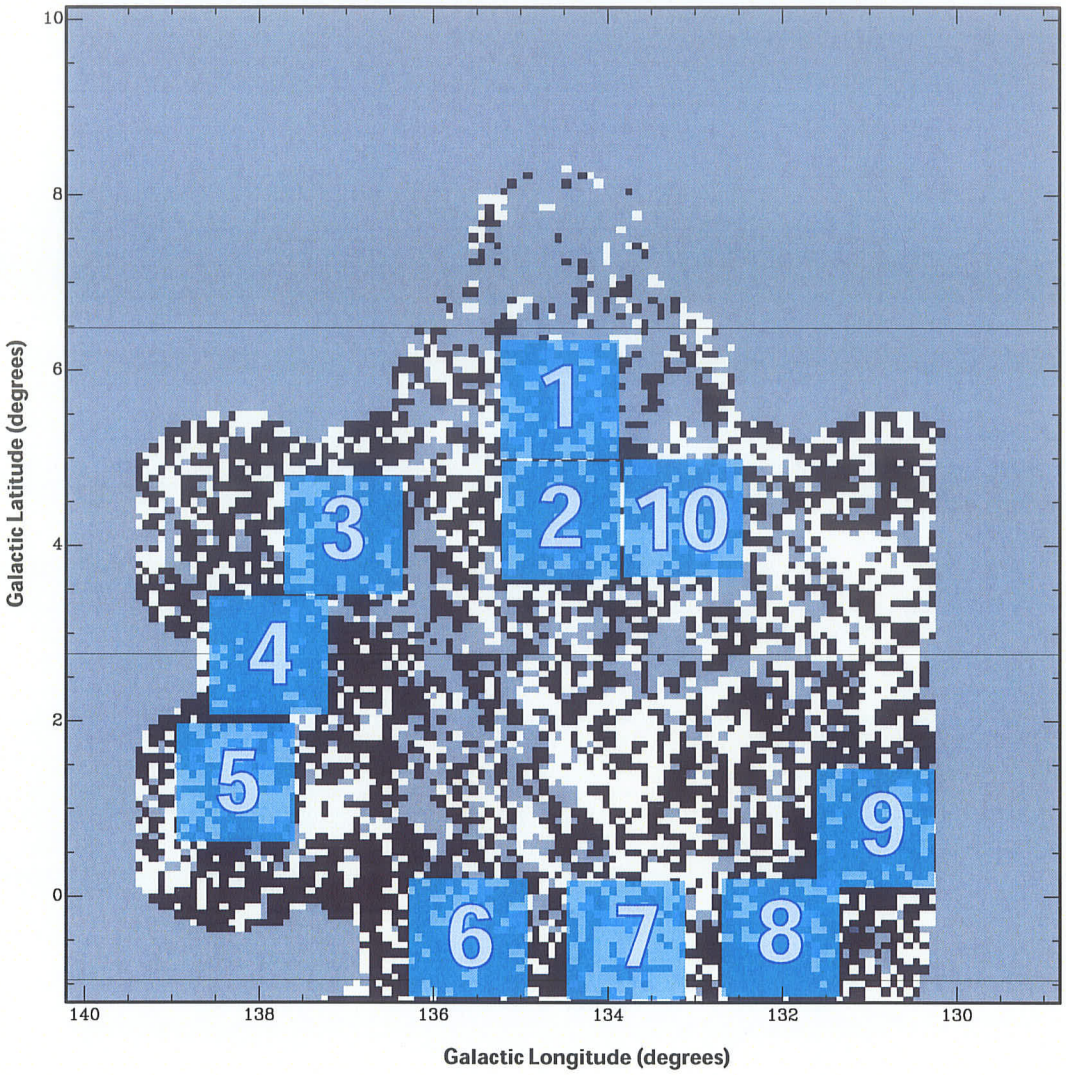

Figure 4-6: Histograms were made for each of the ten 1.3° × 1.3° square regions shown here labeled 1 through 10. The regions are overlaid on a binary rotation measure map; that is, regions of positive RM are shown white and regions of negative RM are shown black. RMs were not calculated for the grey regions due to the low polarized intensity in those regions (see section 4.2.2.1).

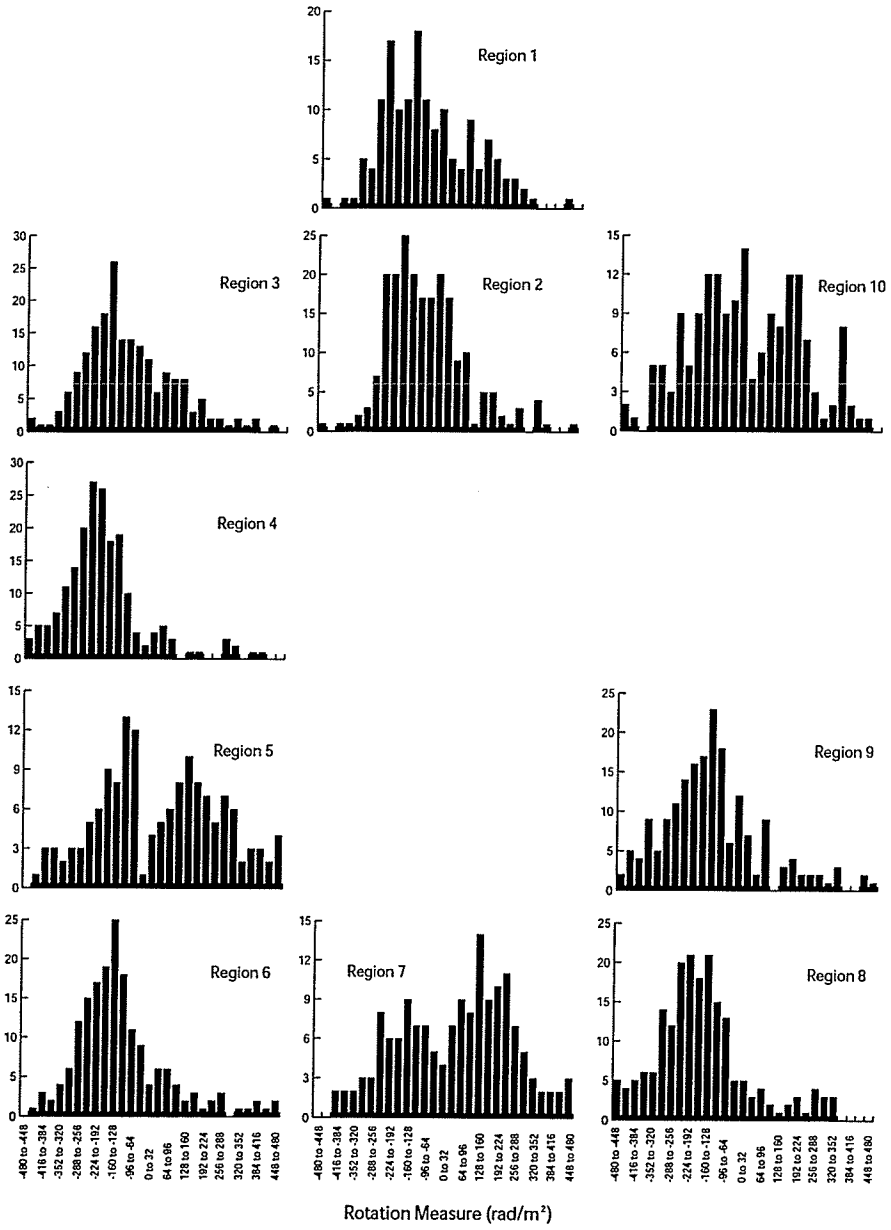

Figure 4-7: Histogram plots of the regions illustrated in Figure 4-6. The arrangement of the plots is similar to the layout of the regions on the image. The bins are the same for all plots having a range of 32 rad/m^2 per bin and shown for the bottom three plots. Note that the bin from –32 rad/m^2 to 0 has been excluded in these plots because that bin contains the points that have been set to zero. Thus it is dominated by the null values and distracting when visually examining the plots. Also note that the exclusion of this bin does not affect the statistics listed in Table 4-3 because for the computations, only zero values were excluded (and not all values in the bin).

Region	Mode RM (rad/m^2)	Mean RM (rad/m^2)	Standard Deviation
1	-236.7	-90.4	169
2	-184.5	-96.7	158
3	-178.7	-108.5	173
4	-200.2	-197.8	158
5 (-ve RM)	-91.3	-182.4	109
5 (+ve RM)	78.4	211.5	122
6	-127.6	-107.8	177
7 (-ve RM)	-245.6	-171.8	101
7 (+ve RM)	171.7	205.0	120
8	-151.1	-155.0	184
9	-212.3	-129.7	185
10 (-ve RM)	-154.7	-171.6	111
10 (+ve RM)	153.1	175.0	102

Table 4-3: Statistics for the RM histograms of Figure 4-7. Regions 5, 7 and 10 exhibit double peaked histograms (see Figure 4-7) and so statistics have computed on the peaks separately; that is, separate statistics have been preformed for RMs below and above zero.

Not all of the remaining regions chosen for the histogram plots are good comparison regions. This is because some of those regions are positioned over known features in the Galaxy and thus are not good representative regions of ambient Galactic emission. In particular, Region 5 is positioned over W5 that is described by Gray et al. (1999) as being a "polarized lens", that is a region of smoothly varying polarization angle. Region 7 is almost directly below W3 which being the most intense source of the W3/W4/W5 complex, may contribute to this region not being a good representative of the ambient Galaxy. It should be noted that these regions both exhibit a double peaked histogram. It may be that the negative RM peak is representative of the ambient Galaxy, while the positive RM peak is more representative of the RM due to the regions (i.e. W5 and W3) themselves.

The histograms for the remaining regions, 3, 4, 6, 8, and 9 all have a similar general shape, with a single negative RM peak and a Poisson-like distribution. Table 4-4 summarizes the statistics of these regions for easier comparison. The mode values for these regions range from –127.6 rad/m^2 to –212.3 rad/m^2 and the mean values range from –107.8 rad/m^2 to –197.8 rad/m^2.

Region	~l (°)	~b (°)	Mode RM (rad/m^2)	Mean RM (rad/m^2)	Standard Deviation
3	137	4	-178.7	-108.5	173
4	138	2.75	-200.2	-197.8	158
6	135.5	-0.5	-127.6	-107.8	177
8	132	-0.5	-151.1	-155.0	184
9	131	0.75	-212.3	-129.7	185

Table 4-4: Summary of statistics for regions that are good candidates for being considered as representing the ambient Galactic medium.

The histograms for Regions 1 and 2 have a different general shape when compared with the histograms of the regions listed in Table 4-4. Although they too have a single negative RM peak, the peak appears to be broader and skewed more towards the positive RMs. The modes in these regions of -236.7 rad/m^2 and -184.5 rad/m^2 are not significantly different that those listed in Table 4-4. However the means in these regions of –90.4 rad/m^2 and –96.7 rad/m^2 are smaller than any of those in Table 4-4. This suggests that perhaps these regions have a contribution from the ambient Galactic medium which produces the peak of the distribution, but it is the rotation occurring in the *eggshell* which is causing the distribution to be skewed.

In an attempt to determine the RM contribution of the *egg*, we compare the means of the regions listed in Table 4-4 with the means of Regions 1 and 2. We estimate that the contribution of the *eggshell* is ~+45 rad/m^2. That is, ambient radiation which would otherwise exhibit a RM of ~-140 rad/m^2 if not passing through the *eggshell* instead exhibits an average RM of ~-95 rad/m^2 due to rotation from the ionized gas and magnetic field in the *eggshell*. The error on this value is estimated to be ~35 rad/m^2 based on the spread in values of Table 4-4.

~*l* (°)	~*b* (°)	Mean RM (rad/m^2)	Error
136.5	4.53	-79	71
135.5	1.57	-293	237
134.5	-0.84	-101	20
133.5	1.73	-243	57

Table 4-5: Point source RM data averaged into 1 degree bins (Brown 2002).

Brown (2002) computed RMs for point sources in the CGPS survey and gives averaged values for 1° bins. Table 4-5 lists the values she gives that are relevant for comparison with our data. The data are consistent within error. Uyaniker et al (2003) compared histograms of RMs of compact sources versus extended emission and found a greater spread apparent in the RM of the compact sources. These data, although limited in scope, are consistent with this conclusion since the spread in the mean values of the RMs of the point sources in Table 4-5 is significantly larger than the spread in the values of the RMs of the extended emission in Table 4-4.

4.2.4 Calculating the magnetic field

Recall Eq. (2-32) can be rearranged to give

$$B_{//} = \frac{RM}{Kn_e l} \qquad (4\text{-}11)$$

where $B_{//}$ is the line of sight component of the magnetic field, RM is the rotation measure, K is a constant equaling 0.812 $\mu G^{-1} cm^{-3} pc^{-1}$, n_e is the electron density, and l is the distance through which the radiation is being rotated. Values for RM, n_e, and l have been determined and thus a value for $B_{//}$ may be calculated.

In section 4.2.1 the electron density for the *eggshell* was calculated to be 0.44 ± 0.19 cm^{-3} for 10 pc thick walls 0.31 ± 0.13 cm^{-3} for 20 pc thick walls. In section 4.2.3 the rotation measure due to these walls with the assumed ambient contribution removed was estimated to be $+45 \pm 35$ rad/m^2. Using Eq. (4-11) we find $B_{//} = 9 \pm 8$ μG for 20 pc thick walls and $B_{//} = 13 \pm 11$ μG for 10 pc thick walls and in a direction that is *towards* the observer.

Beck (2001) and references therein give the total field strength of the local Galaxy as being 6 ± 2 μG, decreasing to ~5 μG for a Galactocentric radius of 11 kpc which is the approximate distance of the W4 region. The uniform component of the magnetic field is 2 to 4 μG. Brown (2002) and references therein give a local field strength of ~2.2 μG.

The values of the *egg*'s field agrees with the estimated ambient magnetic field to within the error. However, the error is substantial and if we compare our best estimates of the line of sight magnetic field (i.e. 9 μG and 13 μG) to the ambient field the suggestion is that the *egg* may have a slightly greater magnetic field than the surrounding ambient medium. If our assumed contribution to the RM by the ambient medium is low, resulting in a high estimate of the RM due to the *egg*, then our calculated line of sight magnetic field decreases to a value that is within the ranges presented by Beck (2001) and Brown (2002).

Recall from section 1.2 that the "v" shaped HI filament observed by Normandeau (1996) has a velocity signature that suggests it is moving towards the observer. This suggests that the *egg* as a whole may be tilted towards the observer. Since the orientation of the line of sight component of the magnetic field due to the *egg* is also likely towards the observer, there is support for Basu et al.'s (BJM99) prediction of a tangentially oriented magnetic field, but of which only a small line of sight component is observed.

5: Discussion and Conclusions

The W4 region is presented as an object that is in an evolutionary stage between that of a superbubble and a chimney. In section 5.1.1, the discussion focuses on the morphology of the region in the various datasets. Timescales and formation scenarios presented in the literature and the ways in which our observations support or refute these theories are discussed in section 5.1.2. In addition, in section 5.1.3 we attempt to assess the likelihood that this region provides a mechanism for ionizing radiation to escape to the Galactic halo.

Sections 5.1.4 and 5.1.5 discuss other interesting features in our data which are not likely related to the *egg* region.

5.1 Discussion

The W4 star forming complex has features of Norman & Ikeuchi's (1989) conventional chimney model, a broken HI shell allowing cosmic rays and UV photons to escape to higher latitudes. The contrasting opinion of Dennison et al. (DTS97) is that W4 is an "apparently closed superbubble", a complete shell of HI with an inner layer of ionized gas, which is trapping the UV photons and cosmic rays being produced by the star cluster, OCl 352. Theoretically, superbubbles evolve to become chimneys and are thus

considered to be at an earlier evolutionary stage than chimneys. As a superbubble expands, it will eventually reach a point where it fragments and bursts resulting in a chimney (de Avillez & Berry 2001 and references therein).

The radio continuum and polarization data supports the intermediate picture lying between the two extremes of superbubble and chimney. The *egg* morphology of the W4 region appears to be a superbubble which is in the process of fragmenting but which has not yet reached the chimney stage. Dennison et al. (DTS97) suggest that an earlier epoch of star formation in a molecular cloud complex south of W4 may have contributed to the formation of the W4 *egg*, but note that the remarkable alignment of OCl 352 with the bubble shape suggest that OCl 352 is the dominant contributer. We support the suggestion that OCl 352 is the dominant source of ionizing radiation for the *egg* but that it is not solely responsible for the creation and evolution of the structure. Additionally, we postulate that there is little matter remaining interior to the upper portion of the *egg* and that any gas or cosmic rays that may have existed at an earlier stage of the superbubble's existence have escaped through apparent breaks in the *egg*'s structure. This theory is supported by morphological evidence and by the temperature spectral index map.

Evidence supporting the picture of a superbubble in a later stage of evolution as it has begun to fragment is outlined in this chapter. The literature suggesting two or more stages of star formation have occurred in the region is reviewed and the ways in which our observations support this scenario are outlined. In addition, in section 5.1.4, some

interesting polarization features that appear in the data and their possible relationship with the W4 superbubble are discussed.

5.1.1 Superbubble or chimney?

The data shows strong evidence of associated emission appearing as one contiguous structure beginning in the Galactic plane and extending up to a latitude of $b \sim 6.7°$. The evidence, including emission in the 1420 MHz, 408 MHz, Hα, and IRAS (60 μm) datasets, reveals a striking, continuous egg-shaped structure (see Figure 3-21). At our adopted distance of 2.3 kpc, the projected ellipse of the *egg* measures ~4° wide by ~5.5° high which is ~165 pc wide by ~225 pc high. At this height the top of the *egg* extends beyond the 1σ distance of the Gaussian HI distribution (135 pc) but not yet into the halo which begins to dominate at a height of ~500 pc (see section 1.1).

The polarization data is also consistent with a continuous structure since the depolarization observed by Gray et al. (1999) in the lower latitude data continuously traces up the "walls" of the *egg*. This is apparent in both Stokes Q and Stokes U and in the polarized intensity map (see Figure 3-7 to Figure 3-9).

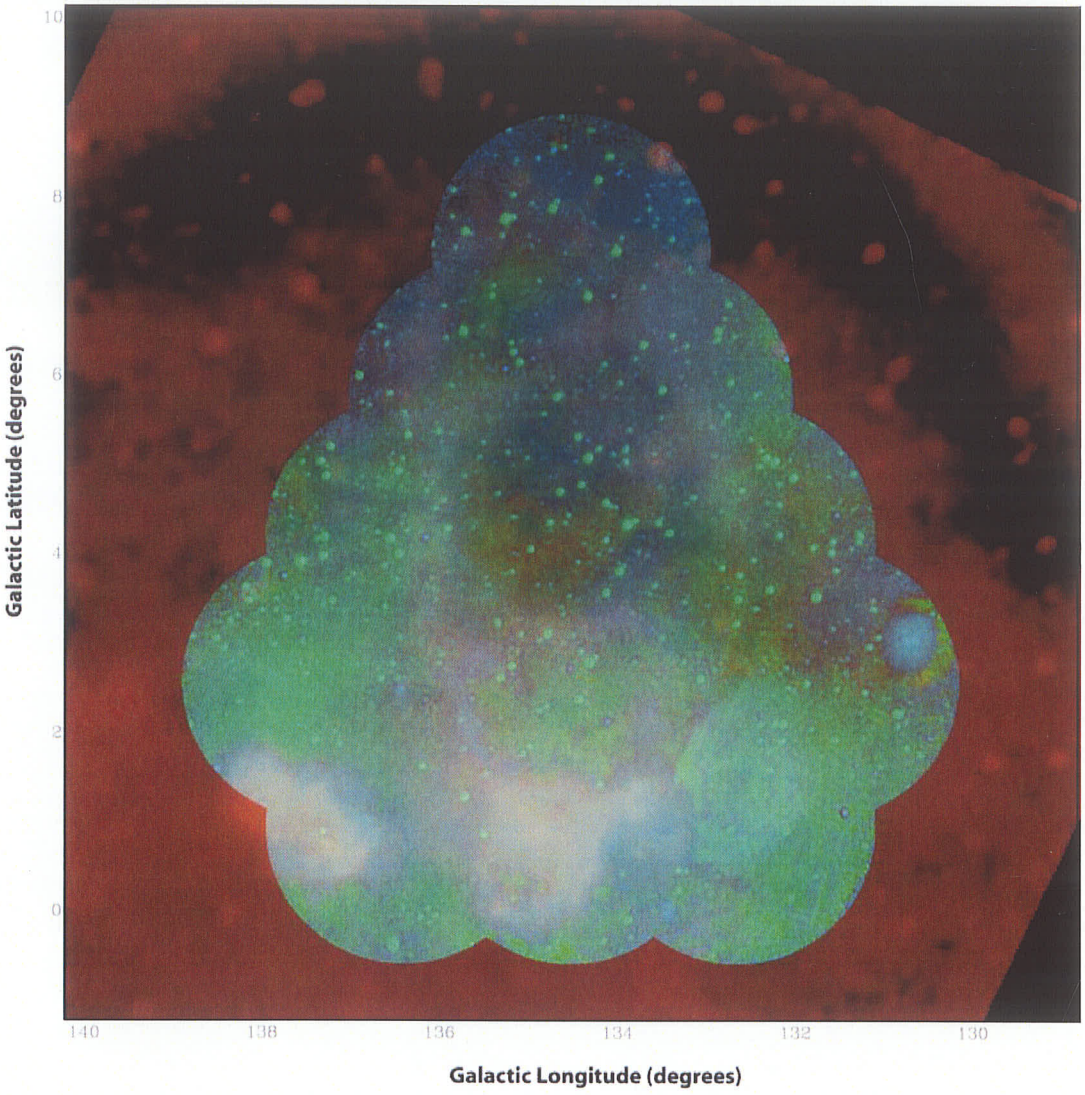

Figure 5-1: Spectral index map (coloured green) combined with the 1420 MHz and Hα datasets coloured as shown in Figures 3-12 and 3-14 respectively. The pink regions indicate a flatter, more thermal spectral index while the light green colour indicates steeper, synchrotron dominated regions. Note the approximately horizontal ridge of flatter (pink) spectral index at $b \approx 3°$ to 3.5°.

In polarization angle Gray et al. (1999) defined a "cell size" as the scale over which the polarization angle varies by 180°. The cells are visually apparent as a "mottling" of the image. They find the cells range in size from 1' near W4 to ~10' farther away to several tens of arcminutes elsewhere in the image. This small scale mottling is observed to follow the "walls" and it is coincident with the observed depolarization (Figure 3-10).

The continuous depolarization is strong evidence that the depolarizing emission is located at the same distance as W4. In addition, the outline of the egg shape is visible as a region of flatter temperature spectral index (see Figure 4-1). A colour image of the spectral index map combined with the 1420 MHz data and the Hα data (Figure 5-1) further illustrates this point.

The egg-shaped structure tapers at the top suggesting convergence or closure rather than having the "cone-like", divergent shape of the chimney models (Norman & Ikeuchi 1989). The 1420 MHz and Hα definitely show this converging top and to lesser degree, so does the 408 MHz data.

Although, the data suggests the *egg* has a top, the shape does not have a uniform intensity around the perimeter. There appear to be regions of lower intensity that suggest breaks in the continuous structure.

Two main breaks appear in the structure, one near the top of the *egg* (point 49, Figure 3-22 and Table 3-2) and one on the lower longitude side near $b = 4°$ (points 31 and 28,

Figure 3-22 and Table 3-2). By visually inspecting each individual image at 1420 MHz, 408 MHz and Hα, the centre coordinates and approximate widths for the two breaks were identified. These are summarized in Table 5-1.

	1420 MHz	408 MHz	Hα	~ width (°)	~ width (pc)
break at top	134.77°, 5.58°	134.12°, 5.82°	135.08°, 5.97°	0.5	20
break at side	133.47°, 4.36°	132.84°, 3.73°	133.56°, 4.15°	1.2	48

Table 5-1: Centre coordinates and approximate widths of "breaks" in the *egg* structure identified visually in the 1420 MHz, 408 MHz and Hα data. Widths in pc are computed using our adopted distance of 2.3 kpc.

The breaks seem to be different in character with respect to the temperature spectral index. Near the top break the temperature spectral index tends to be flatter ($\beta \approx 2.1$), i.e. more thermal, while at the side break the index steepens to $\beta \approx 2.2$ to 2.3 (see Figure 4-1 and Figure 5-1).

In addition to the breaks, there appears to be emission branching off the main *egg* structure which we have nicknamed the *fork* (see Figure 3-21 and Figure 5-2). A faint *arc* of emission extends up from this *fork* and appears to arc back to the *egg*. This *arc* of emission is coincident with the polarization *wishbone* (see Figure 3-21 and later discussion in this chapter).

The lower portion of the *fork* does exhibit similar depolarization as the lower portion of the wall, suggesting that the *fork* is associated with the *egg*'s emission. However it is

unclear whether the continuing *arc* of emission is associated with the *egg*. A hand tracing of the regions of higher emission including the *fork* and the apparent breaks are illustrated in Figure 5-2.

Having identified breaks in the structure one must ask, is anything escaping? Normandeau (2000) observed a vertical HI filament or "spur" extending from ~(134.15°, 6.083°) to ~(134.175, 7.25) and with a width ~0.25° (see Figure 1-2, Figure 3-17, Figure 3-19 and Figure 3-21). The filament appears in several velocity channels from v = -38.46 km/s to v = -45.05 km/s, velocities which are consistent with chimney velocities. Additionally at 408 MHz the filament appears directly above the apparent break in the superbubble and also at the higher longitude edge of the break at the top of the *egg* (Figure 5-2). This filament may be interpreted as being a portion of the *egg*'s "skin" (i.e. the *eggshell*) that is being pushed out as it breaks. It suggests that an outflow is taking or has taken place.

There is a distinctive region of very low intensity inside the *egg*'s walls and above $b \approx$ 3.5° (points 30, 32, 33, 35 and 40 in Figure 3-22 and Table 3-2). Figure 5-3 and Figure 5-4 show plots of the 1420 MHz data at fixed longitude (l = 134.68°) and fixed latitude (b = 4.011°) respectively. In both plots this region of very low emission (< 4.8 K) is evident; in Figure 5-3 the area runs from 3.5° < b < 4.8° and in Figure 5-4 the area extends from 134° < l < 135.5°. The region has lower emission than even the regions exterior to the *egg*.

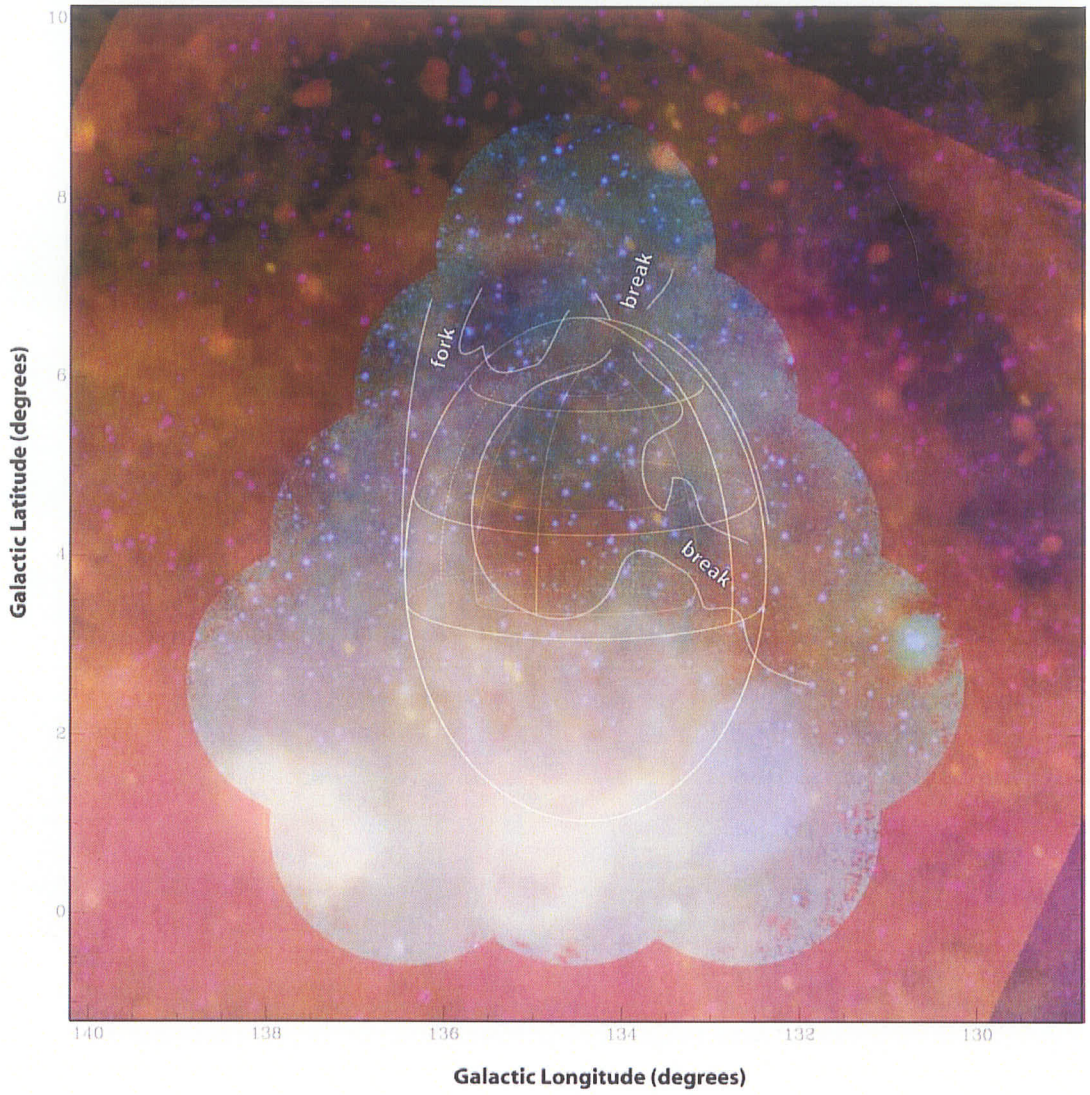

Figure 5-2: Colour image of Figure 3-20 (recall that it is a combination of 1420 MHz (turquoise), 408 MHz (purple), Hα (red), and 60 μm IRAS (yellow)) with the overlay of the *egg* and lines tracing the contours of higher emission. The *fork* and the two breaks discussed in the text are labeled.

This low emission region is most obvious at 1420 MHz but is also apparent in both 408 MHz and Hα. There does appear, however, to be 60 μm emission in this region from dust which one would reasonably expect to find in the foreground and along the line of sight.

The low emission implies either that the region is evacuated of gas that would emit at these wavelengths or that UV photons contained within are being absorbed by dust. In the former case, there is less column density along the lines of sight passing through this region and less intensity is observed.

In this low emission region, there are two horizontally oriented HI filaments positioned at $\sim b = 3.75°$ which were first identified by Normandeau (1996) (see Figure 1-2, Figure 3-17, Figure 3-19 and Figure 3-21). These suggest that the gas within the region below $b = 3.75°$ is in fact being "trapped".

Additionally, a *ridge* of Hα and 1420 MHz emission appears at $\sim b = 3°$ to 3.5° (points 21, 23 and 25 in Figure 3-22 and Table 3-2). The *ridge* at 1420 MHz is visible in Figure 5-2. Coincident with the 1420 MHz *ridge* is a flattening of the temperature spectral index (see section 4.1.2.2, discussion point #4 and Figure 5-1). Below this *ridge* but above point "O" (DTS97, Figure 4-2 or point 15 in Figure 3-22 and Table 3-2) the spectral index steepens, indicating a shift between these two features from thermal emission near both the *ridge* and point "O", to synchrotron emission. The synchrotron emission region appears to be surrounded by thermal emission, suggesting perhaps, that the synchrotron emitting electrons are trapped within.

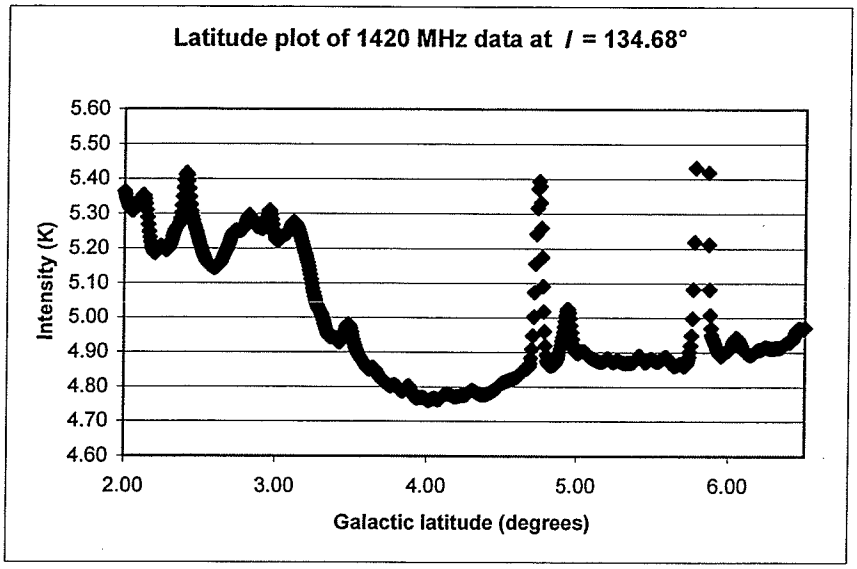

Figure 5-3: Plot of intensity vs Galactic latitude in the 1420 MHz data at a fixed longitude of 134.68°.

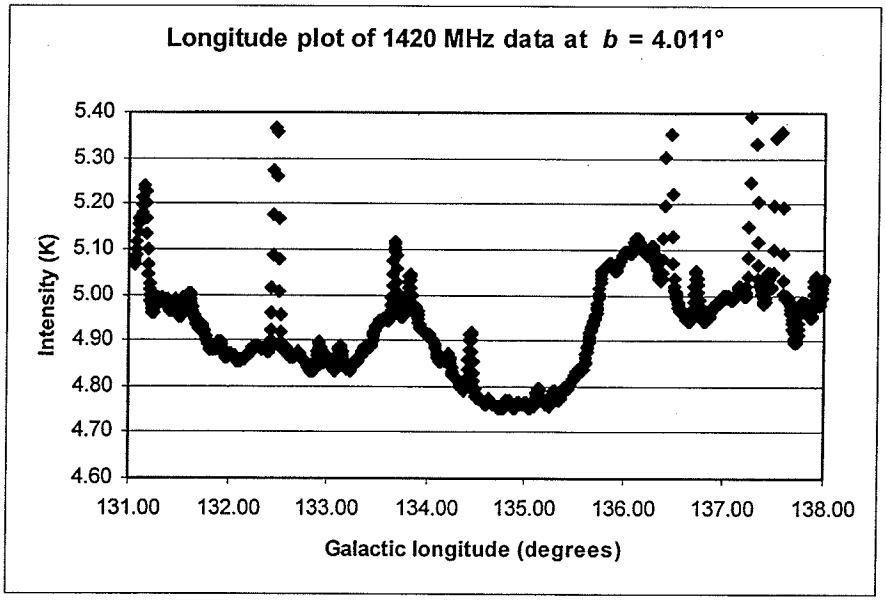

Figure 5-4: Plot of intensity vs Galactic longitude in the 1420 MHz data at a fixed latitude of 4.011°.

All this evidence supports the theory of a trapped lower region (i.e. south of $b = 3.75°$) with an evacuated region above (i.e. north of $b = 3.75°$). This trapped region is in addition to the trapped region below point "O" as discussed by DTS97.

5.1.2 Timescales and possible formation scenarios

Several authors have suggested that multiple epochs of star formation have occurred in the region (Lada et al. 1978, Thronson et al. 1980, Carpenter, Heyer & Snell 2000, Reynolds, Sterling & Haffner 2001) and DTS97 suggest that an earlier epoch of star formation may be responsible for the creation of the superbubble that we call the *egg*. Dennison et al. (DTS97) suggest that while an earlier generation of stars may not be directly responsible for creating the *egg*, it may have contributed by creating a region of reduced density due to the outflows from the stars which in turn allowed OCl 352 to form the egg shape in its relatively short 1.3-4.3 Myr lifetime.

Normandeau et al. (NTD96) calculate that the combined winds of the 9 O-type stars in the cluster could blow-out the region up to a height of 110 pc in 5.7 Myr which they say roughly agrees with cluster age estimates of 3.7-4.3 Myr.

In light of Hα evidence that the structure extends up to ~230 pc, DTS97 calculate that 6.4-9.6 Myr would be required to allow sufficient expansion. They cite cluster ages of 1.3-2.5 Myr, which are smaller than those cited by NTD96, and thus claim that OCl 352 cannot be solely responsible for the formation of the *egg*.

Reynolds, Sterling & Haffner (2001) state that numerical simulations of blowouts reaching heights of <1000 pc, as suggested by their observations of the large Hα loop, require times of 10-20 Myr. Thus they also suggest a multiple star forming epoch scenario to explain the observations.

Using a Kompaneets model (see section 1.2) on the superbubble Basu et al. (BJM99) find a best-fit age estimate of 2.5 Myr which is in agreement with age estimates for OCl 352. However, the model also predicts a scale height of H ~ 25 pc which is much less than the ~140 pc that was measured for the region by Normandeau (2000). The scale height evidence suggests that the model may not be appropriate. Additionally, if the multiple star forming epoch scenario is adopted, it is not necessary for the *egg* structure to have been formed on a timescale comparable to the age of OCl 352.

The morphological evidence supports the multiple star forming epoch scenario. Near the cluster there is relatively intense ~22 K emission. Around the cluster, but not symmetrically centred on the cluster is a small, 1° or ~40 pc loop visible in radio continuum, infrared, and Hα emission with shell-like structure. This loop does not have a constant limb brightness and is thus interpreted as having "broken out" in places. (Terebey et al. 2003)

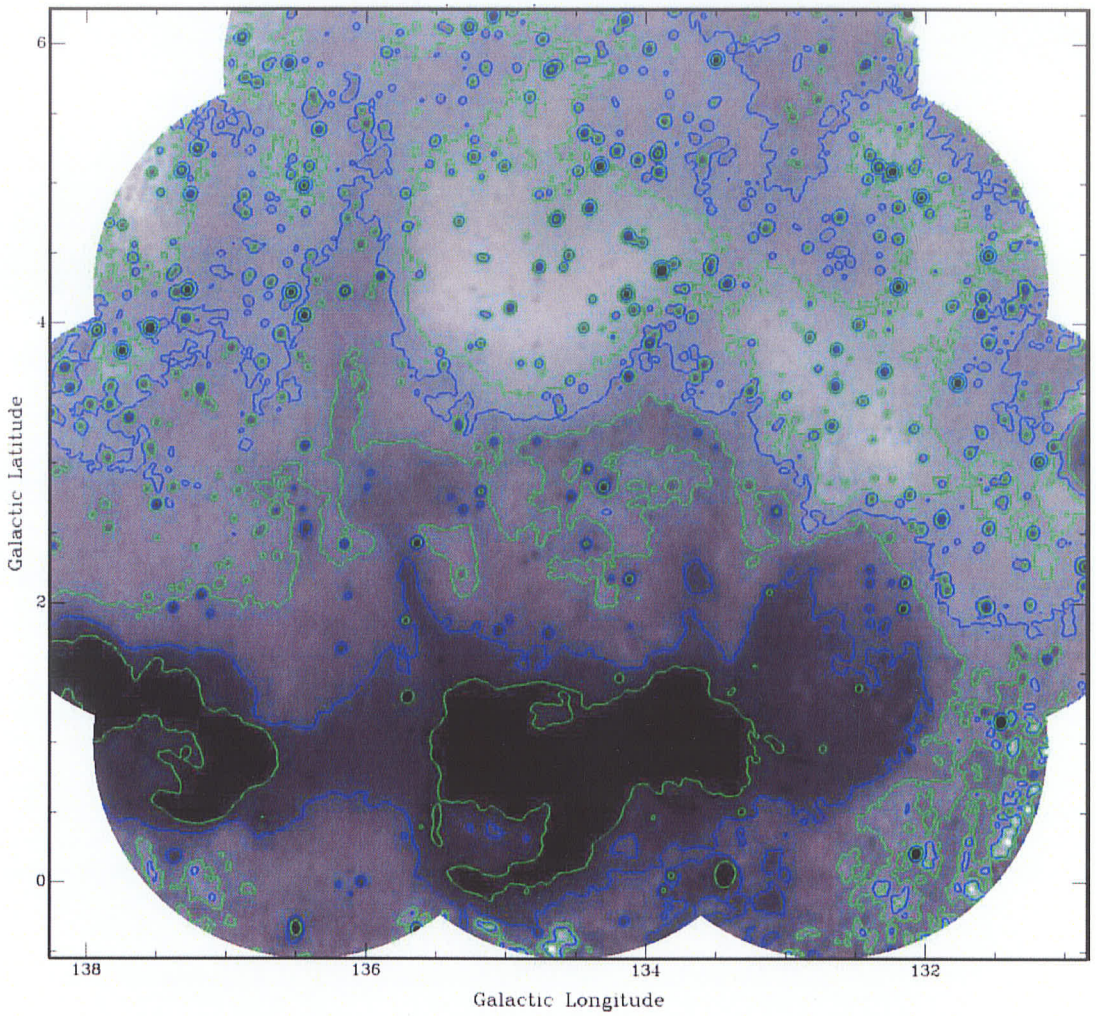

Figure 5-5: 1420 MHz image convolved to the resolution of the 408 MHz image shown log scaled and with inverted colours (i.e. black is high intensity). Green contours are at values of (starting nearest W4 and going up in latitude) 8.0 K, 5.2 K, and 4.9 K. Blue contours are set at values of 6.0 K and 5.0 K. Contour levels have been chosen to highlight the small "loop" (8.0 K green contour) and the "ridge" of emission (5.2 K green contour).

Above or approximately coincident with the top of the Terebey et al. (2003) loop is the Hα filament identified by DTS97 (point "O" in Figure 4-2) at b ~ 1.3° which is also apparent at 1420 MHz. A box from 134.94° > *l* > 134.45° and 1.41° > *b* > 1.29° over this filament has a mean value of 8.8 K. Above this filament the 1420 MHz intensity drops to ≤ 6 K. Between *b* ≈ 1.5° and b ≈ 3.2° the intensity only drops from ~6 K to ~5.2K after which one finds a *ridge* where the intensity drops quickly to ~4.75 K in the low emission region (see Figure 5-3 and Figure 5-4 and discussion in the previous section). Figure 5-5 shows a contour map highlighting these *ridges*. Further above this we find the upper limb of the *eggshell*. We postulate that this sequence of *ridges* may be the result of a series of star forming epochs in the region. Theoretical modeling is needed to test whether this postulate is physically reasonable.

5.1.3 The halo connection

Dennison et al. (DTS97) predict that the O-type stars in OCl 352 have a total output of ~2.3×10^{50} photons/s. Terebey et al. (2003) conclude that 40% ± 16 % (~9.2×10^{49} photons/s) of this ionizing radiation escapes to heights >60 pc. They suggest that these photons are available to contribute to ionizing the diffuse ionized gas and the upper Galactic halo. Our observations suggest that some of these photons are ionizing the gas in the upper portion of the *egg*.

Dennison et al. (DTS97) predict that the Hα surface brightness of the upper portion of the *eggshell* should be ≈20 R, which is well in excess of the 0.7 to 6.7 R that is actually

observed (see Table 4-2). They propose that two small molecular clouds located just above point "O" (Figure 4-2) are "shadowing" the upper portion of the shell, accounting for the low observed values of the emission measure. In contrast, Terebey et al. (2003) find that fewer photons than DTS97 predict are absorbed by the molecular clouds. A schematic diagram summarizing this picture is provided by Figure 5-6.

We adopt the Terebey et al. picture that 40% of the photons are escaping the lower loop and propose that some of these are ionizing the *eggshell* while others escape through the breaks in the *egg*'s structure. This hypothesis explains the observed deficiency in Hα intensity in the upper portions of the *egg*.

The average value of the observed Hα surface brightness for the four points, H through K in Figure 4-2 is 4 R (where R is Rayleighs, see section 4.2.1 for a definition). If we compare this to the predicted 20 R (DTS97) we find that ~20% (~1.8×10^{49} photons/s) of the photons escaping from the lower loop ionize the *eggshell* and the remaining ~80% of the lower loop's radiation escape through the breaks.

If a simple comparison of the sizes of the areas of the breaks is done, one finds the side break, having a width ~48 pc, has approximately 6 times the area of the top break, which has a width of ~20 pc (Table 5-1). Thus approximately 14% (~1.0×10^{49} photons/s) of the 80% of the photons escaping from the lower loop and not used for ionizing gas in the shell, can escape through the top break. The remaining 86% (of the 80%; i.e. ~6.3×10^{49} photons/s) may escape through the side break.

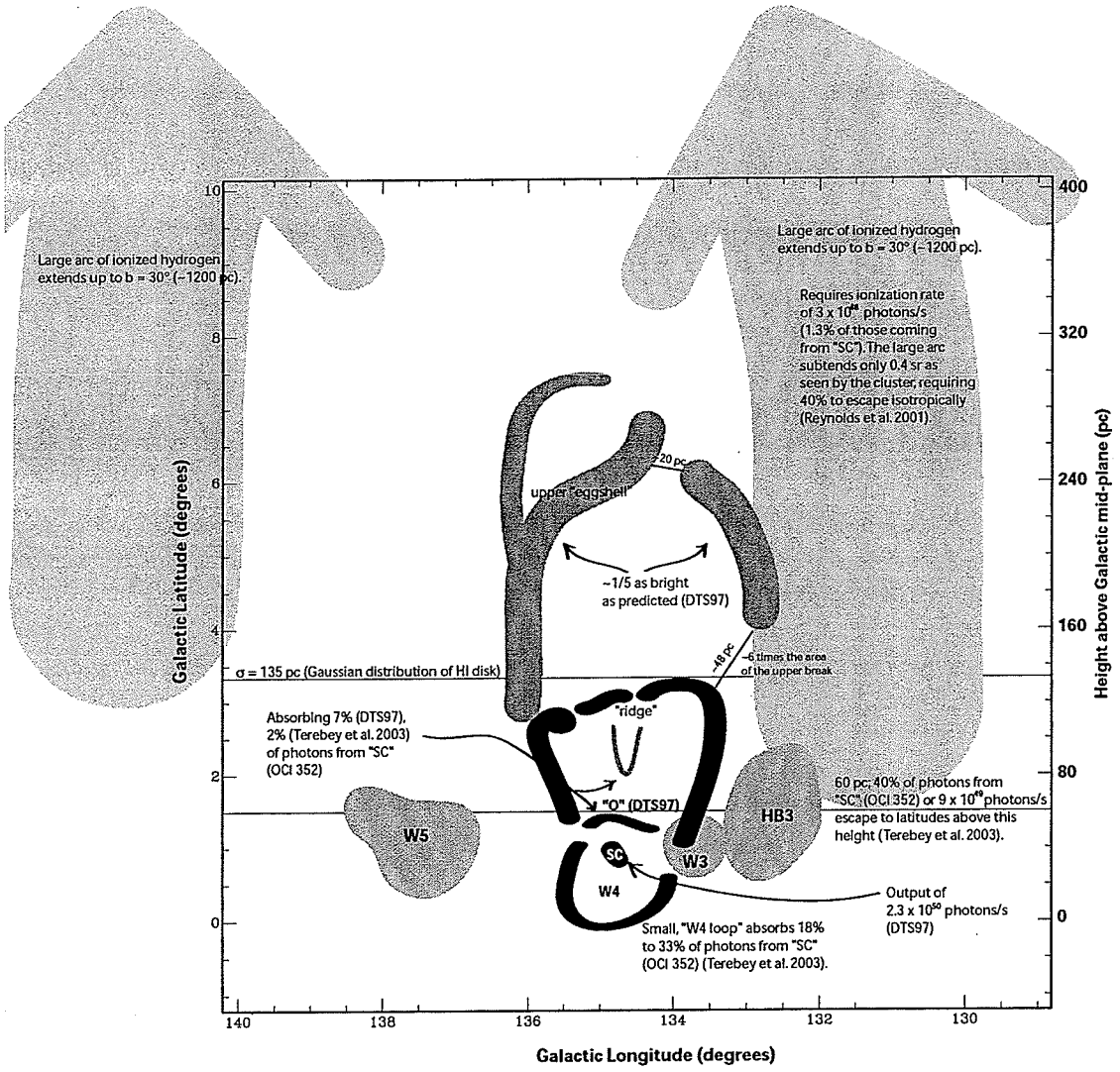

Figure 5-6: Schematic diagram summarizing the results of Dennison et al. (DTS97), Terebey et al. (2003) and Reynolds et al. (2001) regarding the number of ionizing photons that are able to escape into the Galactic halo. DTS97 predict that the upper shell should have an intensity of 20 R but it was observed to have ~1/5 this intensity.

In summary, the cluster produces of total flux of ~2.3×10^{50} photons/s, of which 40% (~9.2×10^{49} photons/s) escape the small loop (Terebey et al. 2003). Of the photons escaping the loop, ~20% (~1.8×10^{49} photons/s) are needed to produce the observed ionization in the upper shell of the *egg*; that is 8% of the *total* flux. This leaves 32% (~7.4×10^{49} photons/s) of the *total* flux that may escape through the breaks with 5% (~1.0×10^{49} photons/s) of the *total* photons produced by the cluster, escaping through the upper break.

Reynolds, Sterling, & Haffner (2001) estimate that the total hydrogen ionization rate for the large Hα loop observed in the WHAM data (Figure 1-4) is 3×10^{48} photons/s or ~1.3% of OCl 352's total output. However, given that the loop subtends ~0.4 sr as seen from the cluster, approximately 40% of the cluster's luminosity must escape if such escape is isotropic. Thus Terebey et al.'s (2003) prediction that 40% ± 16% of the cluster photons escape is consistent with the WHAM data. However, ~20% of these photons are required to produce the observed ionization in the upper *eggshell* as discussed above. Additionally, only 5% of the *total* cluster photons are predicted to escape through the top of the *egg*.

If the constraint that most of the photons escape through the break at the side of the *egg* is relaxed, then it is possible that enough photons would escape through the upper break to produce the observed ionization in the large Hα loop.

5.1.4 Polarization features

5.1.4.1 The wishbone

The aforementioned polarization *wishbone* is an unusual feature visible in both Stokes Q and Stokes U as well as the polarized intensity and polarization angle maps. This feature appears above the *egg* with approximate centre coordinates (134.9°, 7.1667°) (see Figure 5-7). The morphology of the object suggests a shell-like structure. A local steepening of the spectral index is observed interior to the polarization "shell" (see section 4.1.2.2 discussion point #5). Additionally, HI spectral line data reveal an almost shell-like structure (Figure 5-8) which is spatially coincident with the polarized emission over the velocities from v = -13.72 km/s to v = -30.21 km/s. The limb of this potential shell has an inconsistent brightness which may mean that it is not a shell at all, or it may be the result of confusing emission along the line of sight.

If the HI is associated with the polarized feature, the kinematic distance to the HI would suggest that the object is ~1.2 ± 0.2 kpc away (Brand & Blitz 1993). This is much closer than the estimated 2.3 kpc distance to W4 and would suggest that this is a foreground object, not associated with the *egg*.

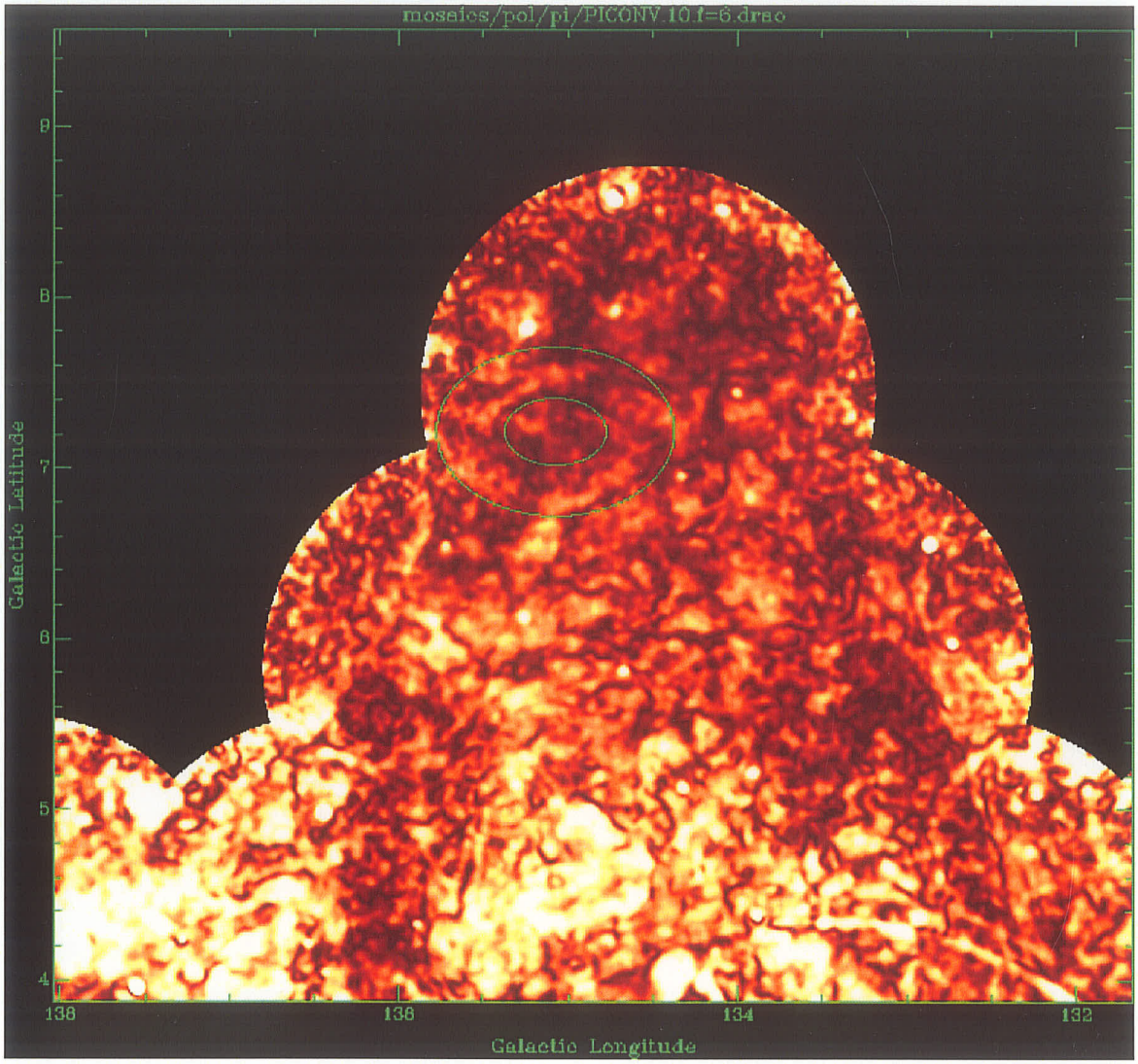

Figure 5-7: Polarized intensity map cropped to show the high latitude fields. The elliptically shaped overlays indicate the position of the *wishbone*.

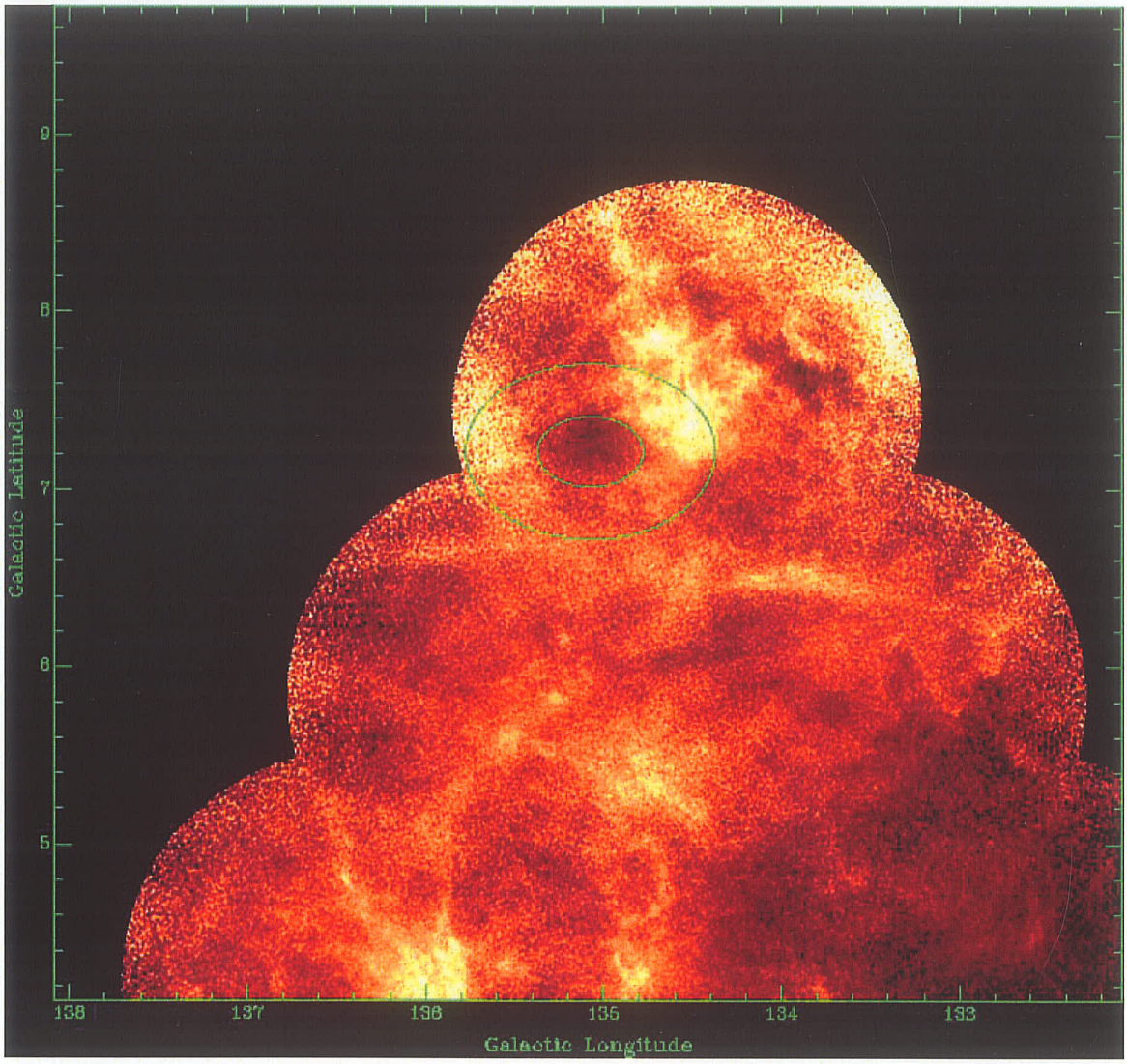

Figure 5-8: HI spectral line data integrated through velocity channels v = -17.02 km/s to v = -23.62 km/s. The ellipses overlaid indicate the position of the *wishbone* as shown in Figure 5-7.

5.1.4.2 Bright knot of strong polarized intensity

A bright, "comma" shaped, knot of strong polarized intensity with approximate centre coordinates of (134.5°, 2.58°) is observed (see Figure 3-9). It is ~0.5° wide and ~0.2° high and has a peak intensity of 0.46 K at full resolution (~1'). A tight box around the object extending from $b = 2.45°$ to $b = 2.65°$ and from $l = 134.8°$ to $l = 134.3°$ has a mean intensity of 0.16 K. The object appears near the base of the "rabbits ears" which are visible in both HI and 60 μm IRAS dust emission. However, there is no clear morphological evidence of an association. The SIMBAD database, operated at the Centre de Données astronomiques de Strasbourg (CDS), Strasbourg, France, was searched for coincident catalogue objects. Table 5-2 gives a complete listing of the objects contained within the box described for the mean intensity measurement. Several of the stars are listed as being part of a cluster although it is unclear to which cluster they belong as a literature search revealed no catalogued cluster near this location (with the exception of OCl 352).

A significant nearby object is the magnitude 8.90 (V) O8 class star, BD+62 424 with coordinates 134.53°, +2.46°. There have been two, distinctly different radial velocity measurements on this star; Abt, Levy, & Gandet (1972) measured a value of –42.5 km/s while Fehrenbach et al. (1996) measured a value of –9 km/s. The measurement of Abt et al. (1972) is consistent with the chimney velocities as observed in the HI spectral line. However the radial velocity measurement of Fehrenbach et al. (1996) has a kinematic distance of ~800 pc (Brand & Blitz 1993) implying that this star is a foreground object.

Object Designation	Object type	Gal. Long. (°)	Gal. Lat. (°)	Mag. (B)	Mag. (V)	Spectral type
GSC 04051-01988	star (in cluster)	134.29	2.56		12.3	A1
V* V677 Cas	irregular variable star	134.33	2.65	15.6		
GSC 04051-01576	star (in cluster)	134.35	2.46		11.7	A1V
GSC 04051-01536	star	134.43	2.53	10.84	9.49	
GSC 04051-01882	star	134.48	2.62	11.34	10.9	
SV* P 70	variable star	134.48	2.63	9.27	7.82	K2
BD+62 424	star (in cluster)	134.53	2.46	9.23	8.9	O8
GSC 04051-01458	star (in cluster)	134.64	2.55	10.84	10.45	A1V
GSC 04051-01774	star (in cluster)	134.65	2.5	11.7	11	A2V
IRAS 02335+6244	infrared source	134.65	2.52			
GSC 04051-02146	star (in cluster)	134.65	2.53	11.43	11.1	B9V
V* V488 Cas	variable star	134.68	2.61			M7
IRAS 02340+6248	infrared source	134.68	2.61			
BD+62 428	star (in cluster)	134.72	2.52	10.76	10.24	B...
IRAS 02342+6238	infrared source	134.76	2.47			
GSC 04051-02154	star	134.77	2.49	10.24	9.79	
GSC 04051-01312	star (in cluster)	134.78	2.56	11.43	11	A4V

Table 5-2: Sources associated with the polarized "knot".

The high polarized intensity of this knot would suggest that its source is at a distance less than the distance to the W4 region, since unlike the surrounding region, it does not appear to suffer depolarization.

5.1.5 Dark ring at 408 MHz

A ring of low 408 MHz intensity with radius ~1.4° and centred at approximately $l = 137°$, $b = 7°$ is observed (Figure 5-9). The intensity inside the ring is ~4 to 5 K below the intensity of the surrounding region. This ring is coincident with a ring observed in polarization data by Haverkorn, Katgert, & de Bruyn (2003) using the Westerbork

Synthesis Radio Telescope (WSRT) at 5 frequencies between 341 and 375 MHz. Haverkorn et al. (2003) detect this ring in polarized intensity (Figure 5-10) and in polarization angle, but not in total power (Stokes I). They find the RM decreases over the ring from ~0 rad/m^2 at the edge to –8 rad/m^2 in the centre while the RM outside the ring is slightly positive. They propose that the ring is a predominantly magnetic feature with a maximum line of sight magnetic field component at the centre and directed away from the observer, given its RM structure. No convincing connections with other known objects were found.

Verschuur (1968) observed this region in polarized emission at 408 MHz. He detected a ring of low polarized intensity that is coincident with the ring observed by Haverkorn et al. and in our data. It is proposed that the ring is due to "an organized magnetic field in the local spiral arm". The region was re-observed in neutral hydrogen (Verschuur, 1968) and found an HI deficiency apparently associated with the depolarized ring.

The low emission ring observed in our 408 MHz data may not be indicative of absorption or low emission in total power at 408 MHz but rather that the polarized emission is "leaking" into the Stokes I continuum data (R. Kothes, private communication). If this is the case, the observations would confirm the depolarized ring observed by Verschuur (1968). Additional data is needed to decide whether this is the case.

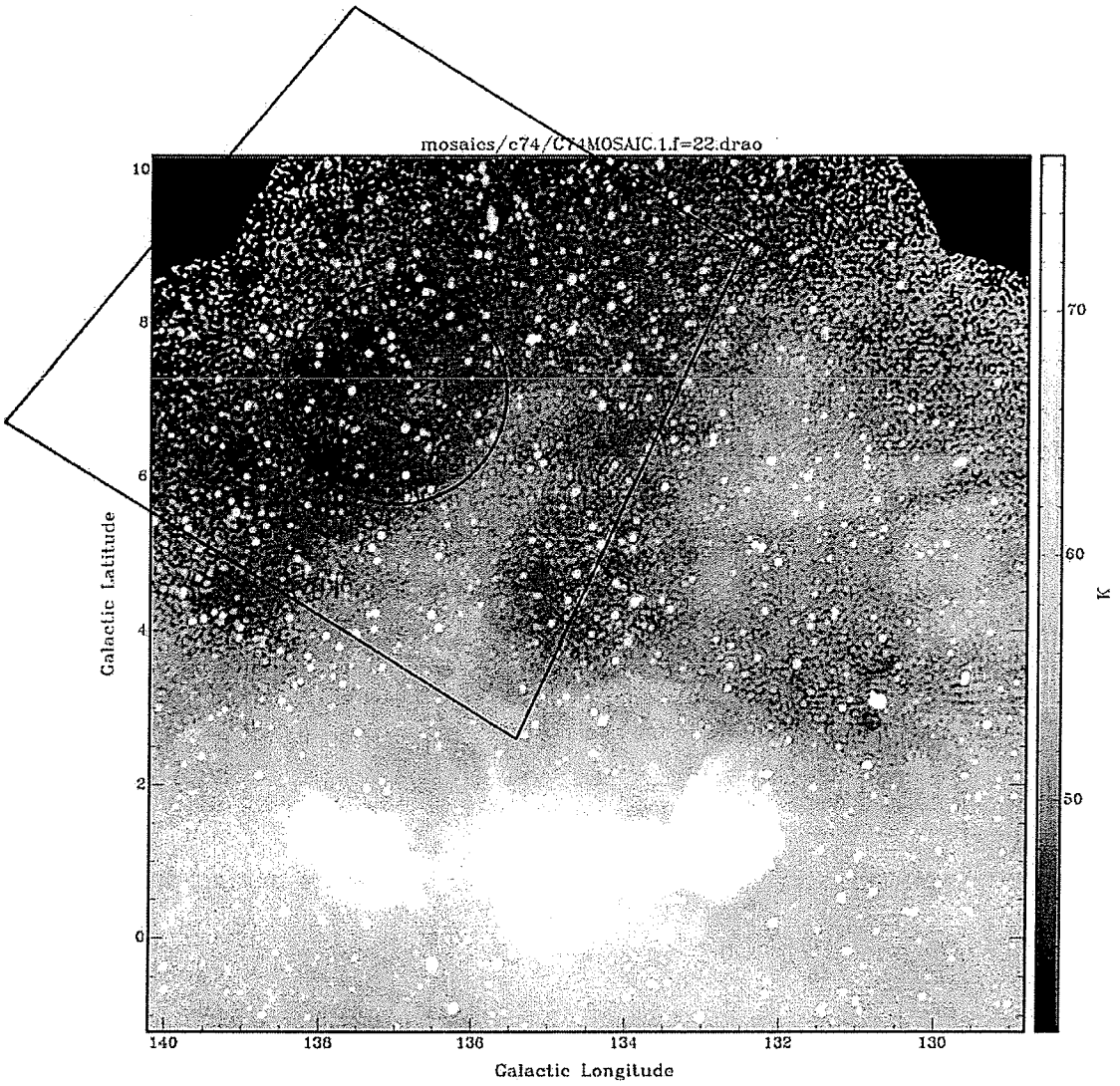

Figure 5-9: 408 MHz continuum image scaled to enhance the low intensity "ring" centred at l = 137°, b = 7°. The overlay indicates the position of the data from Haverkorn et al. (2003) (see Figure 5-10). The circle shown is centred at l = 137.0°, b = 7.1° and has a radius of 1.44° which is coincident with the circle shown in Figure 5-10.

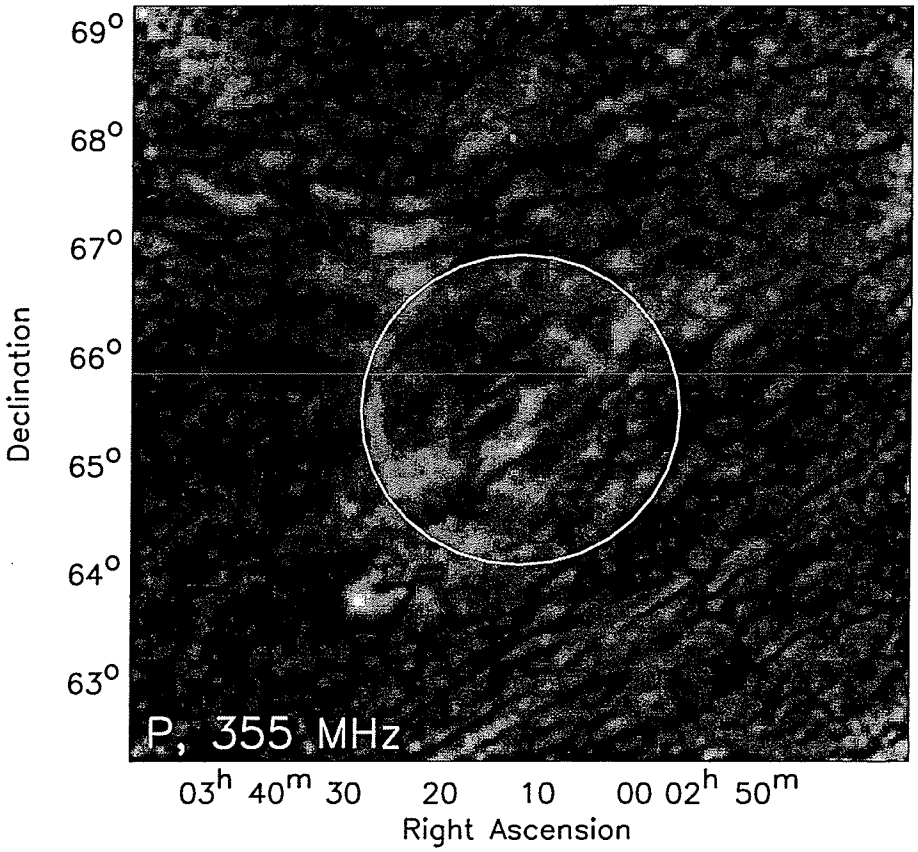

Figure 5-10: Polarized intensity (PI) image of approximately 5' resolution at 355 MHz from Haverkorn et al. (2003). The circle shown is centred at l = 137.0°, b = 7.1° and has a radius of 1.44°.

It should also be noted that the data of Haverkorn et al. (2003) overlaps partially with our 1420 MHz polarization images including our "wishbone" feature and one side of the depolarized "wall" of our *egg*. Figure 5-11 shows our 1420 MHz polarized intensity image with an overlay indicating the region observed by Haverkorn et al. (2003) (Figure 5-10).

There does not appear to be any obvious correlation between the polarized intensity at 355 MHz and our observed polarized intensity at 1420 MHz in the case of the depolarized "wall". However, in the case of the *wishbone* there does appear to be some corresponding polarized intensity between the two images.

Further analysis on this object is beyond the scope of this thesis. Additional observations are desired to assess if a relationship exists between the *wishbone* and the polarized "ring".

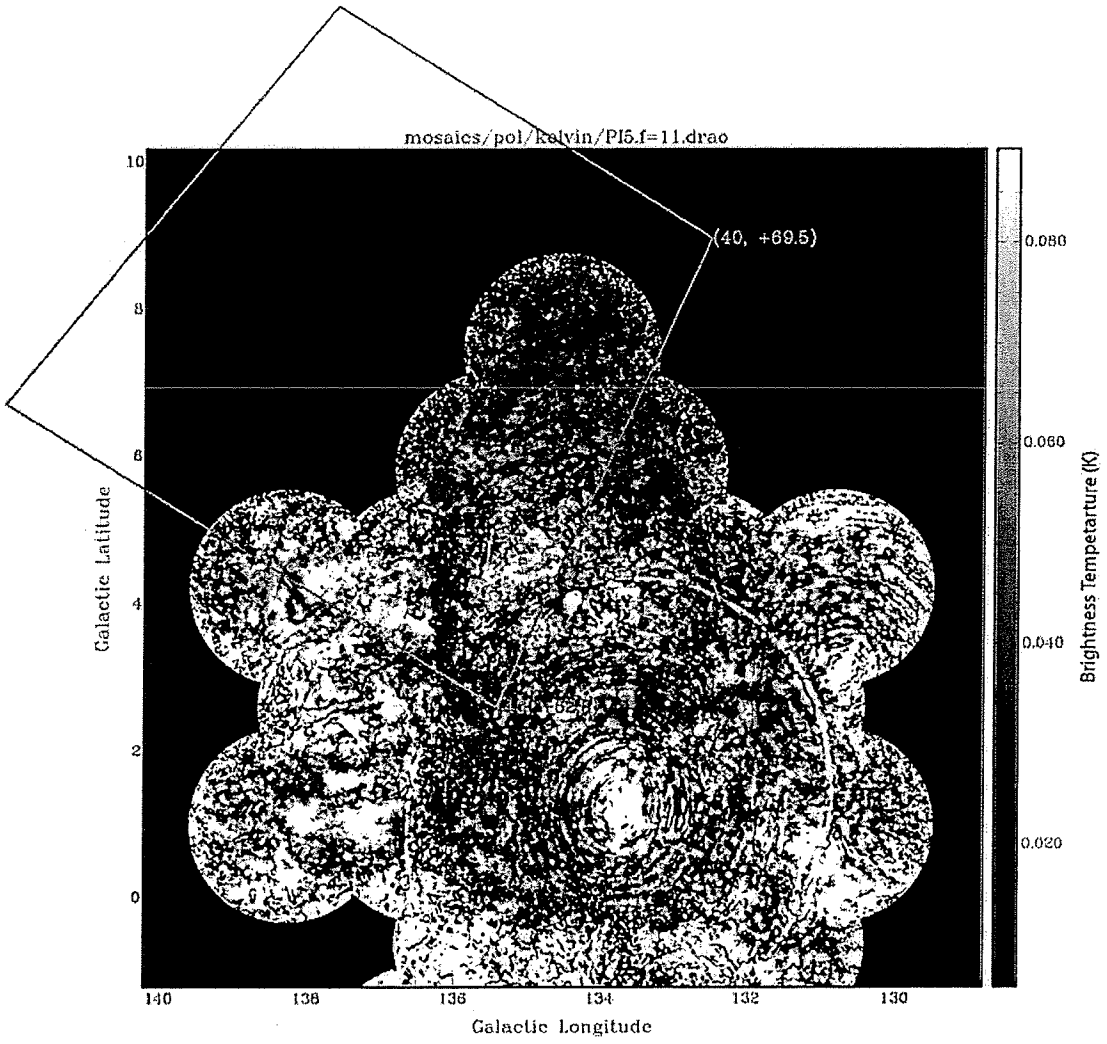

Figure 5-11: 1420 MHz polarized intensity image at a resolution of 5' with overlay of region observed by Haverkorn et al. (2003) (Figure 5-10)

5.2 Conclusions

5.2.1 Summary of this work

Compelling evidence for the existence of a fragmented superbubble that is in the process of evolving into a chimney has been found. This evidence includes morphological correlations between our 1420 and 408 MHz continuum datasets, the 1420 MHz polarization datasets and the Hα data of DTS97 together with evidence for two breaks in the continuous egg-shaped structure. The *egg* measures ~165 pc wide and extends ~240 pc above the mid-plane of the Galaxy, the upper portion of the egg reaching beyond 135 pc which is the σof the global Gaussian HI distribution. While this is not into the Galactic halo, the breaks in the structure may provide a means for the ionizing radiation to escape to latitudes higher than the top of the *egg*.

These observations are consistent with the conclusion of Terebey et al. (2003) that up to 56% of the ionizing photons escape from the small, ~1° or 40 pc loop surrounding OCl 352. These photons are available for ionizing gas within the *egg* structure and excess photons have a means of escape. We predict that at least 5% of the photons produced in the cluster are able to escape through the upper break in the structure and thus available for ionizing the halo. This prediction is not sufficient to account for the observed ionization in the large Hα loop in the WHAM data. However, it is possible that sufficient energy escapes and is able to ionize the 1 kpc loop if one relaxes the constraint that most

of the radiation escapes out of the side of the *egg* structure or if radiation escaping through the side break does contribute to the ionization of the large loop.

Polarized intensity images, showing depolarization that extends from W4 up the walls of the superbubble, provide strong evidence that the observed continuum and Hα emissions are at the same distance as the W4 region. The temperature spectral index map of the region indicates that there are not high energy losses in the region due to synchrotron emission and imply that existing cosmic rays have sufficient energy for escaping into the Galactic halo via a convection model of transport. The rotation measure in the region is calculated so that the line of sight magnetic field in the region can be estimated. We find $B_{//} = 9 \pm 8$ μG assuming a wall thickness of 20 pc or $B_{//} = 13 \pm 11$ μG assuming a wall thickness of 10 pc and in a direction that is *towards* the observer. Both values are consistent with the ambient Galactic magnetic field within the error, but the best estimates of 9 or 13 μG are 2 to 6 times stronger than the generally accepted values for the line of sight component of the Milky Way's field.

5.2.2 Future endeavours

A consistent picture of the connection between this complex region and the Galactic halo is beginning to develop, but more work is needed to definitively declare W4 as a young chimney.

Modeling is required to investigate whether the multiple star forming epoch scenario is appropriate to this region. The Kompaneets modeling by Basu et al. (BJM99) has yielded some interesting results, however the predicted scale height from this model contradicts the observations. The model is simple and does not account for the complex density variations in the interstellar medium which may be especially important in this region.

Modeling the polarization of the ambient Galactic medium with an embedded plasma shell is another avenue worthy of investigation. Such modeling could confirm the Faraday rotating effect of the shell and indicate if the estimate of the *eggshell*'s contribution to the rotation measure is reasonable.

Additional observations will also help to confirm or refute the picture developed in this thesis. The Fabry-Perot Hα observations collected at Mont Megantic (G. Joncas; private communication) will indicate if Hα emission is occurring at velocities consistent with those in HI spectral line observations. Such a detection would be strong confirmation that the observed *egg* structure is indeed contiguous and a result of ionizing radiation from OCl 352.

X-ray observations would be useful to indicate whether there is any hot, X-ray emitting gas contained within the egg structure. These observations may also indicate whether gas is escaping through the breaks identified in this thesis.

To assess whether it would be feasible to detect X-rays from the region we estimate the temperature in the region by comparing the magnetic energy density to the thermal density

$$P_{\mathrm{B}} = P_{thermal}$$
$$\frac{B^2}{4\pi} = 2n_e kT \qquad (5\text{-}1)$$

If the temperature is 10^6 K or higher then it is likely for X-rays to be detected as at lower temperatures it is more likely for the diffuse X-ray emission to be absorbed by the interstellar medium (Morrison and McCammon 1983). Using the electron density calculation for the upper shell (see section 4.2.1), n_e = 0.44 cm^{-3}, and Eq. (5-1) we find the total magnetic field must be ~40 μG for a temperature of 10^6 K. Our magnetic field calculation from the rotation measure was $B_{//} = 13 \pm 11$ μG assuming a wall thickness of 10 pc, but is just the line of sight component of the magnetic field. It is plausible that the magnetic field in the region is higher since the ambient field is thought to be dragged upwards during the formation of a superbubble (Norman & Ikeuchi 1989) and most of the field is directed up, tangential to the shell. Thus if the total field is 2 or 3 times the line of sight component, the temperature in the region is sufficiently high to produce detectable X-ray emission.

In addition, absorption from atomic hydrogen along the line of sight will obscure X-rays emitted at the source and may, if the column density is high enough, obscure them completely. A column density of ~10^{22} atoms cm^{-2} is high enough to prevent the

detection of X-rays whereas a column density of ~10^{20} atoms cm^{-2} is low enough to allow detection of X-rays given a high enough flux (S. Safi-Harb, private communication). Normandeau et al. (1996) found the column density to W4 to be 2.6 x 10^{21} atoms cm^{-2} which decreases to 1.4 x 10^{21} atoms cm^{-2} as one increases the Galactic latitude to 3.8°. Thus the detection of X-rays from the region is likely to be difficult or impossible if they are produced by gas with a temperature of 10^6 K.

5.2.3 In search of other chimneys

Theoretical predictions estimate that there should be many more disk-halo conduits than have so far been identified. Estimates of the number of conduits range from 1000 (Norman and Ikeuchi, 1989) to between 50 and 100 (Heiles et al., 1996). Chimneys require the existence of an energy source at the base to create the initial bubble and to power the outflow. The only known phenomena that would produce sufficient energy are supernovae or the combined winds of several supermassive O or B type stars. Since the chimney formation theories suggest that all these regions should be blowing chimneys it would be interesting to target such regions in a search for additional chimneys.

Catalogues of chimney candidates such as Koo, Heiles, & Reach's (1992) catalogue of worm candidates have been produced by examining the HI and IR datasets first, and afterwards checking for associations with possible energy sources. We propose turning the problem around by first identifying possible energy sources and then investigating whether chimney-like phenomenon are evident.

This search would examine IGPS datasets in proximity to known OB associations and Galactic clusters in an effort to identify additional W4-like chimneys. Other datasets could be utilised to check for other chimney features like dust walls (using IRAS data) and ionization or shocks (using continuum data). Melnik and Efremov (1995) have compiled a catalogue of OB associations and Mermilliod (1993) has developed a database of Galactic clusters, both of which could be used to highlight regions of interest for this survey.

References

Abt, H. A., Levy, S. G., & Gandet, T. L. 1972, AJ, 77, 138-143

Basu, S., Johnstone, D., & Martin, P. G. 1999, ApJ, 516, 843

Beck, R. 2001, Space Sci. Rev., 99, 243

Bevington, P. R. & Robinson, D. K. 1992, Data Reduction and Error Analysis for the Physical Sciences, 2nd Ed. (Boston: WCB/McGraw-Hill), 96:114, 194:219

Binney, J. & Merrifield, M. 1998, Galactic Astronomy (Princeton: Princeton University Press), 551

Bowers, R. & Deeming, T. 1984, Astrophysics II (Boston: Jones and Bartlett), 360:1, 398:9, 455:6

Brown, J-A. C. 2002, Ph. D. thesis, University of Calgary, Calgary, Canada

Brand, J. & Blitz, L. 1993, A&A, 275, 67

Burke, B. F. & Graham-Smith, F. 1997, An Introduction to Radio Astronomy (Cambridge: Cambridge University Press), 106:110

Carpenter, J. M., Heyer, M., & Snell, R. L. 2000, ApJS, 130, 381

Chu, Y.-H., Gruendl, R. A., & Guerrero, M. A. 2003 in *Winds, Bubbles and Expansions*, Eds. Arthur, S. J. & Henney, W. J.

Condon, J. J. 1992, Ann. Rev. A&A, 30, 575-611

de Avillez, M. A. & Berry, D. L. 2001, MNRAS, 328, 708

Dennison, B., Topasna, & G. A., Simonetti, J. H. 1997, ApJ, 474, L31

Dickey, J. M. & Lockman, F. J. 1990, ARA&A, 28, 215

Fehrenbach, Ch., Duflot, M., Genty, V., Amieux, G. 1996, BICDS, 48, 11F-13

Gaensler, B. M., Dickey, J. M., McClure-Griffiths, N. M., Green, A. J., Wieringa, M. H., & Haynes, R. F. 2001, ApJ, 549, 959

Gonzalez, R. C. & Woods, R. E. 2002, Digital Image Processing (Upper Saddle River: Prentice-Hall, Inc.), 147:219

Gray, A. D., Landecker, T. L., Dewdney, P. E., Taylor, A. R., Willis, A. G., & Normandeau, M. 1999, ApJ, 514, 221

Gray, A. D., Landecker, T. L., Dewdney, P. E., & Taylor, A. R. 1998, Nature, 393, 660

Han, J. L., Manchester, R. N., Lyne, A. G., & Qiao, G. J. 2002, ApJ, 570, 17
Haslam, C. G. T., Stoffel, H., Salter, C. J., & Wilson, W. E. 1982, A&AS, 47, 1

Haverkorn, M., Katgert, P., de Bruyn, A. G. 2003, A&A, 404, 233

Heiles, C., Reach, & W. T., Koo, B.-C. 1996, ApJ, 466, 191

Heyer, M. H. 1995 in *CO:Twenty Five Years of Millimeter Wave Spectroscopy,* Eds Latter, W. B, Radford, S. J. E., Jewell P. R., Mangum, J. G. & Bally, J.

Högbom, J. 1974, ApJS, 15, 417

Irwin, J. & English, J. 1996, BAAS, 28, 1361

Kallas, E., Reich, W., & Haslam, C. G. T. 1983, A&A, 128, 268

Kerton, C. R. & Martin, P. G. 2001, PASP,113, 872

Koo, B.-C., Heiles, C., Reach, W. T. 1992, ApJ, 390, 108

Lada, C. J., Elmegreen, B. G., Cong, H-I, & Thaddeus, P. 1978, ApJ, 226, L39

Landecker, T. L., Dewdney, P. E., Burgess, T. A., Gray, A. D., Higgs, L. A., Hoffmann, A. P., Hovey, G. J., Karpa, D. R., Lacey, J. D., Prowse, N., Purton, C. R., Roger, R. S., Willis, A. G., Wyslouzil, W., Routledge, D., & Vaneldik, J. F. 2000, A&AS, 145, 509

Lang, K. R. 1980, Astrophysical Formulae (Berlin: Springer-Verlag), 11

Lerche, I. & Schlickeiser, R. 1980, ApJ, 239, 1089

Lisenfeld, U. & Völk, H. J. 2000, A&A, 354, 423

Lockman, F. J., Hobbs, L. M., & Shull, J. M. 1986, ApJ, 301, 380

Longair, M. S. 1997, High Energy Astrophysics (Cambridge: Cambridge University Press), 81:2

McClure-Griffiths, N. M., Dickey, J. M., Gaensler, B. M., Green, A. J., Haynes, R. F., Wieringa, M. H. 2000, ApJ, 119, 2828

Melnik A.M., & Efremov Yu.N. 1995, Pis'ma Astron. Zh. 21, 13

Mermilliod, J.-C. 1993, in *Workshop on Databases for Galactic Structure*, Eds A.G.D. Philip, B. Hauck & A.R. Upgren (L. Davis Press), p. 27-34. http://obswww.unige.ch/webda/

Morrison, R. & McCammon, D. 1983, ApJ, 270, 119

Norman, C. A. & Ikeuchi, S. 1989, ApJ, 345, 372

Normandeau, M. 2000, in *Stars, Gas and Dust in Galaxies: Exploring the Links*, Eds. D. Alloin, G. Galaz, and K. Olsen

Normandeau, M. & Basu, B. 1999, in *New Perspectives on the Interstellar Medium*, Eds. Taylor, A. R., Landecker, T. L., & Joncas, G.

Normandeau, M., Taylor, A. R., & Dewdney, P. E. 1997, ApJS, 108, 279

Normandeau, M. 1996, Ph. D. thesis, University of Calgary, Calgary, Canada.

Normandeau, M., Taylor, A. R., & Dewdney, P. E. 1996, Nature, 380, 687

Owens, A. J. & Jokipii, J. R. 1977, ApJ, 215, 677

Reich, P., Reich, W., & Fürst, E. 1997, A&AS, 126, 413

Reich, W., Reich, P. & Fürst, E. 1990, A&AS, 83, 539

Reich, P., & Reich, W. 1988, A&A, 196, 211

Reich, P., & Reich, W. 1986, A&AS, 63, 205

Reich, W. 1982, A&AS, 48, 219

Reynolds, R. J. 1991, ApJ, 345, 372

Reynolds, R. J., Sterling, N. C., & Haffner, L. M. 2001, ApJ, 558, L101

Rohlfs, K. & Wilson, T. L. 2000, Tools of Radio Astronomy (Berlin: Springer-Verlag), 13, 232:50

Rybicki, G. B. & Lightman, A. P. 1979, Radiative Processes in Astrophysics (New York: John Wiley and Sons), 178

Safi-Harb, S. 2002, in *New Views on Microquasars*, Eds. Ph. Durouchoux, Y. Fuchs, & J. Rodriguez (Center for Space Physics: Kolkata (India)), 235

Steinberg, J. L. & Lequeux, J. 1963, Radio Astronomy (New York: McGraw-Hill), 96:116

Taylor, A. R., Gibson, S. J., Peracaula, M., Martin, P. G., Landecker, T. L., Brunt, C. M., Dewdney, P. E., Dougherty, S. M., Gray, A. D., Higgs, L. A., Kerton, C. R., Knee, L. B. G., Kothes, R., Purton, C. R., Uyaniker, B., Wallace, B. J., Willis, A. G., & Durand, D. 2003, AJ, 125, 3145

Tenorio-Tagle, G. & Bodenheimer, P. 1988, ARA&A, 26, 145

Terebey, S., Fich, M., Taylor, R., Cao, Y., & Hancock, T. 2003, ApJ, 590, 906

Thronson, H. A., Campbell, M. F. & Hoffmann, W. F. 1980, ApJ, 239, 533

Tomisaka, K. & Ikeuchi, S. 1986, PASJ, 38, 697

Uyaniker, B., Landecker, T. L., Gray, A. D., & Kothes, R. 2003, ApJ, 585, 785

Verschuur, G. L. 1969, AJ, 74, 597

Verschuur, G. L. 1968, Obs. 88, 15

Westerhout G. 1958, BAN, 14, 215

Wheelock, S., Chillemi, J., Gautier, N., Gregorich, D., Kester, D., McCallon, H., Oken, C., White, J., Chester, T. 1991, BAAS, 23, 908

Appendices

1: Image processing of Dominion Radio Astrophysical Observatory Synthesis Telescope images

In the Dominion Radio Astrophysical Observatory (DRAO) nomenclature, the images to be processed are labeled KM, KN, and KT (see Chapter 3). These are the high latitude extension of CGPS fields - above the W3/4/5 region - collected by Magdalen Normandeau in 1998. Each field includes data at 21 cm and 74 cm continuum (Stokes I) and 21 cm polarization (Stokes Q and U). Note that scripts referred to in this appendix were written by R. Kothes, A. Gray or B. Uyaniker except where noted as written by the author and obtained from R. Kothes. Those written by the author are included at the end of this appendix.

This processing was completed with assistance and advice from Roland Kothes. I was working from the machine "castor.drao.nrc.ca" at DRAO.

Image files in the "DRAO format" do not include a header. Instead, the image data is stored separately and a file called deffil.mad stores the file "definitions". These

definitions are numbered and provide a way to refer to the image data when using various DRAO export software.

The processing uses the file manipulation program known as "madr". Here is a list of the commands used in this processing -

```
name        lists file names and definition numbers (no more than 200
            file definitions per directory allowed)
neg         deletes file and corresponding definition
            syntax (eg. delete files 2, 3 and 4)          neg f2:4
rdir        switches to a remote directory
            syntax (eg. switch to ../myfiles/)      rdir
                  when promted:                     ../myfiles/
rname       lists files in a remote directory
rget        copys files (data and definition) from a remote directory
```

1.1 On producing scripts

The programs used in this processing all have the same general format. One types the name of the program at the command prompt to run the program and then one must respond to a series of questions. The majority of questions in many of the programs can be answered with the default response and to do this one simply enters "return". Only questions which were answered with a response other than the default will be discussed here.

With most of the programs, a script may be generated by typing "&scriptname" at the prompt of the first question. All subsequent responses will then be recorded in a file called scriptname.dra in the current directory. The script may then be edited for use with

other files. It is called by typing "@scriptname" at the prompt of the first question in one of the drao programs.

1.2 Pre-processing

Before beginning the processing, one must determine the clean and steer limits for each raw image. The "clean limit" is the lowest level at which a point source will be cleaned (i.e. "sources" with values below the clean limit are assumed to be noise). The "steer fraction" applies to the space between the point sources (i.e. the extended emission) and defines the level below which is considered noise.

I was advised to use the following guidelines:

First, determine the maximum value in the image. Call it "max".

```
Clean limit
      - stop cleaning between 1 and 2 mJy -> take 1.5 mJy
      - clean limit = 1.5/max

Steer fraction
      - the weak extended emission value ~6 mJy
      - steer limit = 6/max
```

The following table shows the clean limit and steer fractions for the three fields at both 21 cm and 74 cm:

	clean limit	steer fraction
km c21	0.01	0.05
kn c21	0.01	0.05
kt c21	0.005	0.05
km c74	0.01	1.0
kn c74	0.01	1.0
kt c74	0.01	0.05

1.3 Processing

Now one may begin the processing. The raw images are separated into individual directories. In the directory of the image to be processed:

```
1. run ph2  (at prompt, type: ph2)
```

Short for "phase 2", ph2 is used to produce the dirty beam (.P21 or .P74 files) and the dirty map (.M21 or .M74) from the visibility files.

```
2. run clean (at prompt, type: /opt2/draoexport/bin/clean - need to
type whole path or uses the wrong clean program...)
```

This program replaces "sidelobish point-source responses in the map with gaussian responses of the same width". (From *Cleaning and self-calibrating continuum maps – an overview* available on the DRAO website).

The program will prompt with a table in which the following parameters must be changed:

```
1     250 (# iterations)
2     clean limit (value found before processing
      began)
3     steer fraction (value found before processing
      began)
4     9999999 (some very large number)
```

```
3. run script: smallmap21
```

This script produces a "final" total power (Stokes I) map. At this point a final map is produced for inspection.

4. The following scripts are specific to the km, kn and kt fields and the particular directory structure I had set up and were written by the author (see the end of this appendix, section 1.8). These would require to be rewritten to process an arbitrary field.

```
run script: phself_1
run script: aself_1
run script: baseline
```

These scripts run other scripts that perform various self-calibrations. There are at times phase (scripts phself_1 and also baseline) and amplitude (script aself_1) variations in the telescope system that may be removed by self calibration.

Examine results after each step (after running each script), looking for asymmetrical artifacts around point sources. If no improvement visible or if additional artifacts have been created, delete the newly created maps and continue with the maps created in the previous step.

1.3.1 Modcal

The program "modcal" (modcal21 and modcal74) is used to remove rings around point sources. The source must be sufficiently strong for this procedure (above 30 or 40 mJy for C21 data; above 500 mJy for C74). The following parameters are required for input when running the program:

```
1. define a box around the source -
- need pixel coordinate (x, y) from lower left and top right corners
(use the clean components (CC) map (created in the previous step) for
this box. It should enclose all central pixels which appear in CC map)

2. choose a lower limit -
```

```
- examine the CC map - are there artifacts visible? (i.e. rings
encircling the central source)
- the lower limit should be the lowest value which is above the counts
for most of the artifacts i.e. if most artifacts have a value of 0.35
mJy or lower, choose 0.4 for a lower limit
- typical lower limit should be around 0.3 - 0.5, and not higher than
1.0
- if there are no artifacts take 0 for the lower limit

3. choose a value for the shortest telescope baseline -
      - depends on max value of source:
            above 100 mJy ->        12 (m)
            80 - 100 mJy ->         24 (m)
            under 80 mJy ->         36 (m)

4. note the code for the last visibility file created (ie AA, AB, etc);
note the file definition number for the corresponding CC map
```

1.3.2 Removing interference

Field KT had interference which showed up as regularly spaced stripes on the image. To remove the interference:

```
1. run script: sub_model
```

This creates model of point sources in image and subtracts this model from the original image, producing a new image (which contains no point sources).

```
      parameters:

      define window (should contain nothing meaningful (ie noise) -
      eg (6, 6) -> (8, 8)), this window is outside the useful beam

      when prompted: model outside window?
      respond: yes

      This way the program will produce a model of all the point
      sources in the image (can also be used to produce a model of a
      single source which is inside the "window").


2. run ph2

      parameters:

      when prompted: Type of maps to make (I,Q,U,V,...
      respond: I
```

```
      when prompted: Bands to be included (A, B, C, D, All)
      respond: A

      This will create an I (total intensity) map for band A; do the
      same for B, C, and D

3. run dove
```

DOVE is an IDL program which allows one to manually edit each of the RR and LL visibility files in each band (8 files)

```
      1. load file
      2. choose amplitude - data to view
      3. choose Flag mode - erase
      4. identify interference "features" and click on either side to
      remove from the data
```

The interference features for this field were apparent in several channels on the extreme right hand side. They are obvious deviations from the general trend of the data.

1.3.3 Removing off-image source grating rings

Most images (except KMC21 and KTC21) had grating rings due to off image (strong) sources (3C58, W3, CasA). These are removed by using a model of the source and subtracting this from the original image.

```
1. Need a model of the source
      models in the form of .MAP files exist on the DRAO system

2. Need a model of the field
      for C21: run script: sub_model

            use default values except enter "no" for "use only positive
            clean components"

      for C74: use madr to manually subtract model (say file #1) from
      the last visibility file (say file #2)

            madr
            man
            f2m = f2 - f1      (here the "m" after f2 means that f2 is
                                being manipulated and replaced)
```

```
3. run ptsrcs
      parameters are defined in script

4. Add the model back into the field
      for C21: run script: add_model

            use default values except enter "no" for "use only
            positive clean components"

      for C74: use madr to manually add the model (say file #1) from
      the new visibility file (say file #3)

            madr
            man
            f3m = f3 + f1      (here the "m" after f3 means that f3 is
                               being manipulated and replaced)
```

5. The centre of the image will have been shifted in the above process, it must be shifted back before creating a map from the visibility file.

```
      run ph2
      parameter #7 in table must be changed
            enter "n" when prompted if parameters in table are correct
            enter "7" to change parameter #7
            enter "y" when prompted if parameters in table are correct
      program should be cancelled after changing this parameter

6. run script "bigmap" entering the code from the newly created
visibility file. This produces the final image!
```

1.4 Polarization processing

```
1. create a new directory and copy into it (for a particular field):
      using madr:

      last visibility files (eg KMRRA.V21BS, KMLLA.V21BS, KMRRB.V21BS,
      ... etc) (8 files)
      final map (eg KMI21.FIN) (1 file)


      using cp:

      .TBL file
      .HISTORY file
      all *.021 files
      all *.E21 files
      all *.C21 files
      all *GAINS* files
```

```
2. logon to the machine cass (at DRAO) in order to gain access to the
following script:
run: ~agray/bin/IBM/scmrg
enter codes of gains (i.e. look at the *GAINS* files and enter all two
letter codes (AA, AB, AC) that gains exist for...)
This script merges the *GAINS* files.

run script: vis
check .C21 file for version

logoff cass

3. run program: to_stokes
specify Stokes params. I Q U (not V)

4. run ph2
parameters are defined in the scripts:
                  make_mapa
                  make_mapb
                  make_mapc
                  make_mapd

5. run /opt2/draoexport/bin/clean
parameters are defined in the scripts:
                  clean_au, clean_aq
                  clean_bu, clean_bq
                  clean_cu, clean_cq
                  clean_du, clean_dq

6. logon to cass;

run:  inspolcorr
parameters are defined in the scripts:
                  inspolcorr_a
                  inspolcorr_b
                  inspolcorr_c
                  inspolcorr_d
logoff cass

7. the bands now need to be combined into single Q and U images

in madr: create new file definitions
example: determine the last file definition in the directory - say #77
as was for KM

have files        KMQ21_ACORR.C1 => file #70
                  KMU21_ACORR.C1 => file #71

now create the new definitions:
                  copy f70 78
                  copy f71 79
this makes copies of files 70 and 71 to the new definitions 78 and 79

now define the new files to change the names:

d f78
```

```
changed the name to KMQ.final, all other attributes left as default

now:
                    man
                    f78 = f70 + f72 + f74 + f76
                    f78m = f78/4
                    f79 = f71 + f73 + f75 + f77
                    f79m = f79/4

this adds all the bands (a, b, c, & d) for each of the Q and U images
separately.
```

1.5 Mosaicking

Mosaicking is a preformed by running `supertile`. (i.e. Type `supertile` at the command prompt on a machine which has the DRAO export software package installed.) As with many of the programs in this package, the user is presented with a list of questions, many of which can be answered with the default value (i.e. by pressing return). The questions that often require a response other than the default, are outline here:

`Are you adding new datasets to a partially-completed mosaic?`

There are a maximum of 16 datasets (fields) that may be mosaicked in a single run. If more than 16 datasets are to be mosaicked one must respond "yes" to this question on the second run.

`Are oversize input datasets to be processed?`

Oversize datasets are considered to be those over 1024x1024. The single fields I was mosaicking were 512x512 pixels which are not oversize. However, if adding fields to a partially completed mosaic, then one will likely need to respond "yes" as the partial mosaic is probably larger than 1024x1024.

```
Select max. number of input datasets (S=4,M=8,L=16)
```

Select the appropriate option (i.e. type "S", "M", or "L") depending on how many fields are to be mosaicked.

```
Are datacubes (rather than single images) being mosaiced?
```

Must respond "no" if not mosaicking datacubes.

```
Specify the input datasets:
```

Type the file definition numbers (i.e. from madr) for the files to be mosaicked (entered one at a time)

```
Add another dataset?
```

Respond "no" when finished entering all of the input datasets.

```
Radius to zero weights beyond (arcmin):
```

The default (93.0 arcmin for 1420 MHz Stokes I and 289 arcmin for 408 MHz) can be accepted except for polarization images. A value of 80 arcmin was used for the Stokes Q and Stokes U.

```
Specify output files(s) for mosaiced dataset
   File definition number [DEFINE FILE]:
```

Enter return after this prompt (unless there is already a file definition created for the output image). Then this prompt:

```
File name (max 52 chars) [] ("/?" = help):
```

should appear. Type the output file name.

```
Basic element and record dimensions (E,R):
```

Type the desired size for the output dataset. Mosaics in this thesis are all 2048, 2048.

```
Sky projection (SEGTVACF) [S]:
```

Type "G" for Galactic coordinates.

```
Select velocity-like coordinate (Vel or Freq) [V]:
```

Type "F" for frequency.

```
LONGITUDE of reference element [0.00000D]:
```

The reference element is a particular pixel for which the coordinates are specified. I used the centre pixel (default) as the reference element and 134.5D for the longitude reference.

```
LATITUDE of reference record [0.00000D]:
```

4.5D

```
DELTA LONGITUDE per element (unsigned)
DELTA LATITUDE per record (unsigned)
```

I used 20″ (for longitude and latitude).

```
Specify output files(s) for mosaic weight-array.
```

Enter file name for the weight-array (i.e. see Figure 3-2).

```
Specify output files(s) for resolution datacube
```

Enter file name for the resolution cube. Since it is a data cube it has a *family* of definitions rather than just 1. For this reason, one must end the file name with two "@" symbols (i.e. "res@@") and then the definitions will have names like res01, res02, etc.

```
Specify output files(s) for beam-patch array
```

Enter file name for the beam-patch array.

Additional notes:

When mosaicking Stokes Q and Stokes U images, one must edit the file definitions for the input fields (using madr) to remove the auxiliary astronomical parameters (i.e. to remove reference to the fact that the image is Stokes Q or Stokes U). Supertile gives an error if trying to mosaic images with Stokes Q or Stokes U specified in the file definition.

1.6 Convolving

The DRAO export program `mosconv` is used for convolving mosaics to a lower resolution. An arbitrary value can be entered or the program may be used to match resolutions between images by using the resolution cube produced by `supertile` (see Appendix section 1.5) for specifying the desired convolution. The program prompts for the input file definition number and output file name, and also for the input resolution cube file definition number.

1.7 Reading and writing fits files

The DRAO export programs `rfits` and `wfits` are used to read and write fits files to and from madr format respectively. These programs have much the same interface as the other programs and just require the user to enter the appropriate file name and file definition number for the file to be read/written.

1.8 Scripts

The following scripts were written by the author and are used as described in the preceding text.

file: phself_1

```
cd /rigel4/jwest/km/c21/
time /rigel4/jwest/scripts/phself21_all <<label1
36
0.01
0.05
label1
cd /rigel4/jwest/kn/c21/
time /rigel4/jwest/scripts/phself21_all <<label1
36
0.01
0.05
label1
cd /rigel4/jwest/kt/c21/
time /rigel4/jwest/scripts/phself21_all <<label1
36
0.005
0.05
label1
cd /rigel4/jwest/km/c74/
time /rigel4/jwest/scripts/phself74_all <<label1
12
0.01
1.0
```

```
label1
cd /rigel4/jwest/kn/c74/
time /rigel4/jwest/scripts/phself74_all <<label1
12
0.02
1.0
label1
cd /rigel4/jwest/kt/c74/
time /rigel4/jwest/scripts/phself74_all <<label1
24
0.02
0.05
label1
```

file: aself_1

```
cd /rigel4/jwest/km/c21/
time /rigel4/jwest/scripts/aself21_all <<label1
36
0.01
0.05
label1
cd /rigel4/jwest/kn/c21/
time /rigel4/jwest/scripts/aself21_all <<label1
36
0.01
0.05
label1
cd /rigel4/jwest/kt/c21/
time /rigel4/jwest/scripts/aself21_all <<label1
36
0.005
0.05
label1
cd /rigel4/jwest/km/c74/
time /rigel4/jwest/scripts/aself74_all <<label1
12
0.01
1.0
label1
cd /rigel4/jwest/kn/c74/
time /rigel4/jwest/scripts/aself74_all <<label1
12
0.02
1.0
label1
cd /rigel4/jwest/kt/c74/
time /rigel4/jwest/scripts/aself74_all <<label1
24
0.02
0.05
label1
```

file: baseline

```
cd /rigel4/jwest/km/c21/
time /rigel4/jwest/scripts/phself21 <<label1
KM
AK
60
0.0
36
80
y
0.01
0.05
label1
#
cd /rigel4/jwest/kn/c21/
time /rigel4/jwest/scripts/phself21 <<label1
KN
AC
36
0.0
36
240
y
0.01
0.05
label1
#
cd /rigel4/jwest/kt/c21/
time /rigel4/jwest/scripts/phself21 <<label1
KT
AB
24
0.0
36
480
y
0.005
0.05
label1
#
cd /rigel4/jwest/km/c74/
time /rigel4/jwest/scripts/phaself74_base <<label1
KM
AL
45
0.0
12
40
0.01
1.0
label1
#
```

```
cd /rigel4/jwest/kn/c74/
time /rigel4/jwest/scripts/phself74 <<label1
KN
AD
15
0.0
12
240
y
0.02
1.0
label1
#
cd /rigel4/jwest/kt/c74/
time /rigel4/jwest/scripts/phself74 <<label1
KT
AB
10
0.0
24
480
y
0.02
0.05
label1
```

2: ImageJ plugins

ImageJ (based on NIH Image) is a public domain image processing and analysis program developed at the U.S. National Institutes of Health by Wayne Rasband. It is available for all platforms on the internet at http://rsb.info.nih.gov/ij/. The program is open source and written in the Java programming language and includes a particularly flexible interface for writing customized user plugins. The program is capable of reading and saving data in a raw 32-bit real format (with either big or little endian byte order) with is useful for producing images that may later be read by the DRAO export software (see Appendix 1).

Several plugins were written by the author to perform some of the analysis described in the text. A brief description of the plugins followed by the Java source code is included here. Also see comments within the code itself for details of the execution.

Polarization_: Creates either a polarized intensity or a polarization angle map given the Stokes Q and Stokes U images. See sections 2.2.2.1 and 2.2.2.2 for details.

Rotation_Measure_with_r: Creates a rotation measure map and a linear correlation coefficient map. Uses the unwrapping algorithm of Brown (2002) as described in section 4.1.1.

Make_Averaged_Map: Divides the image into a grid of 16x16 pixels and creates a map consisting of the average value of each grid value.

Make_RM_annotations: Outputs Karma syntax text which may then be saved as a Karma annotation file.

```
 1: import ij.*;
 2: import ij.process.*;
 3: import ij.gui.*;
 4: import java.awt.*;
 5: import ij.plugin.filter.*;
 6:
 7: /**
 8: * Produces a polarized intensity or polarization angle image given
 9: * Stokes Q and Stokes U images as input (selected via a GUI)
10: */
11:
12: public class Polarization_ implements PlugInFilter {
13:         ImagePlus imp;
14:         int Q = 0;
15:         int U = 0;
16:         int compute = 0;
17:
18:         public int setup(String arg, ImagePlus imp) {
19:                 this.imp = imp;
20:                 return DOES_ALL;
21:         }
22:
23:         public void run(ImageProcessor ip) {
24:                 ImagePlus[] imps = createImageList();
25:                 String[] titles = createTitleList(imps);
26:                 getUserValues(titles);
27:
28:                 ImageProcessor ipQ = imps[Q].getProcessor();
29:                 ImageProcessor ipU = imps[U].getProcessor();
30:
31:                 double ratio =0;
32:                 double value =0;
33:                 int offset, i, x, y;
34:                 int width = ipQ.getWidth();
35:                 int height = ipQ.getHeight();
36:                 ImageProcessor newIp = new FloatProcessor(width, height);
37:                 for (y=0; y<height; y++) {
38:                         for (x=0; x<width; x++) {
39:                                 if(compute==0) {
40:                                         value = 0.5*Math.atan2
41:                                         (ipQ.getPixelValue(x,y),
42:                                         ipU.getPixelValue(x,y));
43:                                 }
44:                                 else value = Math.sqrt(Math.pow(
45:                                      ipQ.getPixelValue(x,y), 2)
46:                                      + Math.pow(ipU.getPixelValue(x,y), 2));
47:                                 newIp.putPixelValue(x,y,value);
48:                         }
49:
50:                 }
51:                 String imTitle = "";
52:                 if(compute==0) imTitle = "Polarization Angle";
53:                 else imTitle = "Polarization Intensity";
54:                 ImagePlus newImp = new ImagePlus(imTitle, newIp);
55:                 newImp.show();
56:         }
57:
58:
59:
60:         private ImagePlus[] createImageList () {
61:                 ImagePlus[] imps = new ImagePlus[WindowManager.getWindowCount()];
62:                 final int[] windowList = WindowManager.getIDList();
63:                 for (int k = 0; ((windowList != null) && (k < windowList.length));
```

```
64:                     k++) {
65:                         final ImagePlus imp =
66:                               WindowManager.getImage(windowList[k]);
67:                         imps[k] = imp;
68:                 }
69:                 return imps;
70:         }
71:
72:         private String[] createTitleList (ImagePlus[] imlist ) {
73:                 String[] titles = new String[imlist.length];
74:                 for(int i=0; i < imlist.length; i++) {
75:                         titles[i] = imlist[i].getTitle();
76:                 }
77:                 return titles;
78:         }
79:
80:
81:         /**
82:         * Create the GUI
83:         */
84:         void getUserValues(String[] titles) {
85:                 String[] s = {"Angle", "Intensity"};
86:                 GenericDialog gd = new GenericDialog
87:                                 ("Polarization Options", IJ.getInstance());
88:                 gd.addChoice("Stokes Q image", titles, titles[0]);
89:                 gd.addChoice("Stokes U image", titles, titles[1]);
90:                 gd.addChoice("Compute Polarization", s, s[0]);
91:                 gd.showDialog();
92:
93:                 if (gd.wasCanceled()) {
94:                         return;
95:                 }
96:
97:                 Q = gd.getNextChoiceIndex();
98:                 U =  gd.getNextChoiceIndex();
99:                 compute = gd.getNextChoiceIndex();
100:
101:        }
102:
103:
104: }
```

```
import ij.*;
import ij.process.*;
import ij.measure.*;
import ij.gui.*;
import java.awt.*;
import ij.plugin.*;

/**
 *  Produces a rotation measure map using the algorithm of Brown (2002)
 *  Requires a stack as input consisting of 10 images:
 *  Stokes Q images in 4 bands (i.e. A, B, C, and D)
 *  Stokes U images in 4 bands (i.e. A, B, C, and D)
 *  Stokes I image
 *  Weight image (from mosconv)
 *  Order of the images in the stack should be:
 *  QA, QB, QC, QD, UA, UB, UC, UD, I, W
 */
public class Rotation_Measure_with_r implements PlugIn {
        public void run(String arg) {

                int size;
                int width;
                int height;
                int count = 0;
                ImageProcessor PI;
                ImageProcessor QA;
                ImageProcessor QB;
                ImageProcessor QC;
                ImageProcessor QD;
                ImageProcessor UA;
                ImageProcessor UB;
                ImageProcessor UC;
                ImageProcessor UD;
                ImageProcessor I;
                ImageProcessor W;
                ImageProcessor RM;
                ImageProcessor diff;
                ImageProcessor error;
                double PA_A;
                double PA_B;
                double PA_C;
                double PA_D;
                double pa_A;
                double pa_B;
                double pa_C;
                double pa_D;
                double delta_AB;
                double delta_BC;
                double delta_CD;
                double delta_AB2;
                double delta_BC2;
                double delta_CD2;

                //for least squares fit...
                double C_QU = 0.01;//stdev of Q or U image at center of ind. field
                double alpha = 0.003;//as described by JoAnne...
                double wA, wB, wC, wD;//weighting factors for least squares fit
                double sigmaSq;
                double rm;
                double delta;
                double theta0;
                double chiSq;
                double r;
```

```
64:             double lambda_Asq = 0.045469068;
65:             double lambda_Bsq = 0.04502633;
66:             double lambda_Csq = 0.044172413;
67:             double lambda_Dsq = 0.043748434;
68:             double pi, piA, piB, piC, piD;
69:
70:             ImagePlus imp = WindowManager.getCurrentImage();
71:             if (imp == null) {
72:                     IJ.noImage();
73:                     return;
74:             }
75:             ImageStack stack = imp.getStack();
76:             size = stack.getSize();
77:             width = stack.getWidth();
78:             height = stack.getHeight();
79:
80:             //error conditions
81:             if (size == 1) {
82:                     IJ.error("Stack Required");
83:                     return;
84:             }
85:             if (size != 10) {
86:                     IJ.error("10 images are required to be in stack\n
87:                     (QA, QB, QC, QD, UA, UB, UC, UD, I, and Weights)");
88:                     return;
89:             }
90:
91:             //create reference to each image in the stack
92:
93:             QA = stack.getProcessor(1);
94:             QB = stack.getProcessor(2);
95:             QC = stack.getProcessor(3);
96:             QD = stack.getProcessor(4);
97:             UA = stack.getProcessor(5);
98:             UB = stack.getProcessor(6);
99:             UC = stack.getProcessor(7);
100:            UD = stack.getProcessor(8);
101:            I = stack.getProcessor(9);
102:            W = stack.getProcessor(10);
103:
104:            //create reference for the rotation measure image
105:            RM = new FloatProcessor(width, height);
106:            diff = new FloatProcessor(width, height);
107:            error = new FloatProcessor(width, height);
108:
109:            for (int i = 0; i < width; i++) {
110:                    for (int j = 0; j < height; j++) {
111:                            //check if PI value is above the threshold
112:                            //(use a thresholded PI image)
113:
114:                            //find unwrapped angles...
115:                            PA_A = Math.atan2(UA.getPixelValue(i, j),
116:                                    QA.getPixelValue(i, j)) + Math.PI;
117:                            PA_B = Math.atan2(UB.getPixelValue(i, j),
118:                                    QB.getPixelValue(i, j)) + Math.PI;
119:                            PA_C = Math.atan2(UC.getPixelValue(i, j),
120:                                    QC.getPixelValue(i, j)) + Math.PI;
121:                            PA_D = Math.atan2(UD.getPixelValue(i, j),
122:                                    QD.getPixelValue(i, j)) + Math.PI;
123:
124:                            //find wrapping factors...
125:                            delta_AB2 = Math.atan2(Math.sin(PA_B-PA_A),
126:                                            Math.cos(PA_B-PA_A));
```

```
127:                    delta_BC2 = Math.atan2(Math.sin(PA_C-PA_B),
128:                                Math.cos(PA_C-PA_B));
129:                    delta_CD2 = Math.atan2(Math.sin(PA_D-PA_C),
130:                                Math.cos(PA_D-PA_C));
131:
132:
133:
134:                    //find wrapped angles...
135:                    PA_A = PA_A;
136:                    PA_B = (PA_A + delta_AB2);
137:                    PA_C = (PA_B + delta_BC2);
138:                    PA_D = (PA_C + delta_CD2);
139:                    PA_A = PA_A / 2;
140:                    PA_B = PA_B / 2;
141:                    PA_C = PA_C / 2;
142:                    PA_D = PA_D / 2;
143:
144:                    //weighted least squares fit...
145:
146:                    //first find weighting factor
147:
148:                    piA = Math.sqrt(Math.pow(UA.getPixelValue(i,j),2)
149:                          +Math.pow(QA.getPixelValue(i,j),2));
150:                    piB = Math.sqrt(Math.pow(UB.getPixelValue(i,j),2)
151:                          +Math.pow(QB.getPixelValue(i,j),2));
152:                    piC = Math.sqrt(Math.pow(UC.getPixelValue(i,j),2)
153:                          +Math.pow(QC.getPixelValue(i,j),2));
154:                    piD = Math.sqrt(Math.pow(UD.getPixelValue(i,j),2)
155:                          +Math.pow(QD.getPixelValue(i,j),2));
156:                    sigmaSq = Math.pow( C_QU *
157:                              Math.sqrt(1/W.getPixelValue(i,j)) , 2)
158:                              + Math.pow(
159:                                alpha * I.getPixelValue(i,j) ,2);
160:                    wA = (4*piA*piA) / sigmaSq;
161:                    wB = (4*piB*piB) / sigmaSq;
162:                    wC = (4*piC*piC) / sigmaSq;
163:                    wD = (4*piD*piD) / sigmaSq;
164:
165:                    //w = 1;
166:                    // do the fit
167:                    delta = (
168:                                    (wA+wB+wC+wD) *
169:                                    (wA * lambda_Asq * lambda_Asq
170:                                    + wB * lambda_Bsq * lambda_Bsq
171:                                    + wC * lambda_Csq * lambda_Csq
172:                                    + wD * lambda_Dsq * lambda_Dsq)
173:                            )       - Math.pow((wA * lambda_Asq
174:                                    + wB * lambda_Bsq + wC * lambda_Csq
175:                                    + wD * lambda_Dsq), 2);
176:
177:                            rm = (  ((wA+wB+wC+wD) *
178:                                    (wA * lambda_Asq * PA_A
179:                                        + wB * lambda_Bsq * PA_B
180:                                        + wC * lambda_Csq * PA_C + wD *
181:                                          lambda_Dsq * PA_D)
182:                                        ) -
183:                                    (wA * lambda_Asq + wB * lambda_Bsq
184:                                    + wC * lambda_Csq
185:                                    + wD * lambda_Dsq) *
186:                                    (wA * PA_A + wB * PA_B
187:                                    + wC * PA_C + wD * PA_D)
188:                                     )/ delta;
189:
```

```
190:                                theta0 = (
191:                                          ((wA * lambda_Asq * lambda_Asq
192:                                          + wB * lambda_Bsq * lambda_Bsq
193:                                          + wC * lambda_Csq * lambda_Csq
194:                                          + wD * lambda_Dsq * lambda_Dsq)
195:                                           * (wA * PA_A + wB * PA_B
196:                                             + wC * PA_C + wD * PA_D)) -
197:                                          ((wA * lambda_Asq
198:                                          + wB * lambda_Bsq
199:                                          + wC * lambda_Csq
200:                                          + wD * lambda_Dsq)
201:                                           * (wA * lambda_Asq * PA_A
202:                                           + wB * lambda_Bsq * PA_B
203:                                           + wC * lambda_Csq * PA_C
204:                                           + wD * lambda_Dsq * PA_D))
205:                                         ) / delta;
206:
207:                                /*chiSq = Math.pow(Math.sqrt(wA) *
208:                                          (PA_A - theta0 - lambda_Asq * rm),
209:                                          2) + Math.pow(Math.sqrt(wB) *
210:                                          (PA_B - theta0 - lambda_Bsq * rm), 2) +
211:                                          Math.pow(Math.sqrt(wC) *
212:                                          (PA_C - theta0 - lambda_Csq * rm), 2) +
213:                                          Math.pow(Math.sqrt(wD) *
214:                                          (PA_D - theta0 - lambda_Dsq * rm), 2);
215:                                */
216:                                r = (
217:                                        (4* (lambda_Asq * PA_A + lambda_Bsq * PA_B
218:                                        + lambda_Csq * PA_C + lambda_Dsq * PA_D)) -
219:                                        ((lambda_Asq + lambda_Bsq + lambda_Csq
220:                                        + lambda_Dsq) * (PA_A + PA_B
221:                                        + PA_C + PA_D))
222:                                ) /
223:                                (
224:                                        Math.sqrt(
225:                                                (4*(lambda_Asq*lambda_Asq
226:                                                + lambda_Bsq*lambda_Bsq
227:                                                + lambda_Csq*lambda_Csq
228:                                                + lambda_Dsq*lambda_Dsq)) -
229:                                                Math.pow((lambda_Asq + lambda_Bsq
230:                                                + lambda_Csq + lambda_Dsq),2)
231:                                        ) *
232:                                        Math.sqrt(
233:                                                (4*(PA_A*PA_A + PA_B*PA_B
234:                                                + PA_C*PA_C + PA_D*PA_D)) -
235:                                                Math.pow((PA_A + PA_B
236:                                                + PA_C + PA_D),2)
237:                                        )
238:                                );
239:
240:                                //store the fit value in the array
241:                                if(Math.abs(rm) < 10000000)
242:                                RM.putPixelValue(i, j, rm);
243:                                else RM.putPixelValue(i, j, 0);
244:                                //find error
245:                                if(Math.abs(r) < 1)
246:                                error.putPixelValue(i, j, Math.abs(r));
247:                                else error.putPixelValue(i,j,0);
248:                                //}
249:
250:                                //else {}
251:                        }
252:                }
```

```
253:                //show the RM map
254:                ImagePlus rmImp = new ImagePlus("Rotation Measure Map", RM);
255:                rmImp.show();
256:                //show the error (linear correlation coefficient) map
257:                ImagePlus erImp = new ImagePlus("Error Map", error);
258:                erImp.show();
259:        }
260:
261: }
262:
```

```
 1: import ij.*;
 2: import ij.process.*;
 3: import ij.gui.*;
 4: import java.awt.*;
 5: import ij.plugin.*;
 6:
 7: /**
 8: * Averages square regions (of dimension scale x scale) and
 9: * produces a new image consisting of the averaged values
10: */
11:
12: public class Make_Averaged_Map implements PlugIn {
13:
14:         public void run(String arg) {
15:
16:                 int imSize = 2048;
17:                 int scale =  16;
18:                 double min;
19:                 ImagePlus imp = WindowManager.getCurrentImage();
20:                 ImageProcessor bg = new FloatProcessor(2048/scale, 2048/scale);
21:                 ImageStatistics is = new ImageStatistics();
22:
23:                 for(int i=0; i<imSize/scale; i++) {
24:                         for(int j=0; j<imSize/scale; j++) {
25:                                 imp.setRoi(i*scale, j*scale, scale, scale);
26:                                 min=is.getStatistics(imp.getProcessor(), 1,
27:                                 null).mean;
28:                                 bg.putPixelValue(i,j,min);
29:                         }
30:                 }
31:
32:                 ImagePlus bgImp = new ImagePlus("Background Map", bg);
33:                 bgImp.show();
34:         }
35:
36: }
```

```
 1: import ij.*;
 2: import ij.process.*;
 3: import ij.gui.*;
 4: import java.awt.*;
 5: import ij.plugin.*;
 6: import java.io.*;
 7:
 8: /**
 9: * Writes a Karma annotation file:
10: * scales the pixel values appropriately - using image centre of
11: * 134.5, 4.5 and image size of 2048x2048
12: * scales the RM by a factor of 4000 (chosen so the symbols
13: * would have a reasonable size)
14: * uses Karma annotation file syntax and writes to the results window
15: * after program exectues, contents of the results window
16: * may be saved as an annotation file
17: */
18: public class Make_RM_annotations implements PlugIn {
19:
20:
21:         int imSize = 128;
22:
23:         public void run(String arg) {
24:
25:                 double value;
26:                 ImagePlus imp = WindowManager.getCurrentImage();
27:                 ImageProcessor rm = imp.getProcessor();
28:                 ImageStatistics is = new ImageStatistics();
29:
30:                 for(int i=0; i<imSize; i++) {
31:                         for(int j=0; j<imSize; j++) {
32:
33:                                 value = rm.getPixelValue(i,j);
34:                                 if (value>-1000&value<1000 && value!=0)
35:                                 writeAnnFile(value, (double)i, (double)j);
36:                         }
37:                 }
38:
39:         }
40:
41:
42:         void writeAnnFile(double value, double i, double j) {
43:                 double l = 0;
44:                 double b = 0;
45:
46:                 double l_ref = imSize/2;
47:                 double b_ref = imSize/2;
48:                 double degPerPix = (double)(2048/imSize)*20/60/60;
49:                 if (i<l_ref) l = 134.5 + (l_ref-i)*degPerPix;
50:                 else l = 134.5 - (i-l_ref)*degPerPix;
51:
52:                 if (j<b_ref) b = 4.5 - (b_ref-j)*degPerPix;
53:                 else b = 4.5 + (j-b_ref)*degPerPix;
54:                 String str= "";
55:                 if(value>0)  str = "color yellow\n"+str+"CIRCLE W "
56:                                 +IJ.d2s(l,6) +" " +IJ.d2s(b,6) +" " +value/4000
57:                                 + "                 # "+value;
58:                 else str = "color blue\n" + str + "CBOX W "
59:                      +IJ.d2s(l,6) +" " +IJ.d2s(b,6) +" "
60:                      +value/4000 +" " +value/4000+ "           # "+value;
61:                 IJ.write(str);
62:         }
63:
```

```
64:         /**
65:         * Converts a String to a char[]
66:         */
67:         char[] s2ch (String str, int offset) {
68:
69:                 int j = 0;
70:                 char[] ch = new char[str.length()];
71:                 for (int i = offset; i < str.length()+offset; i++) {
72:                         ch[i] = str.charAt(j++);
73:                         // if path uses "\", replace with "/"
74:                         if (ch[i] == (char)0x5C) ch[i] = (char)0x2F;
75:                 }
76:                 return ch;
77:         }
78:
79: }
```